

Simulation of the Optics of the Imaging Air-Cherenkov Telescopes IceAct with Geant4

Master Thesis in Physics

by
Maurice Günder, B.Sc.

revised version

submitted to
III. PHYSIKALISCHES INSTITUT B
RHEINISCH-WESTFÄLISCHE TECHNISCHE HOCHSCHULE AACHEN
Univ.-Prof. Dr. Christopher Wiebusch

in
April 2019

First Referee

Univ.-Prof. Dr. Christopher Wiebusch
Physics Institute III B
RWTH Aachen University

Second Referee

Prof. Dr. Thomas Bretz
Physics Institute III A
RWTH Aachen University

Supervisor

Dr. Jan Auffenberg
Physics Institute III B
RWTH Aachen University

Contents

1. Introduction	1
1.1. Motivation	1
1.2. The IceCube Neutrino Observatory	2
1.2.1. IceCube-Gen2	4
1.3. Cosmic Rays	4
1.4. Extensive Air Showers	6
1.5. Detection of Cosmic-ray Air Showers via Atmospheric Cherenkov Light .	8
1.5.1. The Cherenkov Effect	8
1.5.2. Detection Techniques	11
1.6. Imaging Air-Cherenkov Telescopes (IACTs)	12
1.7. The IceCube Air-Cherenkov Telescopes IceAct	14
2. The IceAct Model in GEANT4	17
2.1. GEANT4	17
2.1.1. FAMOUS Telescope Simulation	18
2.2. Materials	19
2.3. Optics	22
2.3.1. Glass Plate	23
2.3.2. Fresnel Lens	24
2.3.3. Camera	27
2.3.3.1. Winston Cones – Working Principle	28
2.3.3.2. Winston Cone Implementation in GEANT4	30
2.3.3.3. Silicon Photomultipliers (SiPM)	31
2.3.3.4. SiPM Implementation in GEANT4	36
3. IceAct Simulation	39
3.1. Getting to Know the IceAct Optics	39
3.1.1. “Best” Wavelength	39

3.1.2. Focal Plane Shift	41
3.1.3. Winston Cone Meshing	44
3.1.4. The “Ghost Image” Effect	47
3.1.5. Impact-location-dependent Detection Efficiency	49
3.2. Parameterization Simulation	53
4. IceAct Parameterization Strategy	55
4.1. Kernel Density Estimation (KDE)	56
4.1.1. Adaptive KDE with Gaussian Kernel	57
4.1.2. Bootstrapping	58
4.2. Coordinate Transformation for KDE	59
4.3. KDE Evaluation	60
4.3.1. The HEALPix Algorithm	60
4.3.2. KDE Renormalization: Detection Efficiency	63
5. Application on Simulated Data	67
5.1. Wavelength Binning	67
5.2. Adaptive vs. Non-adaptive KDE	68
5.3. Detection Efficiency Maps	72
5.3.1. Choice of HEALPix Pixelization Parameter N_{side}	72
5.3.2. Overview of Results	74
5.4. Lookup Table (LUT)	79
5.4.1. LUT Production	79
5.4.2. LUT Readout – “Event Dicing”	81
5.5. Application on CORSIKA Air Shower Events	83
6. Summary and Outlook	85
A. Access to the IceAct GEANT4 Simulation	87
B. Additional Plots	89
B.1. Impact-location-dependent Detection Efficiency	89
B.2. Detection Efficiency Maps	92
B.3. Camera Pixel Response For Single HEALPixels	96
Figures	I
Tables	III

Literature	V
Acknowledgements	
Danksagungen	XI

CHAPTER 1.

Introduction

»Remember to look up at the stars and not down at your feet. Try to make sense of what you see and wonder about what makes the universe exist.«

Stephen Hawking

1.1. Motivation

The exploration of cosmic rays and cosmic-ray air showers is one of the major challenges in astro-particle physics. Scientists all over the world try to explain the mechanisms in extra-galactic sources that enable them to accelerate particles to incredibly high energies of 10^{20} eV. These particles reach us in the form of so called *cosmic rays* which can be explored to understand their spectrum in a preferably wide energy range. Especially for the highest energies, the flux is very low. In order to compensate for this, larger and larger detectors are built. The *IceCube Neutrino Observatory* is one of them. It is a neutrino telescope at the geographic South Pole measuring the Cherenkov light of secondary charged particles originating from neutrino interactions with the Antarctic ice. To differentiate between interesting – so called *cosmogenic* – neutrinos and less interesting atmospheric neutrinos, the surface detector IceTop is installed above IceCube to veto muons and neutrinos from air showers.

A large-scale upgrade – *IceCube-Gen2* – is planned to massively enlarge the instrumented volume. A part of this upgrade is an extension of the surface detector by adding detectors with complementary detection techniques. One approach is to install an array of compact imaging air-Cherenkov telescopes – called *IceAct* – based on a 61-pixel SiPM camera. In December 2015, a 7-pixel demonstrator telescope was deployed and successfully showed its veto and calibration capabilities together with IceTop during its measuring period in 2016. Additionally, *IceAct* can be used for cosmic ray composition measurements. Thanks to the air shower simulation toolkit CORSIKA, one can produce Monte Carlo data for air showers with various properties like primary energy, primary particle, inclination, etc. In order to evaluate Monte Carlo data – i.e. how the showers are “seen” by *IceAct* – a detailed knowledge of the optical system is crucial.

In this thesis, the full optical system of a single *IceAct* telescope is simulated with GEANT4 with the goal to parameterize the response of each camera pixel depending on direction and wavelength of incident Cherenkov photons by a preferably efficient lookup table.

1.2. The IceCube Neutrino Observatory

Since January 2011, the IceCube Neutrino Observatory at the Amundsen-Scott South Pole station is measuring neutrinos emanating from various sources. For this purpose, a detector instrumented with digital optical modules (*DOMs*) is installed deep in the antarctic ice. 5160 of these optical sensors are arranged on 86 strings at a height between 1450 m and 2450 m below the surface. The central region of this in-ice array which has a higher density of *DOMs* is called *DeepCore*. Figure 1.1 shows a sketch of the detector arrangement.

Neutrinos are very interesting elementary particles because of their weak interaction cross-section and their electrical neutrality. This fact makes it possible for neutrinos to point back to their sources which is exploited in the search for astrophysical processes like active galactic nuclei, supernovae, or gamma-ray bursts. Since they are able to reach us without scattering processes, neutrinos can even give information about sources at cosmological distances. Simultaneously, the weak interaction potential is what makes neutrino detection challenging. Therefore, a detector with a large scale active volume is needed. In the case of IceCube, this is about 1 km^3 of ice. Finally, neutrinos are detected by the Cherenkov light (cf. section 1.5) of secondary charged particles that are produced

in unlikely but still occurring interactions with the glacial ice.

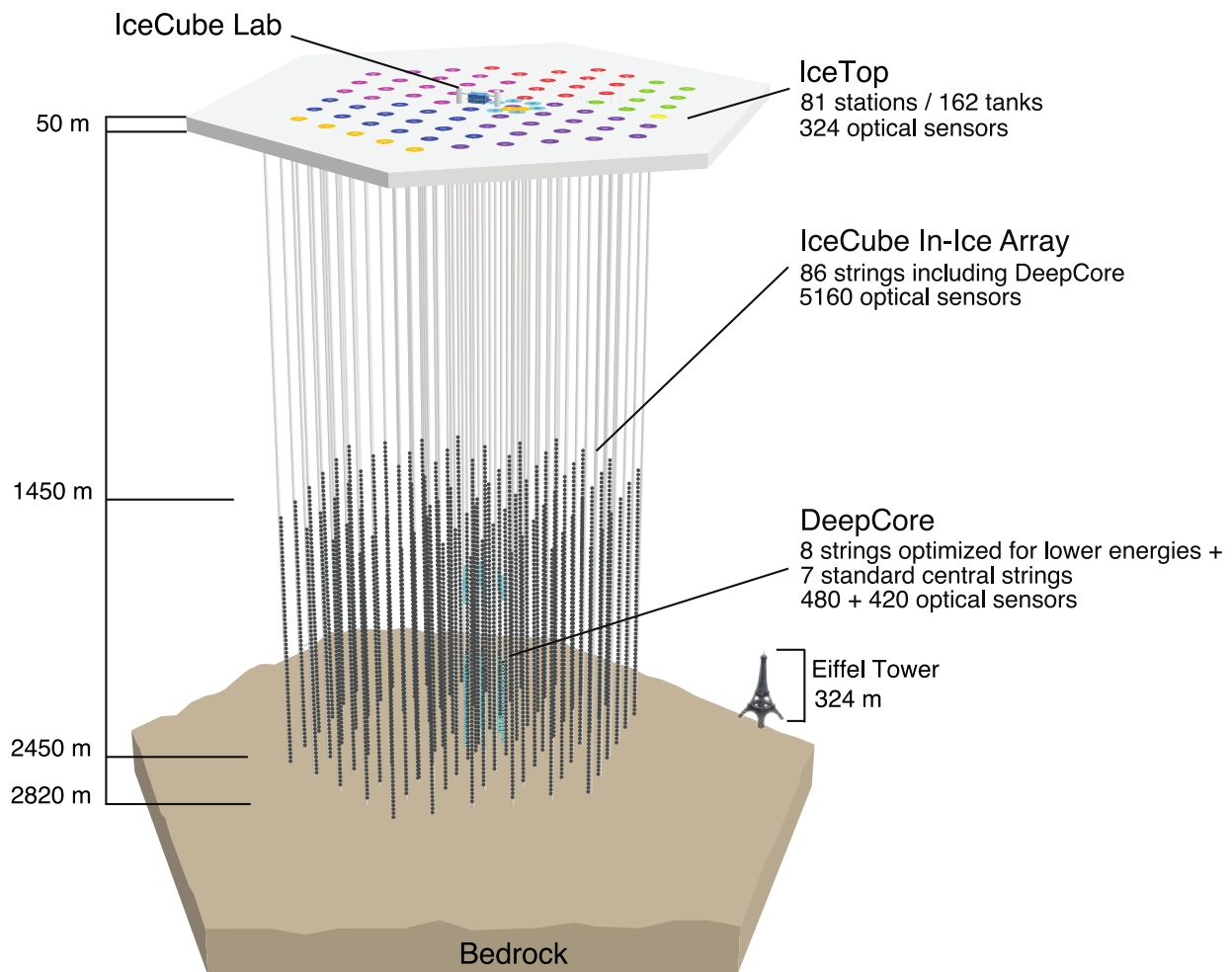


Figure 1.1.: Schematic view of the IceCube Neutrino Observatory. [1] The in-ice array with the denser sub-array DeepCore as well as the surface array IceTop is sketched. Different station colors represent different deployment stages.

At the surface on top of the in-ice detector, the cosmic-ray air shower array IceTop is installed to detect Cherenkov radiation (cf. 1.5). IceTop consists of 81 stations approximately arranged in the same grid as the in-ice strings. Each station has two tanks filled up with ice and two IceCube DOMs. This arrangement makes it possible for IceTop to detect primary cosmic rays (cf. 1.3) in the energy range of PeV to EeV. One purpose of IceTop is to provide a veto for downward-going neutrinos in the IceCube detector emanating from coincident atmospheric air shower events. [1] Since IceCube is mainly investigating astrophysical neutrinos, atmospheric neutrinos are a major background.

Since the start of operation, IceCube has achieved two important breakthroughs. In 2013, high-energetic extraterrestrial neutrinos were observed [2]. Four years later – on 22 September 2017 – IceCube has detected a high-energy neutrino originating from the blazar TXS+0506-056 which was coincident in time and direction with a gamma-ray flare of this source. As a result, this was the first time that an extra-galactic accelerator could be identified as a source of an astrophysical neutrino [3].

1.2.1. IceCube-Gen2

IceCube-Gen2 is proposed to be a substantial enhancement of the IceCube Neutrino Observatory. It is planned to have a much better sensitivity to high-energy neutrinos by an instrumented volume about ten times bigger than IceCube has today. Studies of extra-galactic neutrino sources and resolving their locations require a much higher rate of detected neutrinos than IceCube provides by now. For this purpose, more strings with a denser spacing of further improved DOMs will be deployed covering a much larger in-ice volume. [4, 5] Additionally, a large upgrade of IceTop concerning veto capabilities (*IceVeto*) is discussed with different approaches. These are scintillation detectors (*IceScint*) [6], a radio antenna array [7], or imaging air-Cherenkov telescopes (*IceAct*) [4, 8].

1.3. Cosmic Rays

Charged particles or nuclei that are propagating through the universe and incidentally reaching the Earth's atmosphere are called *cosmic rays*. They were discovered by the Austrian physicist VICTOR FRANZ HESS in 1912 when he observed an increasing discharge of electroscopes with increasing height in seven balloon flights. [9] Hess initially called this underlying radiation “durchdringende Strahlung” (*penetrating radiation*).

When it comes to cosmic rays, ascertaining the mass composition is a key measurement for learning about their propagation in universe and about extra-galactic cosmic ray accelerators. Figure 1.2 shows that the energy spectrum of cosmic rays follows a power law:

$$\frac{dN}{dE} \propto E^{-\gamma}, \quad (1.1)$$

introducing a spectral index γ which is dependent from the considered energy region.

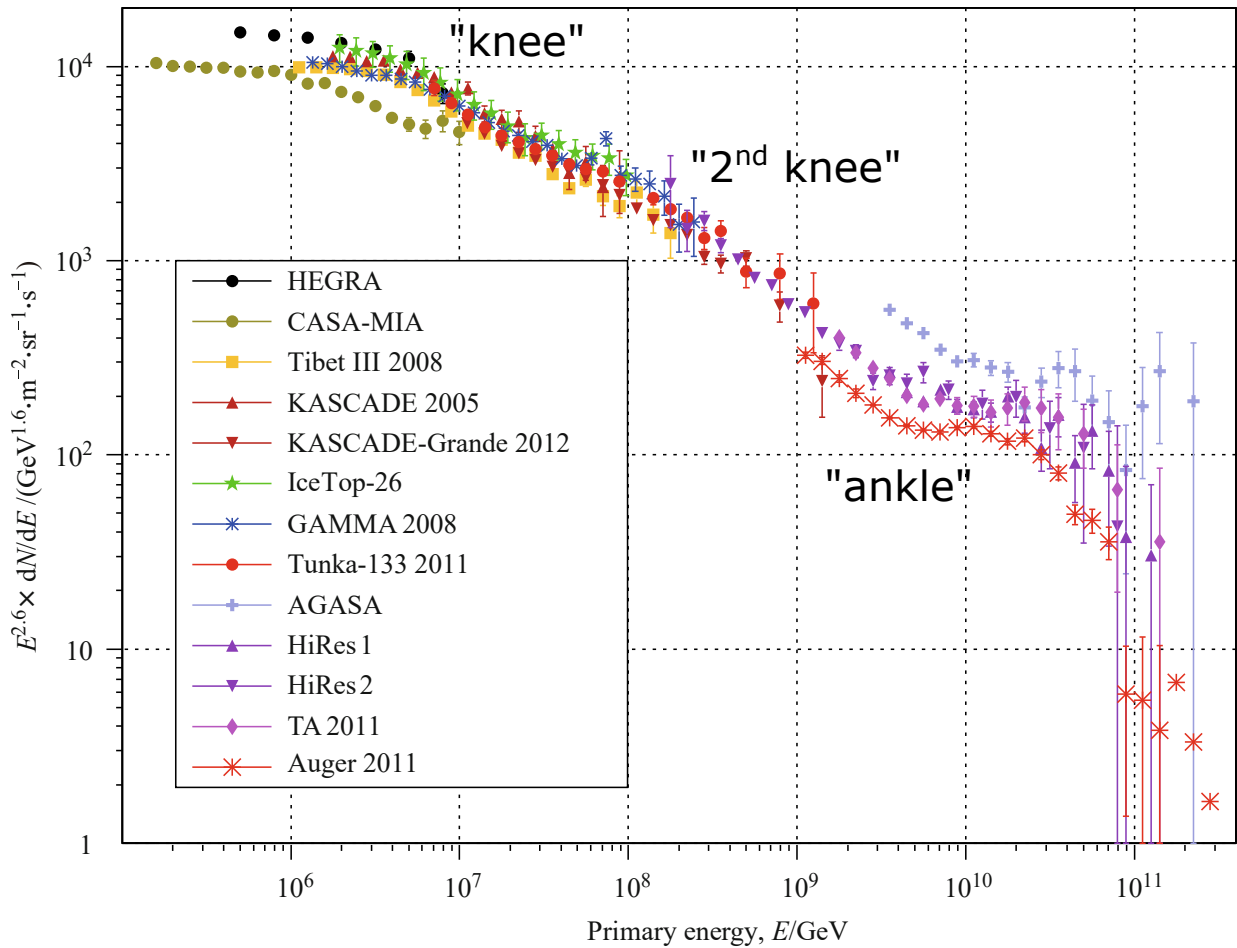


Figure 1.2.: Energy spectrum of cosmic rays measured with multiple air shower experiments. [10, adapted] The three prominent regions known as “knee”, “second knee”, and “ankle” are marked. Multiplication of the spectrum by the factor $E^{2.6}$ leads to a better visibility and shows that the spectral index changes at these features.

Measurements show [11, 12]

$$\gamma(E) = \begin{cases} 2.7 & \sim 10 \text{ GeV} < E < 4 \cdot 10^6 \text{ GeV} \\ 3.1 & 4 \cdot 10^6 \text{ GeV} < E < 4 \cdot 10^9 \text{ GeV} \\ 2.6 & 4 \cdot 10^9 \text{ GeV} < E < 3 \cdot 10^{11} \text{ GeV} \end{cases} . \quad (1.2)$$

Due to these interesting features, composition measurements at the transition points are desired in particular.

The phenomenological model to describe the spectrum is referred to as *poly gonato* (Greek for “many knees”). The “knee” is assumed to be based on different rigidity¹ dependent cut-off energies for sub-spectra of element groups which sum up to the observed spectrum. [11, 13] At energies beyond 10^{11} GeV, a strong suppression is observed. The GZK-effect (named after KENNETH GREISEN, GEORGIY ZATSEPIN, and VADIM KUZMIN) is supposed to be the reason. Protons with energies above a threshold of $5 \cdot 10^{19}$ eV can interact with photons of the cosmic microwave background in such a way that they produce π^0 and π^+ mesons via Δ^+ resonance:



Thus, the protons effectively lose about 20 % of their energy. Additionally, calculations show that these interactions become quite frequent for proton energies of $E_p \gtrsim 10^{20}$ eV which results in an effective cut-off of cosmic-ray energies above this region. [14]

1.4. Extensive Air Showers

If a high energetic particle – a photon or hadron – incidentally reaches the Earth’s atmosphere, it interacts with their atoms. A common way to describe the traversed atmospheric matter for an air shower is the *slant depth*

$$X(h) = \int_h^\infty \rho(h') dh', \quad (1.4)$$

with the height-dependent air density $\rho(h)$. Once a high-energetic “primary” particle interacts with an atmospheric atom, it initiates a cascade of secondary particles. Typically, one differentiates between hadronic and electromagnetic cascades or showers (cf. figure 1.3). For electromagnetic showers or sub-showers, *Heitler’s model* is used as a simple conception. The model is based on two-body splittings of electrons, positrons, and photons by e^+e^- pair production or bremsstrahlung which occur after a fixed distance $d = \lambda_{\text{em}} \ln 2$ by using the medium-specific *radiation length* λ_{em} . In other words: after n splitting processes, the shower consists of $N = 2^n = e^{x/\lambda_{\text{em}}}$ electrons and photons.

¹ property of a magnetic field to bend a particle’s trajectory

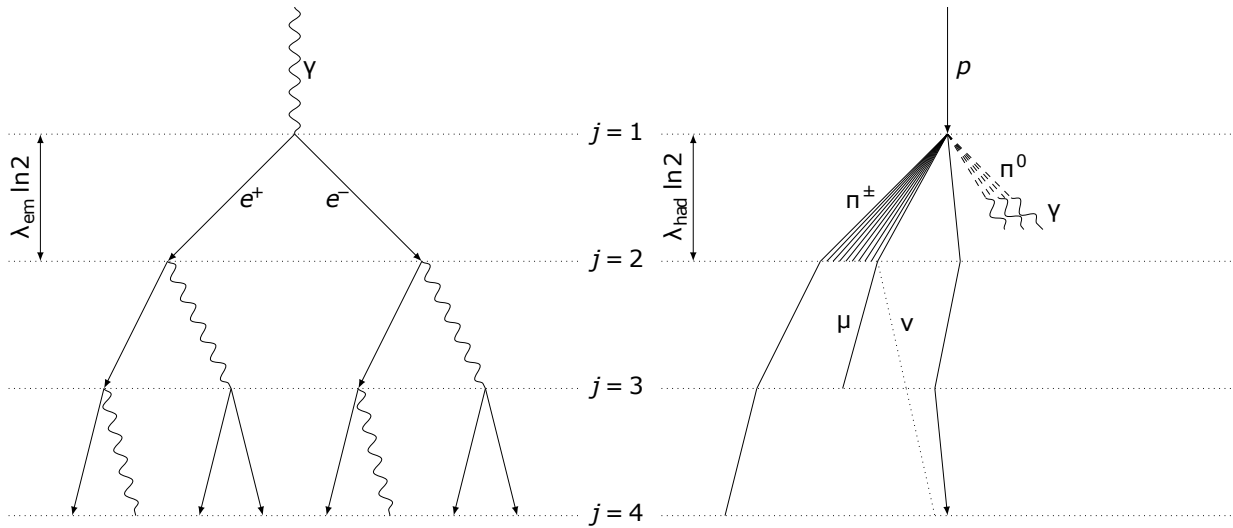


Figure 1.3.: Schematic view of extensive air showers. [15] Two possible shower formations are shown. A primary photon initiates an electromagnetic shower (left) whereas a primary proton initiates a hadronic shower with electromagnetic sub-showers. The splitting steps are stated as well as the interaction lengths. For the hadronic cascades not all traces are sketched for clarity reasons.

The multiplication process holds, until the particle energies are high enough for pair production and bremsstrahlung. Below this energy which Heitler named the *critical energy* ξ_c^e , the shower size decreases. Hence, the maximum number of particles $N_{\max} = 2^{n_c}$ is reached after n_c splitting steps. The energy of a considered primary photon E_\circ is then distributed among all secondary shower particles so that $E_\circ = \xi_c^e N_{\max} = \xi_c^e 2^{n_c}$. With this information, one can derive the slant depth X_{\max} at which the shower has the largest size. It is

$$X_{\max}^\gamma = n_c \lambda_{\text{em}} \ln 2 = \lambda_{\text{em}} \ln \frac{E_\circ}{\xi_c^e}. \quad (1.5)$$

It should be mentioned that this calculation only holds for pure electromagnetic showers which is the reason for the superscript γ in equation (1.5). [16] Since the maximum depth X_{\max} is dependent from energy and type of the primary particle, it is a very important parameter for composition studies of cosmic rays. A detailed discussion on several interaction models and comparisons to simulation is done in [16].

1.5. Detection of Cosmic-ray Air Showers via Atmospheric Cherenkov Light

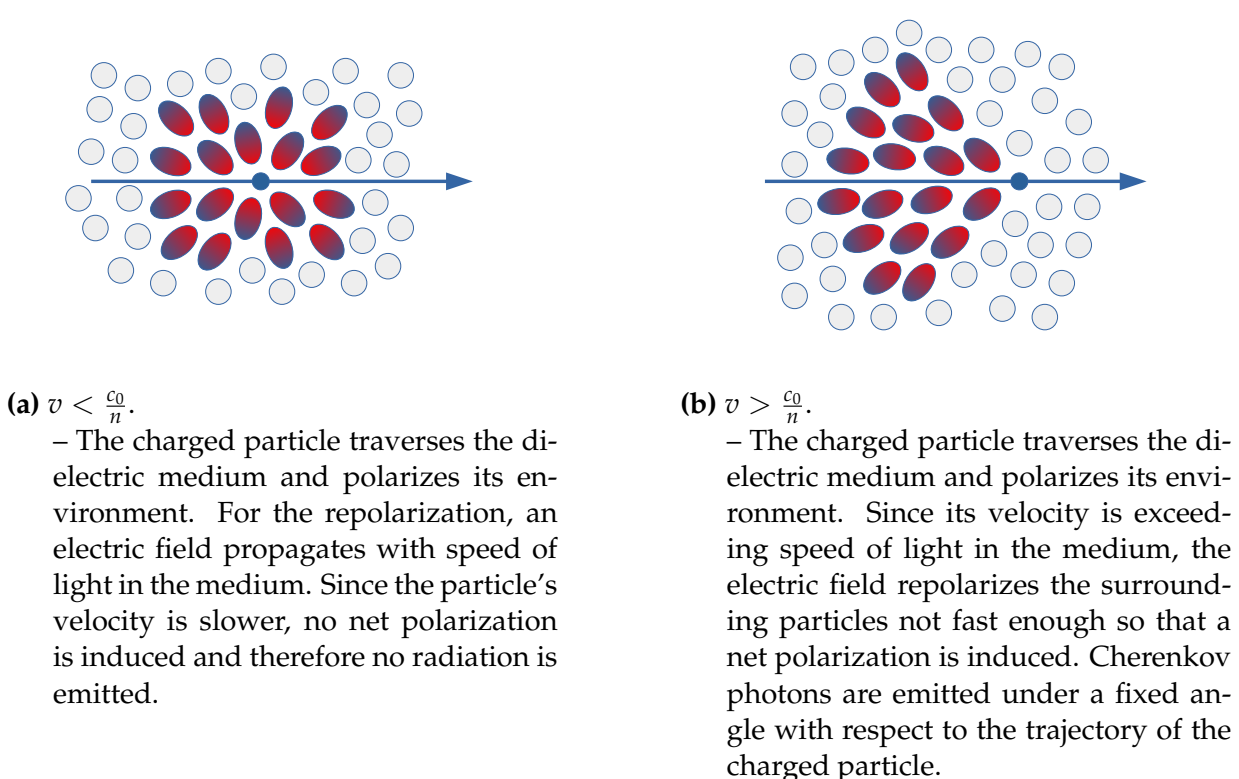
This section should give a brief introduction to the different detection possibilities of cosmic-ray air showers. In particular, the focus is on the detection via atmospheric Cherenkov light and the physics of the Cherenkov effect.

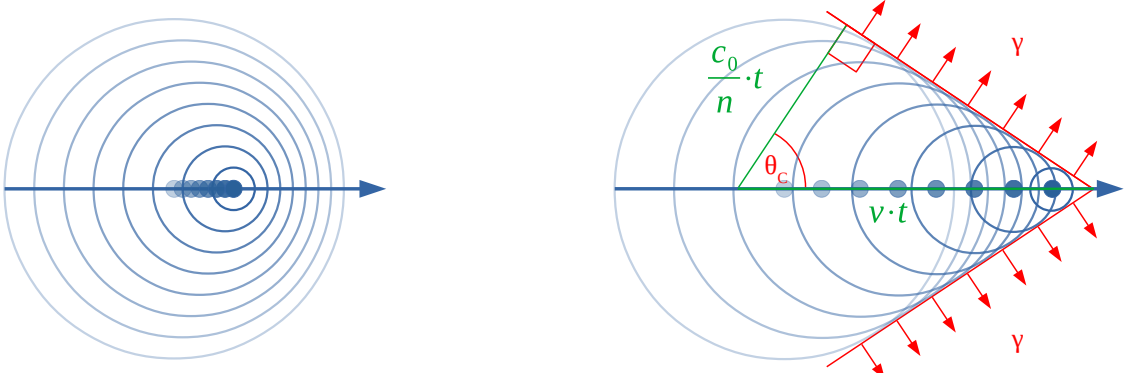
1.5.1. The Cherenkov Effect

The *Cherenkov effect* is named after the Soviet physicist PAVEL A. CHERENKOV and describes the emission of radiation if a charged particle traverses a medium with a speed that exceeds speed of light in the medium. [17] This is possible due to the fact that speed of light in a medium with a refractive index $n > 1$ is always below vacuum speed of light c_0 since

$$c = \frac{c_0}{n} \stackrel{n \geq 1}{\Rightarrow} c < c_0. \quad (1.6)$$

The effect is describable in two ways which are shown in figure 1.4.





(c) $v < \frac{c_0}{n}$.

- The charged particle induces electromagnetic elementary waves along its trajectory which propagate faster through the medium than the particle. No radiation is emitted.

(d) $v > \frac{c_0}{n}$.

- The charged particle induces electromagnetic elementary waves along its trajectory which propagate slower through the medium than the particle. All elementary waves add up to a wavefront under a fixed angle θ_C . With this model the Cherenkov effect can be interpreted as the optical analogue for the *sonic boom*.

Figure 1.4.: Illustration for the Cherenkov effect. A charged particle is traversing the medium with a refractive index n from left to right with velocity v . c_0 is the vacuum speed of light. In (a) and (b), the dipole interpretation of the Cherenkov effect is shown. (c) and (d) show the effect by exploiting Huygens' principle of elementary waves.

A *Cherenkov angle* θ_C – as introduced in figure 1.4d – can be calculated by applying trigonometry:

$$\cos \theta_C = \frac{c_0}{nv} = \frac{1}{n\beta}, \quad (1.7)$$

with the dimensionless velocity $\beta = \frac{v}{c_0}$.

Furthermore, the two Soviet physicists ILYA M. FRANK and IGOR Y. TAMM found a relation for the differential emission per wavelength and spatial interval known as the *Frank-Tamm formula* [18]:

$$\frac{d^2N}{dxd\lambda} = 2\pi\alpha q^2 \frac{1}{\lambda^2} \left(1 - \frac{1}{n^2(\lambda)\beta^2}\right), \quad (1.8)$$

with

$\frac{d^2N}{dx d\lambda}$	number of emitted Cherenkov photons per unit wavelength and unit propagation length,
α	fine structure constant,
q	particle charge,
λ	wavelength,
$n(\lambda)$	refractive index of the medium (wavelength dependent),
$\beta = \frac{v}{c_0}$	dimensionless relative velocity.

The factor $\frac{1}{\lambda^2}$ suppresses higher wavelengths so that the Cherenkov spectrum is dominant in the ultra-violet regime. Figure 1.5 shows a measured energy spectrum.

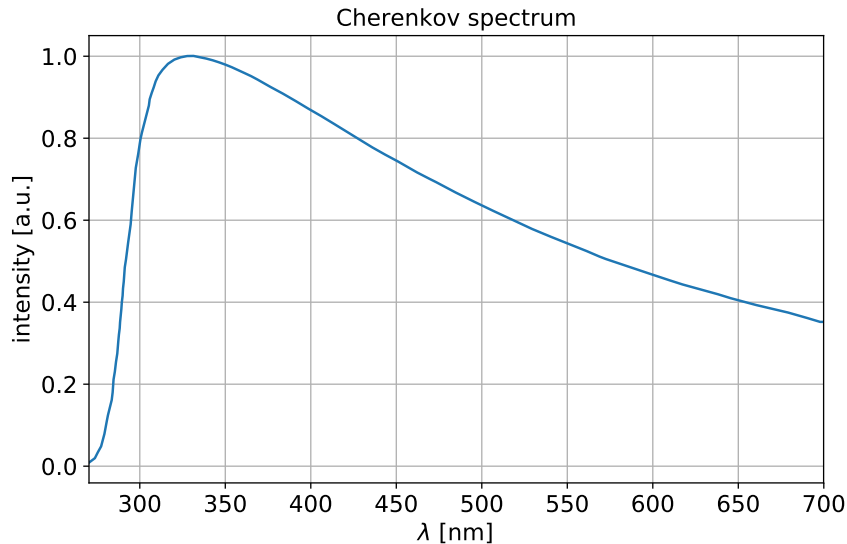


Figure 1.5.: Cherenkov wavelength spectrum. Exemplary spectrum of Cherenkov photons measured at 2200 m above sea level at the HEGRA IACT System (La Palma)². The falling edge towards high wavelength is proportional to λ^{-2} whereas the falling edge towards low wavelengths is caused by atmospheric attenuation. Data adapted from [19].

The cone-like radiation profile of Cherenkov light with respect to the air shower axis makes it possible to reconstruct the shower direction by observing the direction of the Cherenkov photons.

² High Energy Gamma Ray Astronomy, operated between 1987 and 2006 at Roque de los Muchachos Observatory on La Palma. [19]

1.5.2. Detection Techniques

Various detection techniques have been developed in the last decades. Overall, they can be divided into two categories:

- direct detection of air shower particles on ground or underground and
- detection of electromagnetic radiation originating directly or indirectly from the electromagnetic air shower component (and the muonic component in a minor part).

Commonly used particle detection experiments are based on scintillation or water-Cherenkov light. For the second category, there are some different effects to look at, in particular fluorescence light, radio, and air-Cherenkov light (cf. section 1.5.1) emission. Figure 1.6 gives a schematic overview of the operating techniques. [20]

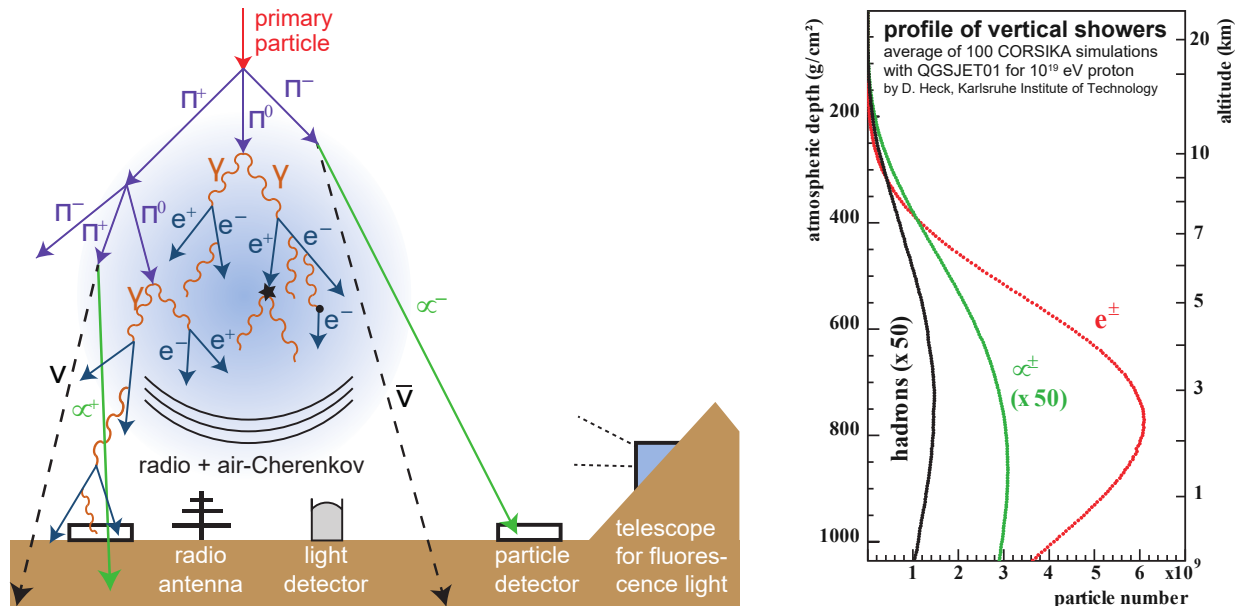


Figure 1.6.: Different techniques for the detection of atmospheric air showers. [20]

Most of the detection techniques (radio antennas, air-Cherenkov, and fluorescence light detectors) use the electromagnetic (e.m.) shower component. Muons typically reach further than the e.m. component and can be measured by particle detectors. There are more different particles than depicted contributing to real air showers. In addition, the right plot shows the longitudinal shower profile for hadrons, electrons or positrons, and muons or anti-muons.

Important parameters to be detected are direction and energy of air showers. Directional information can be reconstructed by measuring arrival times or an imaging system. The energy can be determined by the integrated signal strength, i.e. the amount

of detected particles in the case of (under-)ground particle detectors or, respectively, the amount of electromagnetic radiation. Composition-dependent air shower variables like X_{\max} are more difficult to detect.

A major challenge all detection varieties have in common is the low flux of primary cosmic rays. One tries to compensate for this by maximizing the instrumented or observed volume. Fluorescence light detectors typically have a large observable atmospheric volume and a sensitivity for air showers up to a few 10 km. For other techniques, large surface arrays instrumenting areas up to several 1000 km^2 have to be build. [20]

In this thesis, the focus is on the air shower detection by Cherenkov light typically at optical and ultraviolet wavelengths.

1.6. Imaging Air-Cherenkov Telescopes (IACTs)

For the observation of cosmic-ray air showers and particularly gamma-ray air showers, *imaging air-Cherenkov telescopes (IACTs)* are very suitable instruments. The common principle is to detect Cherenkov photons reflected by a segmented mirror. An array of *photomultiplier tubes (PMTs)* as detector additionally enables the reconstruction of direction. Thus, the air shower can be imaged by Cherenkov light. State-of-the-art IACTs have mirrors with diameters up to 17 m by gaining an angular resolution down to 0.07° [21]. Typically, these IACTs are operating in an energy range of primary gamma rays of $\sim 50 \text{ GeV}$ up to $\sim 10 \text{ TeV}$ [21] whereas there is basically no upper limit for the detectable primary energy.

Established IACT experiments are for instance *H.E.S.S.* (Namibia) [22], *VERITAS* (Arizona) [23], and *MAGIC* (La Palma) [21]. The Cherenkov Telescope Array (CTA) will be a next-generation IACT array operating at two sites at the northern and southern hemisphere. In total, 118 telescopes are planned with three different sizes of 4 m, 12 m, and 23 m. It will extend the observable energy range up to $\sim 100 \text{ TeV}$. [24] An artwork of a possible array is shown in figure 1.7.

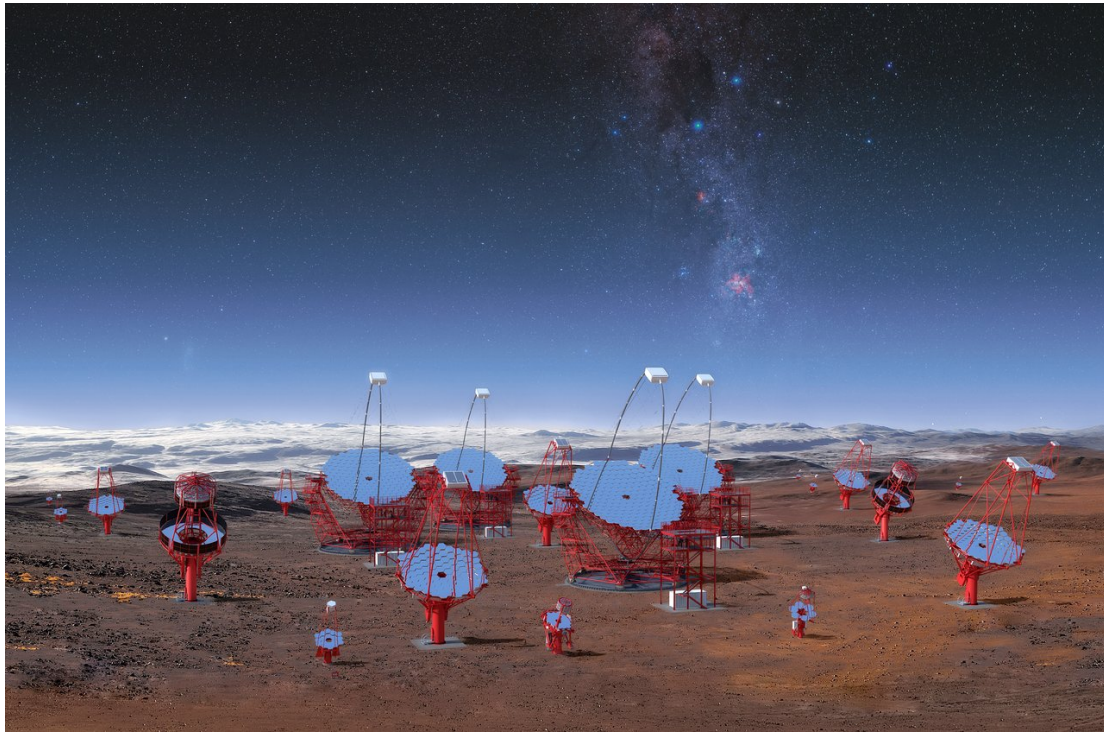


Figure 1.7.: Artwork of the proposed CTA site at ESO’s Paranal Observatory. [25] In this picture, the three classes of IACTs planned are rendered. This CTA site is located at the Paranal Observatory (Atacama desert, Chile) at an altitude of 2100 m a.s.l. administrated by the European Southern Observatory (ESO). The final array layout may be different. [24]

All the IACTs introduced before are large-scale detectors but in principle, the IACT technique allows to build smaller telescopes as well. Obviously, smaller telescopes are associated with lower costs but also with lower efficiency in terms of angular resolution, field of view, etc. However, they are useful as a complementary component for other experiments rather than for a standalone application. Even small IACTs can improve the energy measurement of other ground-based particle detectors since the Cherenkov light yield is proportional to the primary particle energy. Hybrid measurements of IACTs and particle detectors can enhance the energy resolution as recent studies show [8].

In contrast to large IACTs where the camera usually consists of PMTs, smaller IACTs are based on Geiger-mode avalanche photo diodes (G-APDs) or silicon photomultipliers (SiPMs) which are linkages of many G-APDs. These devices are discussed in more detail in section 2.3.3.3. In 2011, the *First G-APD Cherenkov Telescope* FACT started taking data with G-APDs as the first Cherenkov telescope of that kind [26].

As a further step, the reflecting optical system can be replaced by a refracting one with a lens and a camera looking upwards. This principle has been proposed to be the baseline design for multiple compact IACTs like IceAct [4].

1.7. The IceCube Air-Cherenkov Telescopes IceAct

The *IceCube Air-Cherenkov Telescopes IceAct* are one of the proposed extensions of the surface detector IceTop within the scope of IceCube-Gen2. It is planned to be an array of small air-Cherenkov telescopes which are compact and robust to stand the harsh weather conditions at South Pole.

A major purpose of IceAct is to enlarge the veto capabilities of IceTop by reducing the energy threshold down to about 30 TeV [4]. It can also be useful for calibration of IceCube and IceTop and is even able to do cosmic-ray composition measurements, especially together with IceCube and IceTop via different detection channels [27].

The baseline design of IceAct is adapted from the *FAMOUS*³ fluorescence telescope designed for the Pierre Auger Observatory in Argentina. It utilizes silicon photomultipliers (SiPMs, cf. section 2.3.3.3) rather than photomultiplier tubes (PMTs) for the detection of fluorescence light. [28] Since Cherenkov and fluorescence light range in similar wavelength regimes, Cherenkov light detection is possible as well. In addition, a third derivative of FAMOUS – namely *HAWC’s Eye* – has operated together with the HAWC gamma ray observatory. Studies showed that a hybrid measurement of HAWC and HAWC’s Eye could improve the energy resolution significantly [29].

The working principle is the same for all the three telescopes. A Fresnel lens refracts the Cherenkov photons on a focal plane where an array of SiPMs detects the position in the image plane and thus the origin direction. To increase the field of view of the single SiPMs, light concentrators are glued on top – so called *Winston cones*. Figure 1.8 shows an overview sketch of the IceAct telescope with all optical components.

³ First Auger Multi-pixel photon counter camera for the Observation of Ultra-high-energy air Showers

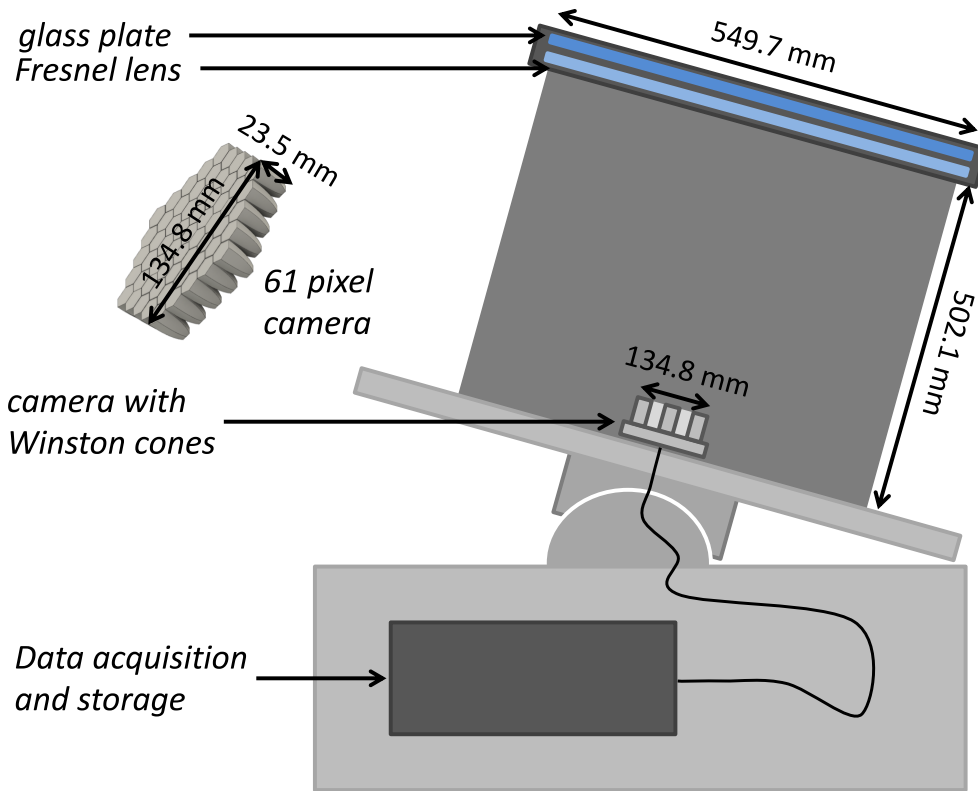


Figure 1.8.: Sketch of the IceAct telescope. [30] The mechanical design of IceAct is based on a carbon tube on a sealed box where the data acquisition system is stored. On top of the tube, a Fresnel lens and a glass plate are fixed. At the focal distance of the lens, the 61-pixel camera is placed. The components are described in more detail in chapter 2.

An additional challenge for IceAct are the already mentioned harsh weather conditions at South Pole. Therefore, some devices are added to the baseline design. One of them is a glass plate on top of the Fresnel lens to protect it from outside influences. In between, the air gap is equipped with a heating cable which should slightly heat the glass plate to free it from ice accumulation. The *data acquisition system (DAQ)* is located underneath the camera in a sealed box – again for protection from the cold environment.

The final IceAct camera consists of 61 SiPMs (cf. section 2.3.3). In 2015, a telescope demonstrator (called *IceACT-2016*) with 7 pixels was deployed on the IceCube Laboratory (ICL) and has been operated in 2016. Analyses of the taken data have proven the concept and the operation at South Pole to be successful [30].

In the northern winter 2018/19, two 61-pixel telescopes were deployed with slightly different DAQ systems and electronic properties. One telescope replaced the previous

one on the ICL. The other one is located on an aluminum stand built on the ice surface.



Figure 1.9.: The IceAct telescope on top of the IceCube Laboratory (ICL). [31] The telescope seen in the picture was deployed in 2017 as a successor of the IceAct 7-pixel demonstrator IceACT-2016.

In this thesis, the focus is on the development of a full telescope simulation with a subsequent parameterization. Thus, the technical properties of the IceAct optics are described in more detail associated with the simulation model in chapter 2.

CHAPTER 2.

The IceAct Model in GEANT4

The optical system of IceAct is modeled in GEANT4. The following chapter will give a view on the material properties and working principles of all optical components.

2.1. GEANT4

GEANT4⁴ is a multi-purpose simulation framework for the passage of particles through matter, written in C++ and developed by the GEANT4 Collaboration at CERN. It includes physics models, geometry, tracking, hits, and digitization. Thus, it allows detailed simulations and response analyses for particle detectors in many application fields like particle and accelerator physics, space engineering, or medical science. In the framework's source, some basic and advanced use cases are implemented and provided as examples. The toolkit is built up of multiple categories (or modules) using each other (cf. figure 2.2). [33]



Figure 2.1.: GEANT4 logo. [32]

⁴ GEometry AND Tracking

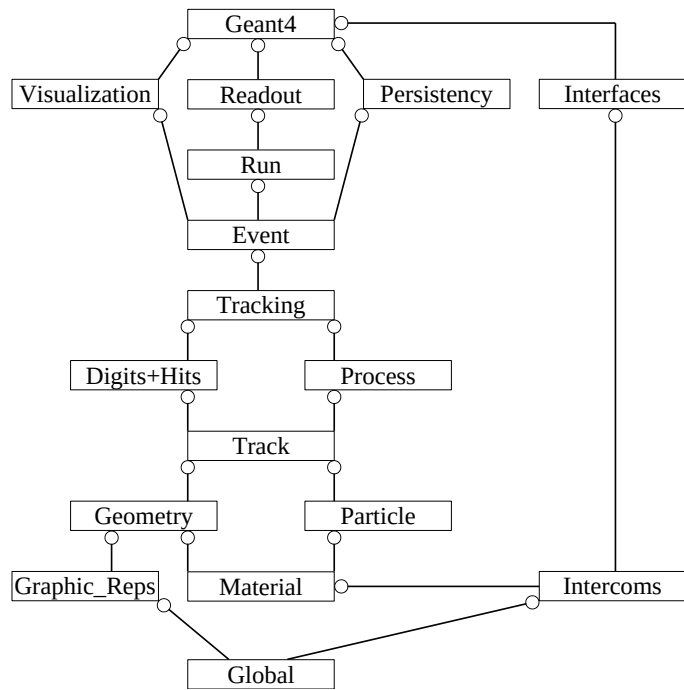


Figure 2.2.: Diagram of relationships between GEANT4 categories. [33, adapted] The circles represent a “using” relation. The category with the circle next to the box uses the linked one.

Especially for IceAct, GEANT4 is capable of simulating Cherenkov (optical) photons, material properties like transmission, reflection, and refraction, as well as detection efficiency properties of the SiPMs.

Since this thesis is about an approach of an all-encompassing telescope simulation, GEANT4 provides all major possibilities to get a distinct analysis of the entire optical system of IceAct.

2.1.1. FAMOUS Telescope Simulation

The fluorescence telescope FAMOUS for the Pierre Auger Observatory in Argentina is developed at RWTH Aachen to measure fluorescence light originating from ultra-high-energy cosmic rays (UHECR) by using silicon photomultipliers (SiPMs) [34]. Within the development, a detailed GEANT4 simulation has been elaborated [35]. The telescope design of FAMOUS is similar since the detection technique and the optics system is basically the same. Therefore, the IceAct telescope simulation is based on this FAMOUS GEANT4 framework. A detailed discourse and a summary of previous analyses can be found in [15].

2.2. Materials

For an optical device, the material that the light should pass has to be chosen deliberately. Especially, the transmission properties, processability, and for IceAct in particular the resistance against harsh weather conditions are of interest.

The glass plate on top of IceAct is made of SCHOTT BOROFLOAT® 33 borosilicate glass. Borosilicate is chosen for its high durability, transparency in the interesting spectral region, flatness, and weak fluorescence intensities. The refractive index is known at certain wavelengths. [36] Since we need to have a full dispersion relation, the points are spline interpolated (cf. orange curve in figure 2.3).

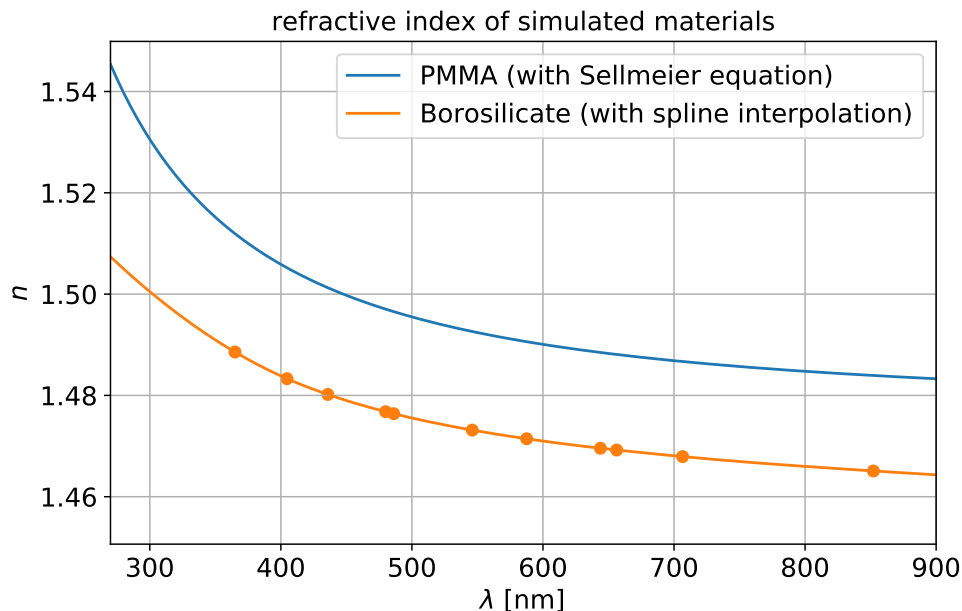


Figure 2.3.: Refractive index of materials used in the simulation. For PMMA the dispersion is calculated by evaluating the Sellmeier equation introduced in this section. The refractive index for the used borosilicate is only given for specific wavelengths [36]. Therefore, splines are used to inter- and extrapolate the full curve.

In the BOROFLOAT® 33 data sheet [36], the transmission properties are given for a vertical light and a glass plate of a thickness of $d = 6.5$ mm. Therefore, the transmission curve $T_{\text{total}}(\lambda)$ includes the internal absorption as well as the two interface transitions into and out of the borosilicate which yields

$$T_{\text{total}}(\lambda) = T_{\text{interface}}^2(\lambda) \cdot T_{\text{internal}}(d = 6.5 \text{ mm}, \lambda). \quad (2.1)$$

The transmission at the interface can be calculated by using the Fresnel equations [37]. In case of perpendicular light, it is

$$T_{\text{interface}}(\lambda) = 1 - \left(\frac{n(\lambda) - n_{\text{air}}}{n(\lambda) + n_{\text{air}}} \right)^2. \quad (2.2)$$

In GEANT4, the wavelength-dependent absorption length $a(\lambda)$ has to be implemented which is given by exponential absorption:

$$I(x) = I_0 e^{-\frac{x}{a}} \Leftrightarrow a = -\frac{x}{\ln \frac{I(x)}{I_0}}. \quad (2.3)$$

Thus, one gets the absorption length by using equations (2.1), (2.2), and (2.3) with

$$\begin{aligned} a(\lambda) &= -\frac{d}{\ln T_{\text{internal}}(d, \lambda)} \\ &= \frac{d}{2 \ln \left(1 - \left(\frac{n(\lambda) - n_{\text{air}}}{n(\lambda) + n_{\text{air}}} \right)^2 \right) - \ln T_{\text{total}}(\lambda)}. \end{aligned} \quad (2.4)$$

This is implemented in the GEANT4 material properties with $n_{\text{air}} = 1$. Figure 2.4 shows the three transmission components as orange lines.

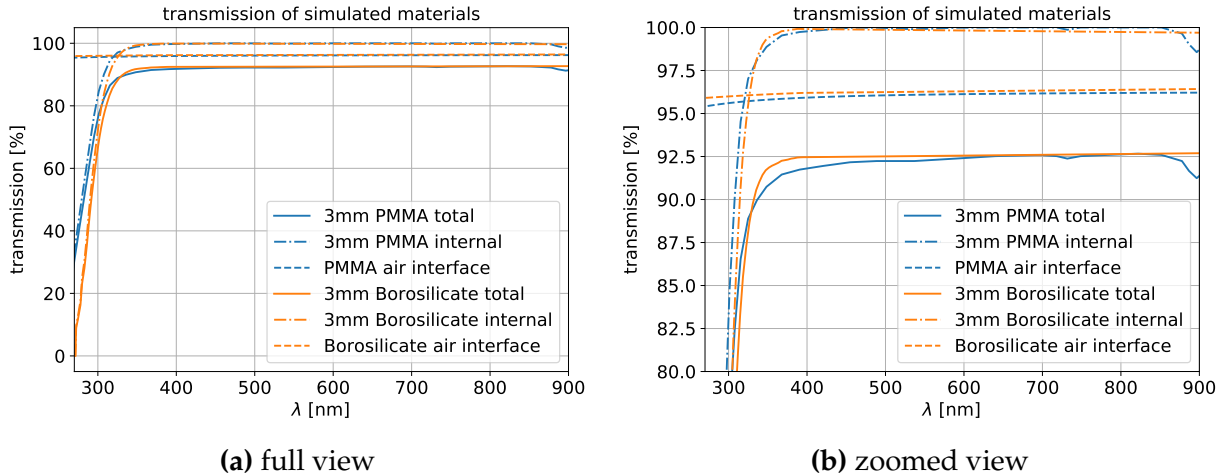


Figure 2.4.: Transmission functions of materials used in the simulation. The total transmission function is the product of internal and two interface transmissions which is evaluated for a perpendicularly incident particle in this plot. Thus, the solid lines represent a complete (perpendicular) transition through a $d = 3$ mm thick layer of the respective material. For a better comparison, the data of internal transmission for borosilicate (given for $d = 6.5$ mm in [36]) is converted for $d = 3$ mm.

The Fresnel lens and the Winston cones in IceAct are made of polymethyl methacrylate (PMMA). The dispersion $n(\lambda)$ can be parametrized with the empirical *Sellmeier equation* [38]. For glasses, the usual form is

$$n^2(\lambda) = 1 + \frac{B_1\lambda^2}{\lambda^2 - C_1} + \frac{B_2\lambda^2}{\lambda^2 - C_2} + \frac{B_3\lambda^2}{\lambda^2 - C_3}, \quad (2.5)$$

with the *Sellmeier coefficients* $B_{1,2,3}$ and $C_{1,2,3}$ [38]. Table 2.1 shows the used coefficients and the function is plotted in figure 2.3 (blue curve).

B_1	0.996 54
B_2	0.189 64
B_3	0.004 11
C_1	0.007 87 μm^2
C_2	0.021 91 μm^2
C_3	3.857 27 μm^2

Table 2.1.: Sellmeier coefficients for PMMA. [39] The above-mentioned coefficients are used in the GEANT4 material properties for PMMA. The related Sellmeier equation (2.5) is plotted in figure 2.3 as blue curve.

For the transmission properties of PMMA, the same method as for borosilicate is used (see above). Therefore, the data stated in [15] is taken as $T_{\text{internal}}(d = 3 \text{ mm})$. Figure 2.4 shows the three transmission components as blue lines.

The tube, back plane and other coating surfaces are simulated as “dummy” material with no reflection or transmission parameters. A particle that hits those surfaces is absorbed and not considered any further.

2.3. Optics

As introduced in section 1.7, IceAct is designed to image the direction of Cherenkov light on a camera consisting of multiple pixels. The imaging is done by a Fresnel lens, and an SiPM-based camera with light collecting “cones” mounted on top. A sketch of the camera layout is shown in figure 2.5.

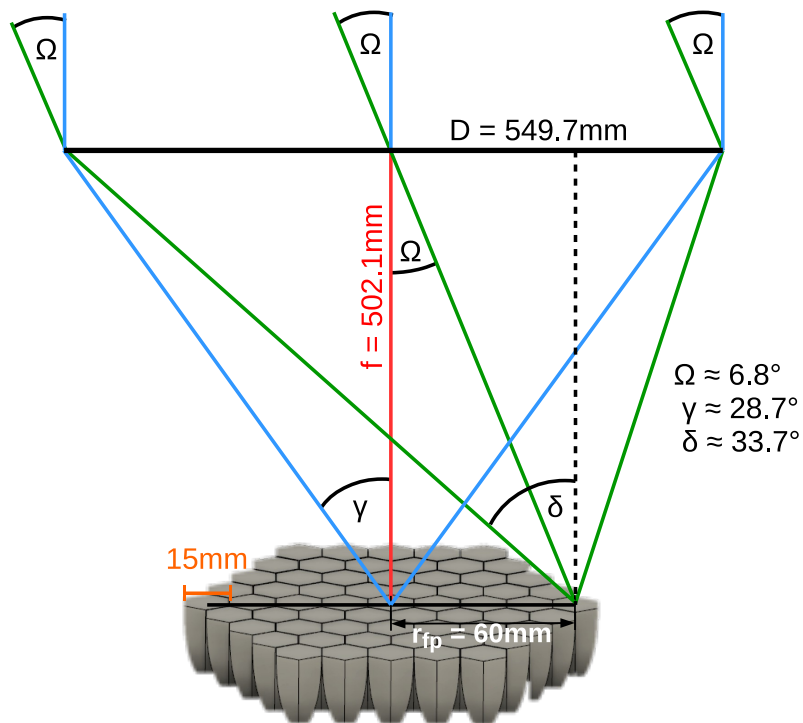


Figure 2.5.: The basic IceAct camera layout. [40] In this sketch, the Fresnel lens with a diameter $D = 549.7$ mm and a focal length of $f = 502.1$ mm focuses rays on the camera sketched below. Additionally, three characteristic angles are shown: the maximum incidence angle of a ray still focused on the camera plane $\Omega \approx 6.8^\circ$, the maximum incidence angle on the central Winston cone $\gamma \approx 28.7^\circ$, and the maximum incidence angle for the outermost Winston cone $\delta \approx 33.7^\circ$.

In the following section, the four optical components of the IceAct GEANT4 model are discussed. Figure 2.6 shows a cross-sectional sketch of the model.

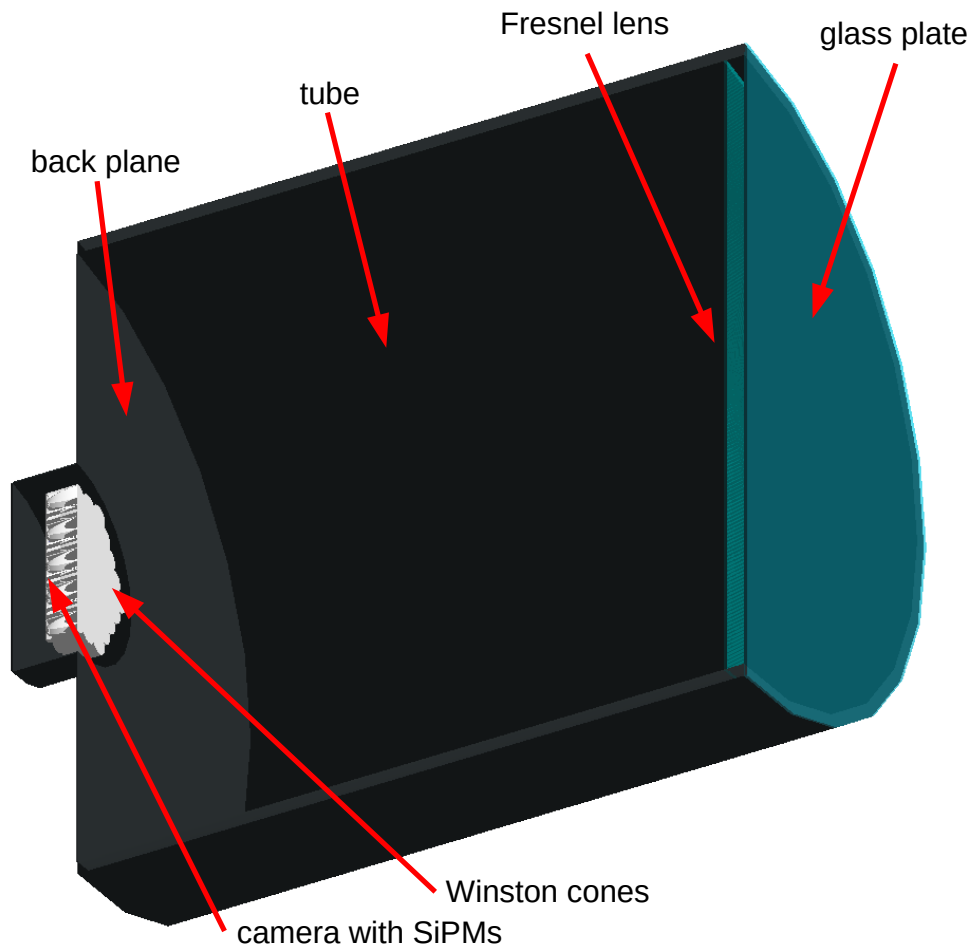


Figure 2.6.: The IceAct GEANT4 model. Cross-sectional sketch of the IceAct optics in GEANT4 with all simulated components. They are described in detail in sections 2.3.2, 2.3.3, and 2.3.1.

2.3.1. Glass Plate

The IceAct glass plate has a thickness of (2.0 ± 0.2) mm, a diameter of (650.3 ± 1.0) mm, and is made of borosilicate as mentioned in section 2.2. It is mounted on top of the tube and its major purpose is to protect the Fresnel lens from the environment. At South Pole conditions, one of the major challenges for the optical system is adherence of snow above the lens which reduces the field of view. In the 12.2 mm thick air gap between glass plate and Fresnel lens, a heating cable is installed to remove snow from the glass surface.

2.3.2. Fresnel Lens

The two major advantages using a Fresnel lens rather than a conventional lens are the significantly less weight and the fact that light passes less material which could absorb it. The main idea of a Fresnel lens is to divide a thick lens into small annular facets in form of prisms that keep the local inclination of the conventional lens by making local approximations of the lens' *sagitta function*⁵. Figure 2.7 visualizes the principle. IceAct uses the model ORAFOL SC 943 with an aperture of 549.7 mm and a focal length of 502.1 mm at a wavelength of (546.0 ± 27.3) nm. The lens is 2.5 mm thick, has 10 grooves per mm, and is made of polymethyl methacrylate (PMMA) as stated in section 2.2. [41]

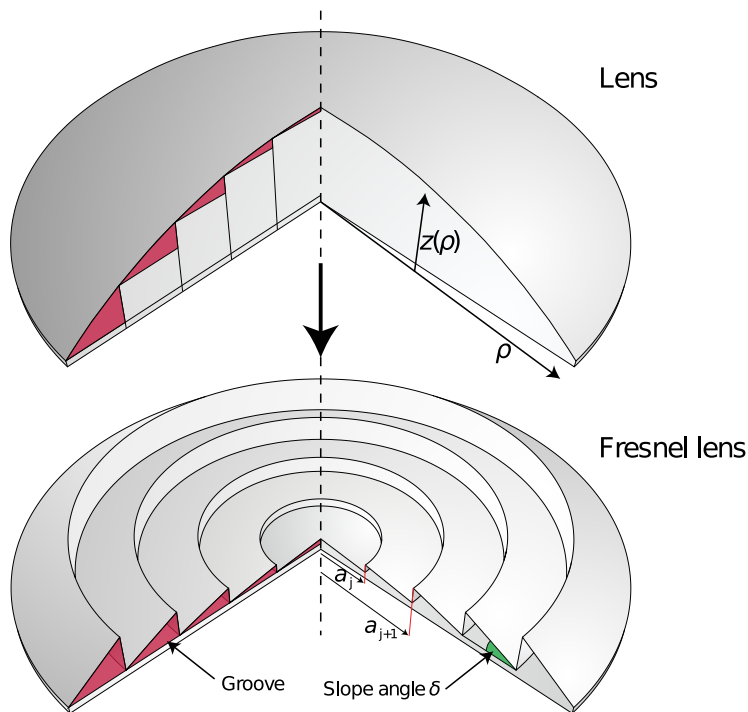


Figure 2.7.: Comparison between a conventional “thick” lens and a Fresnel lens. [42]

For the functionality of a lens the radius-dependent sagitta function $z(\rho)$ is crucial. To get rid of the bulky material of a conventional lens, the Fresnel lens is divided into annular “prisms” called “grooves”. The slope angle δ of each groove is a local approximation of the sagitta function to ensure the imaging capability.

⁵ In application to lenses, the sagitta function $z(\rho)$ gives the lens thickness z as a function of the radial distance ρ from the optical axis for radially symmetrical lenses.

The transmission of a Fresnel lens is not just given by the material properties. Due to the groove structure, there are so called *draft facets* where unwanted refractions, reflections, or transmissions occur. One can compensate for this by adjusting the draft angle ψ (cf. figures 2.8 and 2.9) as a function of the lens radius ρ . Anyway, the molding process – which is the common manufacturing technique of Fresnel lenses – does not allow to have a perpendicular draft facet ($\psi = 0$) due to mold release [43]. This forces the lens to have a minimum draft angle of $\psi_0 = 3^\circ$. With the optimization mentioned before, this leads to a radial dependent draft angle which can be expressed as [15, 42]

$$\psi(\rho) = 3^\circ + 0.0473^\circ \text{ mm}^{-1} \rho. \quad (2.6)$$

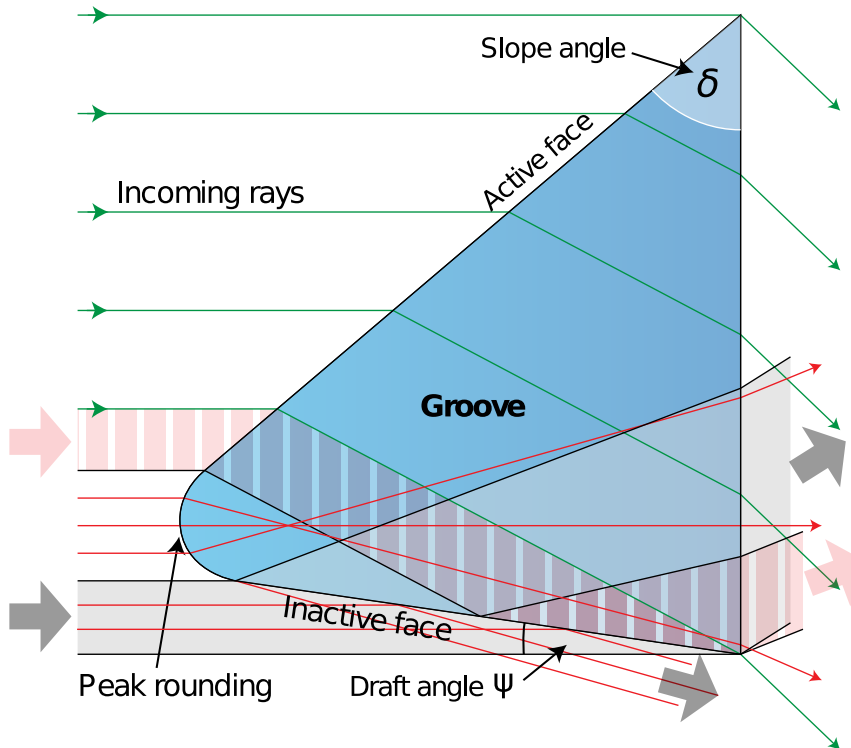


Figure 2.8.: Cross-sectional sketch of a Fresnel groove. [42] Most of the incoming rays are hitting the regular active (or slope) facet of the groove with slope angle δ . For an optimal groove, the inactive (or draft) facet would be parallel to the optical axis. Due to manufacturing process, there is always a small slope on the inactive facet given by the draft angle ψ and the peak is rounded. With this design, there are some impact regions where incoming rays are not refracted to the focal point: if they undergo total reflection at the inactive facet inside the groove (red-dashed region), if they hit the peak rounding (red rays), or if they hit the inactive face (gray region).

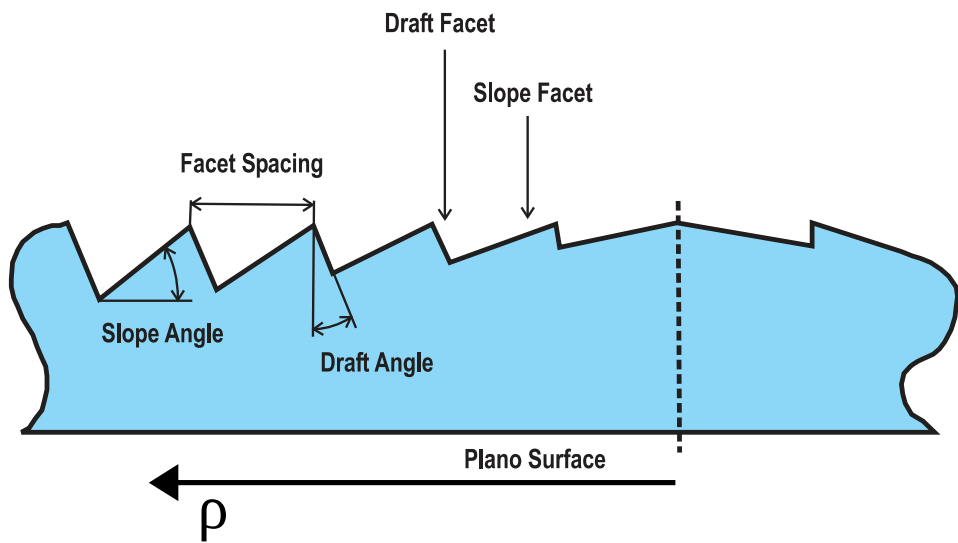


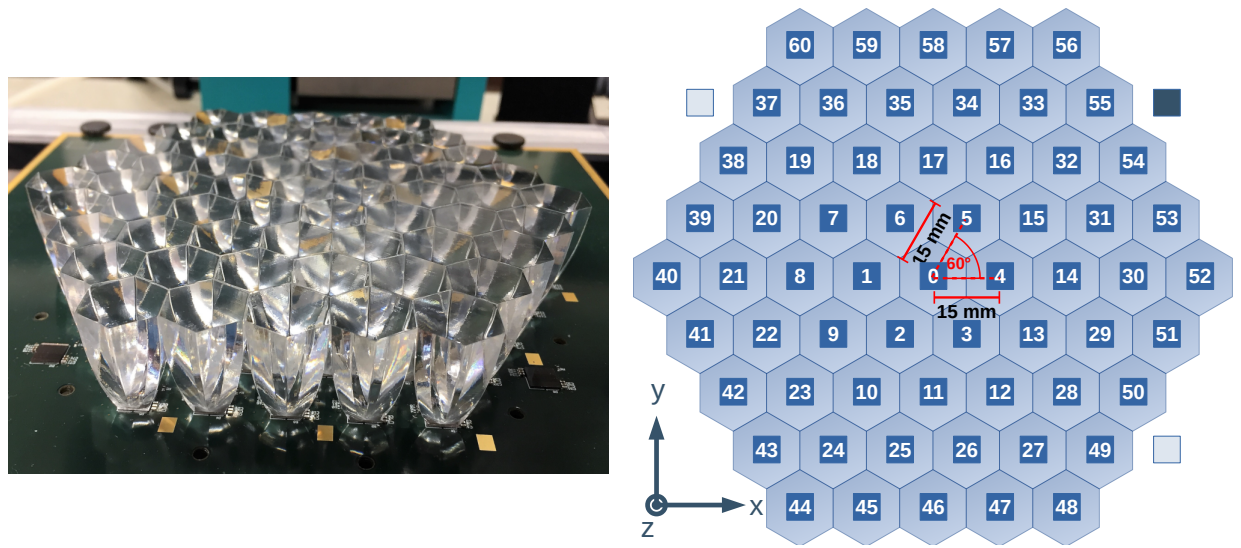
Figure 2.9.: Side-profile sketch of a Fresnel lens. [43, adapted]. Complementary sketch to figure 2.8 which shows the draft angle increase with radius ρ driven by manufacturing.

However, one has to be aware of the fact that approximating a thick lens by a Fresnel lens comes along with losses due to “false” optical projections and results in aberration effects. To quantify the quality of any lens, an important property is the so called *point spread function (PSF)* which describes the energy distribution in the focal plane for a point-like light source at infinite distance – i.e. light parallel to the optical axis. One usually calculates the *aberration radius* r_{90} . It is defined to be the radius of the circle around the PSF centroid which encloses 90 % of the beam energy. One can use the aberration radius for optimizations of the optics. This is described in more detail in section 3.1.2.

The draft angle function (cf. equation (2.6)) is implemented in the Fresnel lens design in GEANT4, the groove peak rounding suggested in figure 2.8 is not. The effect of simulating the rounding is discussed in [42] with the result that a peak rounding radius of 5 μm would slightly enlarge the aberration radius by a few 10 μm . A detailed discussion and measurement of point spread functions and optical aberrations is done in [15] and [42].

2.3.3. Camera

The IceAct camera is the compound of 61 silicon photomultipliers (SiPMs, cf. section 2.3.3.3) arranged in a hexagonal grid together with 61 Winston cones (cf. section 2.3.3.1) glued on them. In addition to the 61 instrumented pixels, there are three pixels aside for reference measurements. Two of them are just placed without Winston cones on top to measure optical noise while one pixel is completely “blind” by being masked. These reference pixels make it possible to measure the optical as well as the pure electronic noise of the SiPM. Figure 2.10a shows an assembled IceAct camera. To address each pixel, they are numbered in a spiral scheme starting with the central “0th” pixel and going outside counterclockwise as seen from the top (cf. figure 2.10b).



- (a) Picture of the assembled IceAct camera. [44] 61 “hex-to-square” Winston cones are glued onto the hexagonal SiPM grid. Besides, one can see two of the overall three additional pixels for reference measurements.

- (b) Placing sketch and pixel numbering of the camera where the 61 pixels are numbered in a spiral scheme starting with the central pixel. The origin of the GEANT4 coordinate system sketched on the bottom left is the entrance window center of the central Winston cone on pixel $i = 0$. In the hexagonal grid, all SiPM centers have a distance of 15 mm to their next neighboring pixels. The bright blue SiPMs are “open” pixels without a Winston cone on top and the dark blue SiPM is a “blind” pixel.

Figure 2.10.: The IceAct camera.

In the following sections, the working principle as well as the implementation in GEANT4 are discussed.

2.3.3.1. Winston Cones – Working Principle

The IceAct telescopes use a light collection technique to enlarge the detection area of the SiPM grid based on *compound parabolic concentrators* (CPCs) [45]. In the following and already mentioned in previous sections, these concentrators are known as *Winston cones*. Primarily, a Winston cone is a rotationally symmetrical paraboloid formed by an off-axis parabola revolving around the axis of symmetry (*CPC axis*, cf. figure 2.11). Hence, the entrance area $A_{\text{en}} = \pi a_{\text{en}}^2$ and the exit area $A_{\text{ex}} = \pi a_{\text{ex}}^2$ are circular.

The concentration effect works for every ray hitting the entrance area up to the maximum incidence angle ϑ_M . A relation between ϑ_M and the characteristic lengths shown in figure 2.11 can be found: [40, 45]

$$\sin \vartheta_M = n \cdot \frac{a_{\text{ex}}}{a_{\text{en}}} , \quad (2.7)$$

with the refractive index n of the cone material. On the one hand, light can be concentrated by using surface reflections in hollow cones ($n = n_{\text{air}} \approx 1$), or – on the other hand – by using internal total reflections in solid cones ($n > 1$). Equation (2.7) shows that the maximum angle can be increased by using a solid cone with a preferably large refractive index.

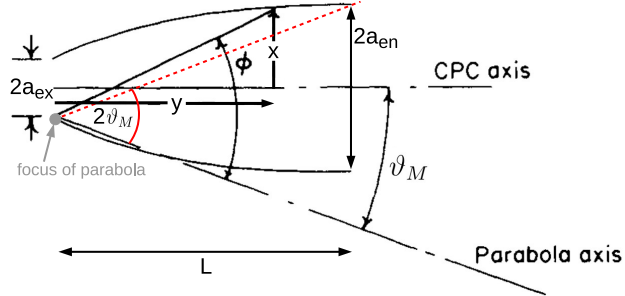


Figure 2.11.: Sketch of a Winston cone. [40] The shape of the cone is given by the two sketched parabolic curves rotating around the CPC axis. Characteristic lengths and angles are indicated: the entrance and exit diameters $a_{\text{en},\text{ex}}$, the cone length L , the maximum incidence angle ϑ_M , the parameterization coordinates (x, y) , and the angle $\phi \in [\vartheta_M, \vartheta_M + 90^\circ]$ needed for parameterization as well.

The parabola describing the Winston cone surface is further called *Winston curve* and can be parameterized by [40, 45]

$$x = \frac{2a_{\text{ex}}(1 + \sin \vartheta_M) \sin(\phi - \vartheta_M)}{1 - \cos \phi} - a_{\text{ex}}, \quad (2.8a)$$

$$y = \frac{2a_{\text{ex}}(1 + \sin \vartheta_M) \cos(\phi - \vartheta_M)}{1 - \cos \phi}, \quad (2.8b)$$

with the cone radius x , the cone length y , and the angle ϕ between the line connecting the parabola focus with a point on the opposite parabola and the parabola axis (cf. figure 2.11).

Another important quantity is the cone length L which is given by [40, 45]

$$L = \frac{a_{\text{ex}}(1 + \sin \vartheta_M) \cos \vartheta_M}{\sin^2 \vartheta_M} \sim \frac{2a_{\text{en}}}{2\vartheta_M}. \quad (2.9)$$

By appropriate design, Winston cones fulfill all requirements for light concentrators in IceAct given by the optical layout (cf. figure 2.5). However, one can design an improved Winston cone for the purposes in IceAct since a hexagonal grid of quadratic pixels with an area of 6 mm × 6 mm is used (cf. figure 2.10b). Instead of a radially symmetrical cone, the IceAct Winston cone is designed in such a way that the exit window fits the SiPM area while the entrance window is hexagonal to maximize the camera's detectional area (cf. figure 2.10a). This design is called *hex-to-square* [40]. A sketch of the IceAct Winston cone is shown in figure 2.12. One can see a green dashed line in it and a pink solid line on the cone's side which follow optimized Winston curves by using the parameterization of equations (2.8).

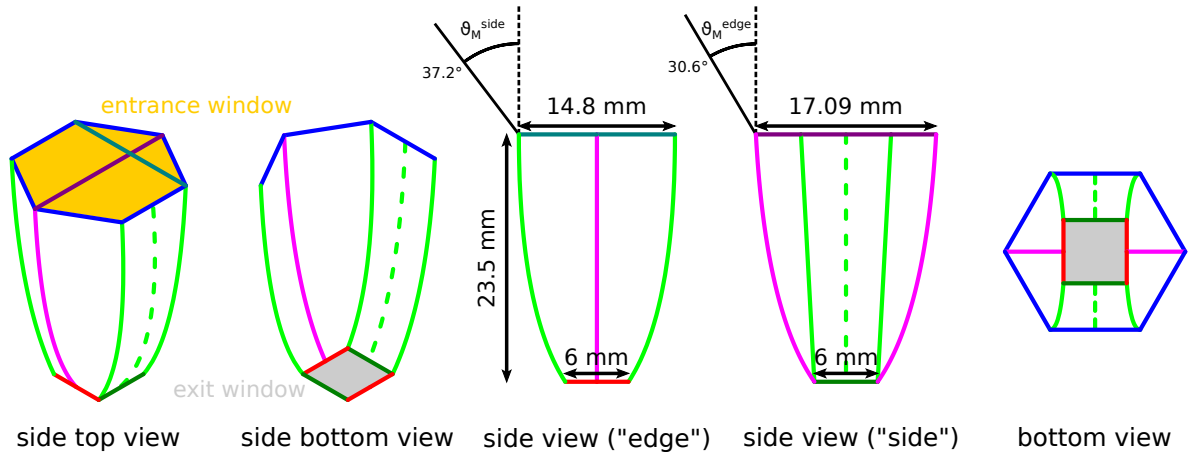


Figure 2.12.: Sketches of the IceAct “hex-to-square” Winston cone. The cone is shown from different points of view with dimensioning. The pink edge and the green dashed surface line follow the optimized Winston curve functions developed in [40]. The green dashed curve is extruded in order to form the whole side. Two different functions result in two different maximum angles $\vartheta_M^{\text{edge},\text{side}}$ for an incidence parallel to the “edge” or the “side” plane.

Hence, the application of Winston cones extend the detectional area of the pixels by a factor of (cf. figure 2.12)

$$\frac{A_{\text{camera with WiCos}}}{A_{\text{camera without WiCos}}} = \frac{61 \cdot \frac{3}{2}\sqrt{3} \cdot \left(\frac{17.09 \text{ mm}}{2}\right)^2}{61 \cdot (6 \text{ mm})^2} \approx 5.27. \quad (2.10)$$

2.3.3.2. Winston Cone Implementation in GEANT4

Due to its complex shape, the cones are implemented in GEANT4 by decomposing their CAD⁶ sketch into small triangular tiles. This process is called *meshing*. For the IceAct Winston cone this is done with the CAD software *FreeCAD*, more precisely with the algorithm *Mefisto*. This meshing routine only needs the maximum edge length of the single tiles as a free parameter. The smaller the maximum edge length the more detailed the mesh gets but the more computational time is needed to translate this mesh into GEANT4. Thus, a good compromise has to be found. Figure 2.13 shows the meshed cone dependent on the maximum edge length. Simulations show a good performance for a maximum egde length of 0.4 mm. Higher lengths result in visible image artifacts (cf. section 3.1.3).

⁶ Computer-aided Design, technique to use a computer for the creation, analysis, etc. of a design.

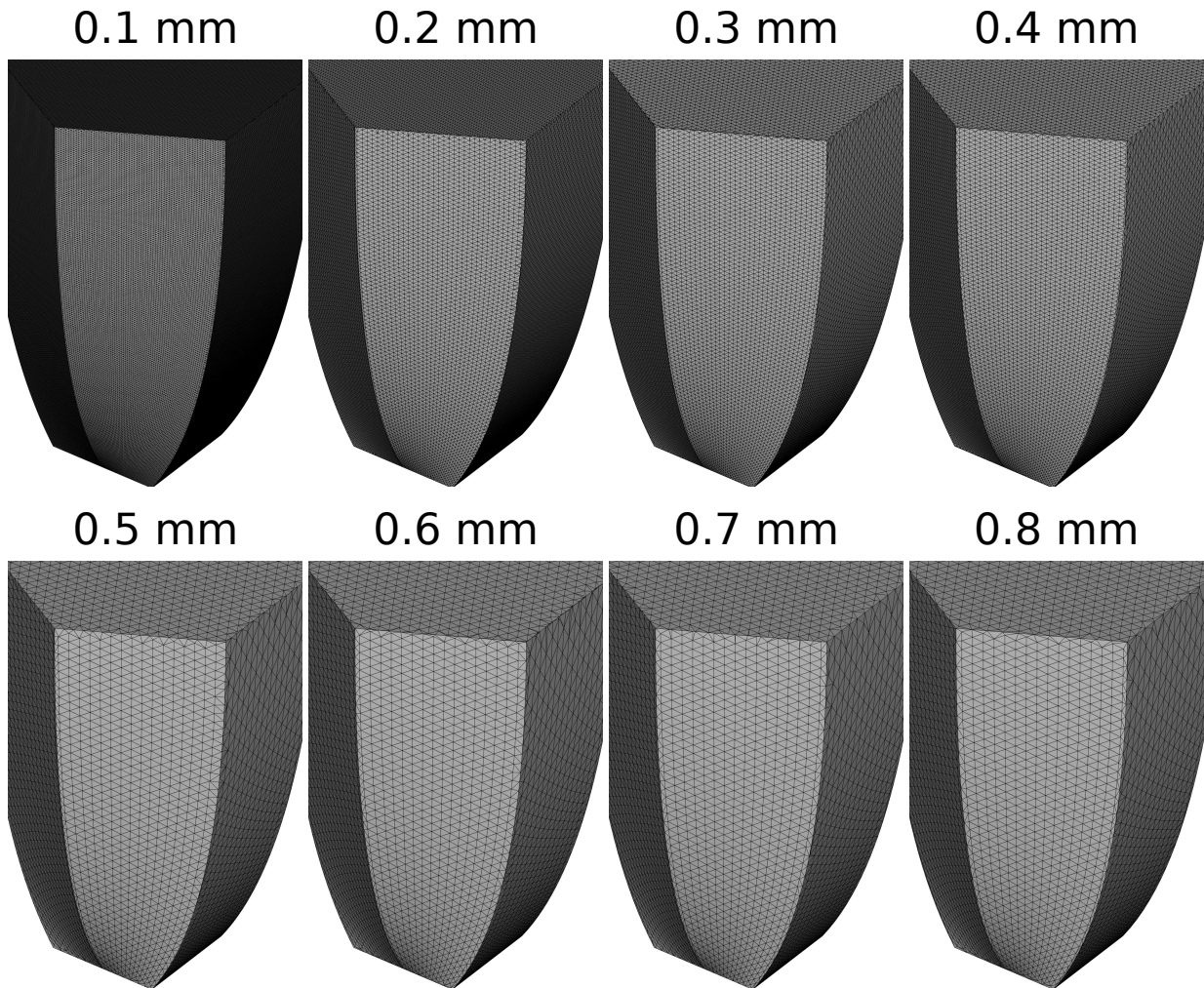


Figure 2.13.: IceAct Winston cone meshing with different maximum edge lengths.

The accuracy increases by reducing the maximum edge length of the tiles. The length of 0.4 mm is used in the simulation.

The meshed geometry is then translated into GEANT4 by using the toolkit *CADMesh* [46]. More about Winston cone meshing is discussed in section 3.1.3.

2.3.3.3. Silicon Photomultipliers (SiPM)

Silicon photomultipliers (SiPMs) are semiconductor devices used for photon detection in multiple applications. In comparison to conventional photon detection devices like *photomultiplier tubes (PMTs)*, they are rather compact and offer a higher photon detection efficiency. These features made them interesting devices for application in imaging detectors.

An SiPM is the composition of an array of so called *Geiger-mode avalanche photo diodes*

(G-APDs). Their working principle is based on *p-n*-junctions (cf. figure 2.14). This is the simple configuration when an *n*-doped and a *p*-doped material are brought together. Thus, a *depletion zone* occurs where free electrons of the *n*-doped material fill holes of the *p*-doped material. Due to the resulting net charge, an electric field arises from the *n*- to the *p*-doped side comparable to a capacitor. The size of the depletion zone can be enlarged by an external *bias voltage* V_{bias} applied with the anode side at the *n*-doped material. In this state, the junction conducts current easily in one direction only which is commonly known as a *diode*. [47]

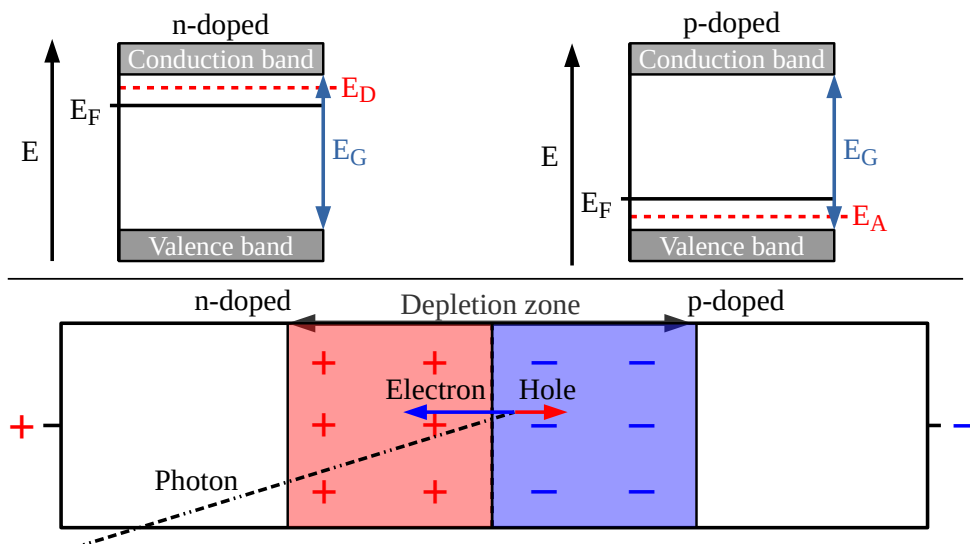


Figure 2.14.: Sketch of a *p-n*-junction. [40] In the top, the energy bands are shown for *n*-doped and *p*-doped semiconductor with the Fermi energy level E_F , the gap energy E_G , and the donor or acceptor energy level E_D and E_A respectively. Below, a *p-n*-junction is sketched. An incident photon may result in production of an additional electron-hole-pair inducing a current via avalanches.

If a photon now traverses the diode, a possible impact can ionize an atom and thus produce an electron-hole-pair. While the electron is accelerated along the electrical field, it can ionize further atoms if the electric field is strong enough – an avalanche is formed that induces a highly temperature-dependent breakdown voltage $V_{\text{breakdown}}$. Here, the “Geiger-mode” prefix additionally indicates that the signal is not dependent on the number of total detected photons. A *quenching resistor* allows to stop the avalanche and enables the cell to recover quickly. This working principle is referred to as an *avalanche photo diode (APD)*. Usually, photo diodes are based on germanium (Ge) or silicon (Si). Since the band gap of silicon-based photo diodes is higher (1.12 eV) than for germanium-based ones (0.67 eV), the electrons in silicon-based photo diodes need

higher energies to produce a significant photo current. Thus, Si photo diodes generate less noise than photo diodes based on Ge. [48] An important operation parameter of a G-APD is the *over voltage* V_{OV} since many features (e.g. the gain) of G-APDs are proportional to it. It is defined as the difference of bias and breakdown voltage [48]

$$V_{OV} = V_{bias} - V_{breakdown}. \quad (2.11)$$

Basically, there are two types of G-APD cells: *p-on-n* which is shown in figure 2.15 and *n-on-p*. They differ in the wavelength region they are efficient in. While *n-on-p* cells are efficient for wavelengths beyond $1\mu\text{m}$, the *p-on-n* cells operate best in the blue and UV regime – thus in the peak region of Cherenkov light (cf. figure 1.5).

The step from a G-APD to an SiPM is done if one now combines many G-APDs in a grid structure in parallel connection which is shown in figure 2.16. Figure 2.17 shows measured waveforms (or “pulses”) of SiPM with linear amplification. A discretization of puls heights which correspond to the number of single cell breakdowns can be observed. The amplitude A_i of a standard pulse is proportional to the capacitance C and anti-proportional to the electron charge q and the over voltage V_{OV} , [48]

$$A_i \propto \frac{C}{qV_{OV}}. \quad (2.12)$$

If now multiple cell breakdowns occur, the total pulse height just sums up over the number of triggered cells which is commonly known as *PE* (*photo electron equivalent*), [48]

$$A = \sum_{i=0}^{PE} A_i. \quad (2.13)$$

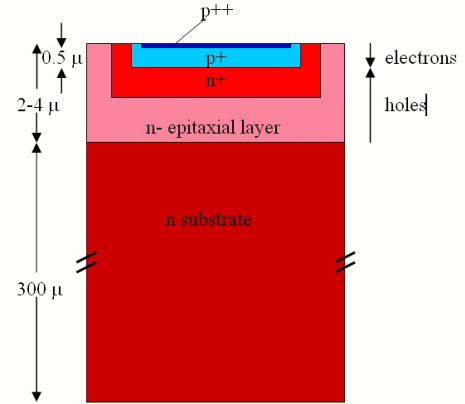


Figure 2.15.: Sketch of a “p-on-n” G-APD cell. [48] This type is optimized to have a high photon detection efficiency in the blue and UV wavelength regime.

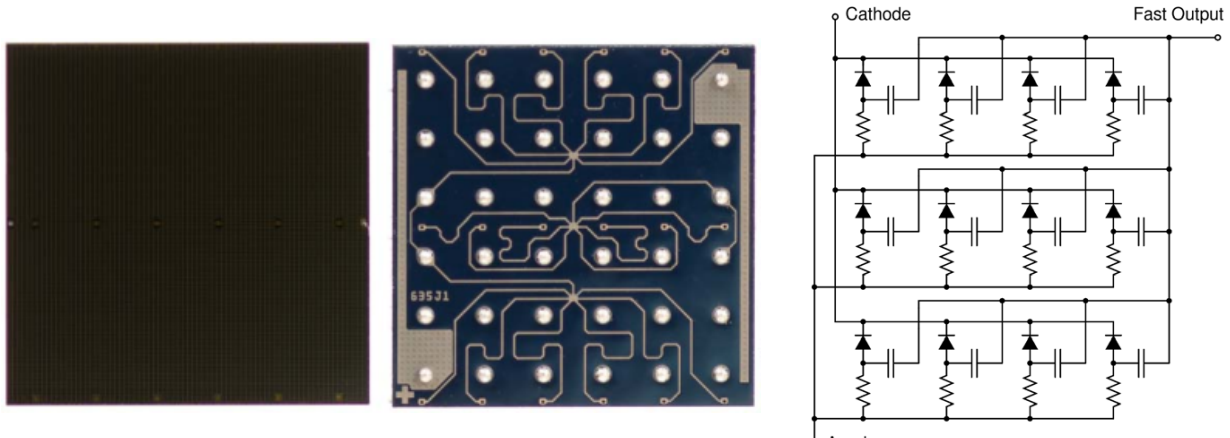
- 
- (a) Picture of the MicroFJ-60035-TSV SiPM which is used in the IceAct camera as seen from the top (left) and the back (right). One can slightly see the fine grid of 22 292 G-APDs with a size of $35\text{ }\mu\text{m} \times 35\text{ }\mu\text{m}$ arranged on a package with the dimensions $6.07\text{ mm} \times 6.07\text{ mm}$.
- (b) Circuit diagram of a SiPM with 12 (very few) G-APD cells in parallel connection. One can see that each cell has its own quenching resistor. The fast output is not used in the application for IceAct.

Figure 2.16.: Structure of an SiPM. [49]

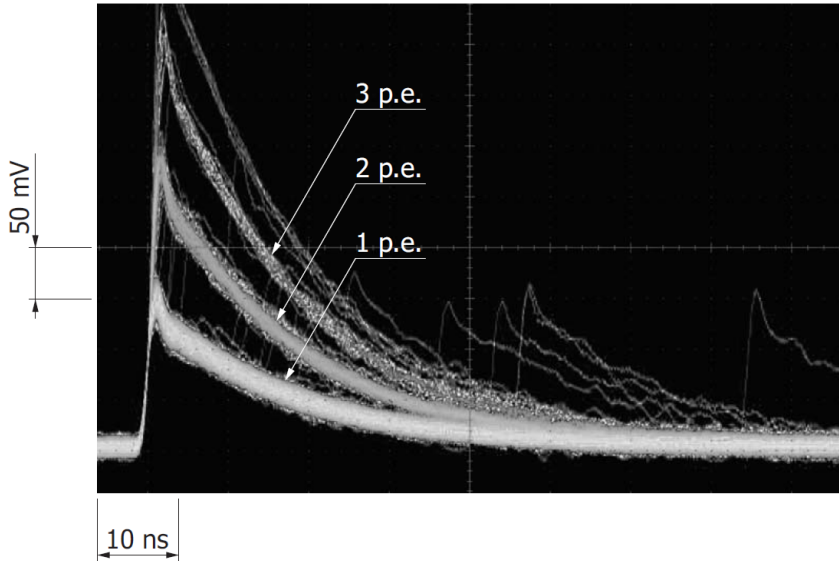


Figure 2.17.: Pulse waveforms of an SiPM. [50] Multiple measured SiPM waveforms (“pulses”) with amplitude plotted against time. A discretization of pulse heights can be observed which is dependent on the number of single cell breakdowns marked with “p.e.” in the plot. One can see a few after pulses at later times as well.

In addition, the pulse shape can be parameterized by a function of two exponential functions, [51]

$$A(t, PE) = c \cdot PE \cdot \left(1 - \frac{1}{1 + \exp\left(\frac{t-t_0}{\tau}\right)} \right) \cdot \exp\left(-\frac{t-t_0}{\lambda}\right), \quad (2.14)$$

where c is a calibration factor that corresponds to the amplitude of a 1 PE pulse, t_0 is the starting time of the pulse, and τ and λ are the rise and fall times respectively which are typically in a range of $\tau = 0.9 \text{ nm}$ to 1.1 nm and $\lambda = 18 \text{ ns}$ to 20 ns . [51]

Moreover, figure 2.16a shows the SiPM used for the IceAct camera. It is the *MicroFJ-60035-TSV SiPM* by *ON Semiconductor*⁷ consisting of 22 292 G-APD cells with the dimensions $35 \mu\text{m} \times 35 \mu\text{m}$ each. The active area is $6.07 \text{ mm} \times 6.07 \text{ mm}$ and the package area is $6.13 \text{ mm} \times 6.13 \text{ mm}$ which results in a fill factor⁸ of $\epsilon_{\text{fill}} = 75\%$. On top of the active area, a glass window with a thickness of 0.37 mm (cf. figure 2.18) is mounted. These and more technical properties can be found in the data sheet [49].

⁷ In former theses and publications on IceAct the SiPM is called SensL J-Series 60035. Since 2018, SensL is fully integrated in the head organization ON Semiconductor which took over the sales of SensL products.

⁸ Percentage of the active area that is actually equipped with cells.

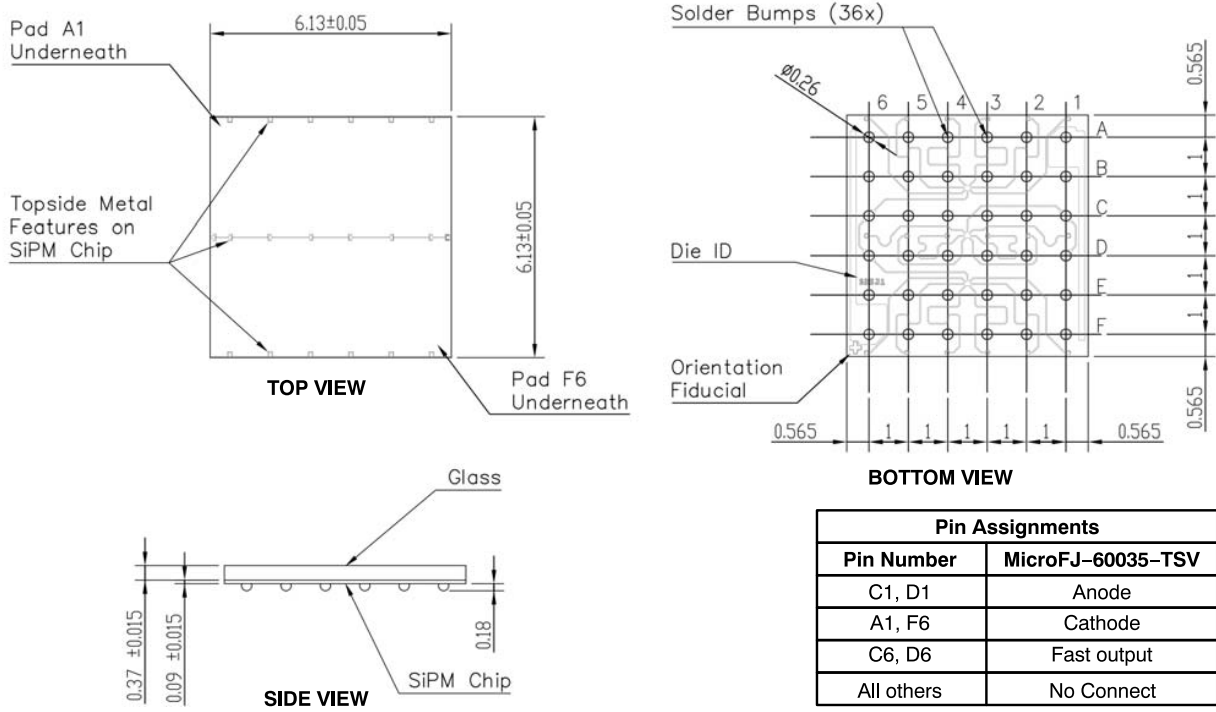


Figure 2.18.: Technical sketch of the MicroFJ-60035-TSV SiPM used in IceAct. [49] All dimensions given in mm.

2.3.3.4. SiPM Implementation in GEANT4

In the IceAct GEANT4 simulation, the SiPM is implemented via the plug-in G4SiPM [52]. It allows a convenient implementation of geometry, materials, photon detection efficiency, and many other physics and performance parameters in GEANT4. It is even possible to do waveform simulation with background from cross talk, after pulses, thermal noise, etc. Since the signal simulation is beyond the scope of this thesis, only the material and detection properties are of interest.

For the material properties of the 0.37 mm thick covering glass plate on the SiPM, only the refractive index of $n = 1.53$ at a wavelength of $\lambda = 436$ nm is given in the data sheet [49]. Since there are no detailed information about the glass, n is assumed to be constant for the simulation.

The other important property is the *photon detection efficiency* $PDE(\lambda, V_{OV})$ which is given for the over voltages $V_{OV} = 2.5$ V and $V_{OV} = 6$ V and for wavelengths $\lambda = 200$ nm to 900 nm. In IceAct, the SiPMs are operated with an over voltage of $V_{OV} = 5$ V. Measurements in the data sheet show that the relation between over voltage and PDE is

linear [49]. Therefore, one gets the needed $PDE_{5V} := PDE(\lambda, V_{OV} = 5\text{ V})$ by linear interpolation as

$$PDE_{5V} = PDE_{2.5V} + \frac{2.5\text{ V}}{6\text{ V} - 2.5\text{ V}} \cdot (PDE_{6V} - PDE_{2.5V}), \quad (2.15)$$

which is then implemented in GEANT4. In addition, G4SiPM takes into account that the PDE is measured for perpendicular light incidence in air environment. By using Fresnel equations, it compensates for slant photon incidences. The fill factor ϵ_{fill} is also divided out. [15, 52]. The interpolated and original PDE functions are shown in figure 2.19

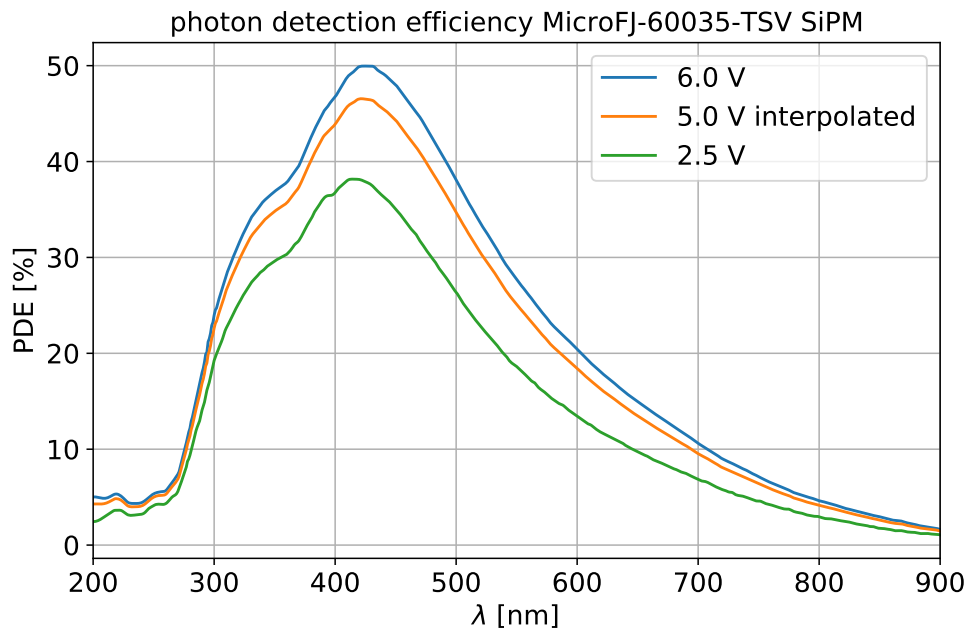


Figure 2.19.: Photon detection efficiency of the MicroFJ-60035-TSV SiPM. The data for over voltages of 6 V and 2.5 V is taken from [49], the curve for 5 V – which is used in the GEANT4 simulation – is interpolated linearly.

CHAPTER 3.

IceAct Simulation

This chapter will discuss the GEANT4 simulation process. At first, simulations of the single optical components are studied in order to find appropriate parameters and settings for the whole optical system. Afterwards, an overall simulation is performed for the final goal of IceAct parameterization.

3.1. Getting to Know the IceAct Optics

In this section, the optical properties of IceAct are investigated in order to optimize their parameters. Possible uncertainties and aberration effects in the IceAct optics are examined by focusing on the single components: on the one hand, the effect of mounting a glass plate on top of the Fresnel lens is discussed. On the other hand, the approximation of the Winston cones by a tessellated structure might imply some aberrations or artifacts.

3.1.1. “Best” Wavelength

Many of the IceAct telescope properties have (non-linear) wavelength dependencies (cf. section 2.2). Additionally, the Cherenkov spectrum is wavelength dependent as well (cf. figure 1.5). By implication, there has to be a wavelength λ^* that IceAct is the most efficient for. One can determine λ^* by looking at the following limiting functions.

- **The Cherenkov spectrum.** The data shown in figure 1.5 (La Palma, 2200 m a.s.l.) is chosen.

- **The internal transmission function of PMMA.** It is assumed that a photon has to pass approximately 30 mm of PMMA to get to the SiPMs. Thus, the internal transmission function shown in figure 2.4 as blue dotted-dashed line has to be exponentiated by 10 to hold for this case.
- **The internal transmission function of borosilicate,** i.e. the material of the glass plate. The photons have to pass approximately 2 mm. Exponentiation of a factor $\frac{2}{3}$ of the orange dotted-dashed line in figure 2.4 leads to the desired function.
- **The photon detection efficiency (PDE) function of the SiPMs** interpolated for $V_{OV} = 5$ V (cf. orange curve in figure 2.19).

All of these functions are normalized – i.e. divided by their own maximum – and then multiplied which results in a new (relative) efficiency function. The maximum of this function again is further named “best” (or most efficient) wavelength and found to be $\lambda^* = 411$ nm. Figure 3.1 shows the procedure graphically.

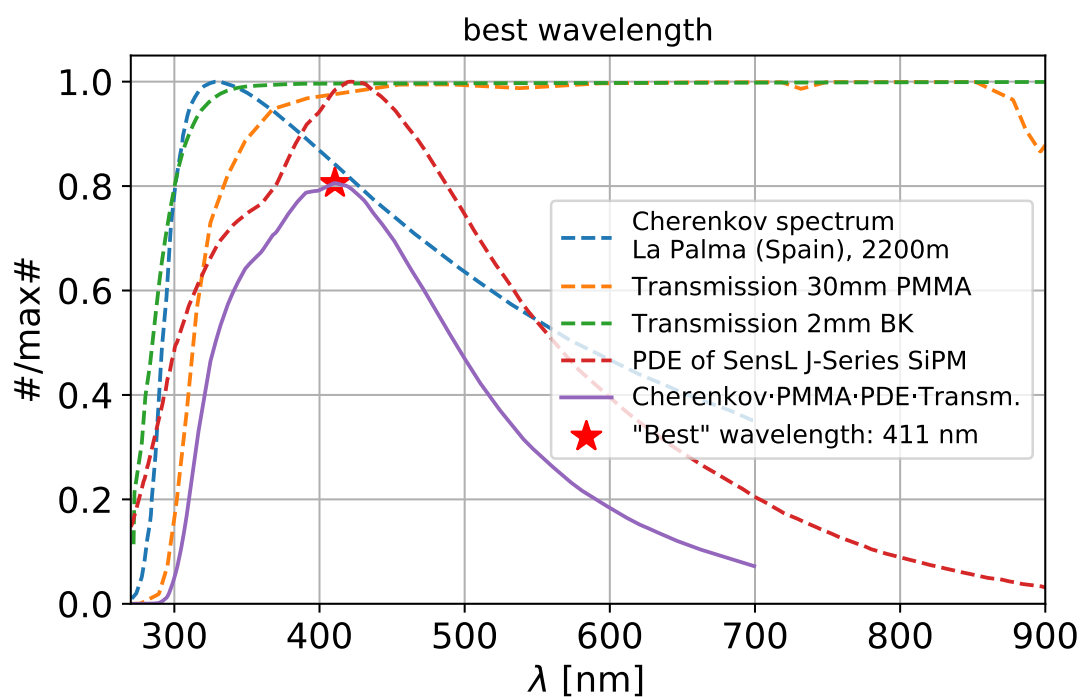


Figure 3.1.: “Best” wavelength. All limiting functions (Cherenkov spectrum, material transmission curves, and photon detection efficiency) are normalized to each maximum and multiplied. The maximum of the product is defined to be the “best”, i.e. most efficient, wavelength $\lambda^* = 411$ nm.

3.1.2. Focal Plane Shift

So there is a most efficient wavelength for the IceAct telescope as shown in the last section 3.1.1. As stated in section 2.3.2 and in the ORAFOL data sheet [41], the focal distance of the Fresnel lens $z_f = 502.1$ mm is given for a certain wavelength $\lambda = (546.0 \pm 27.3)$ nm. Thus, the focal distance at $\lambda^* = 411$ nm may be different which gives a possibility for potential improvement for the optical properties of IceAct. To investigate a shift of the focal plane, one has to define a quantity to optimize. In this simulation, the aberration radius r_{90} is used for this purpose (cf. section 2.3.2). A point spread function (PSF) measurement of the Fresnel lens for monochromatic light with $\lambda = 546$ nm and different incidence angles θ is done in [15] by using ray tracing simulation. In this thesis, a PSF simulation is done as well but for wavelengths between 270 nm and 900 nm and vertical incidence $\theta = 0^\circ$. The focal plane is fixed at the focal distance $z_f = 502.1$ mm. In total, a vertical beam of 10^8 photons with uniformly density and uniformly distributed wavelengths in the interval given above is simulated. On the focal plane, the wavelength λ_{hit} , position $(x_{\text{hit}}, y_{\text{hit}})$, and angle $(\theta_{\text{hit}}, \phi_{\text{hit}})$ of the detected photons are registered. The goal is to measure the minimal aberration radius at the suggested focal distance $z_f = 502.1$ mm and a possible focal plane shift in order to minimize the aberration radius for $\lambda^* = 411$ nm.

For the first measurement, the aberration radius is evaluated by calculating the 90 %-quantile of the distances r_{hit} between the hit position and the optical axis⁹ given by

$$r_{\text{hit}} = \sqrt{(x_{\text{hit}} - x_{\text{centroid}})^2 + (y_{\text{hit}} - y_{\text{centroid}})^2} \stackrel{(x,y)_{\text{centroid}}=(0,0)}{=} \sqrt{x_{\text{hit}}^2 + y_{\text{hit}}^2}. \quad (3.1)$$

By doing this for small wavelength ranges, one gets a wavelength-dependent aberration radius $r_{90}(\lambda)$ on the focal plane. As a result, a minimal aberration radius of 1.78 mm is reached at a wavelength of 403 nm. Figure 3.2 shows $r_{90}(\lambda)$.

⁹ Normally, this is the centroid rather than the optical axis but in the case of parallel light, the centroid is assumed to be at $(x, y) = (0, 0)$.

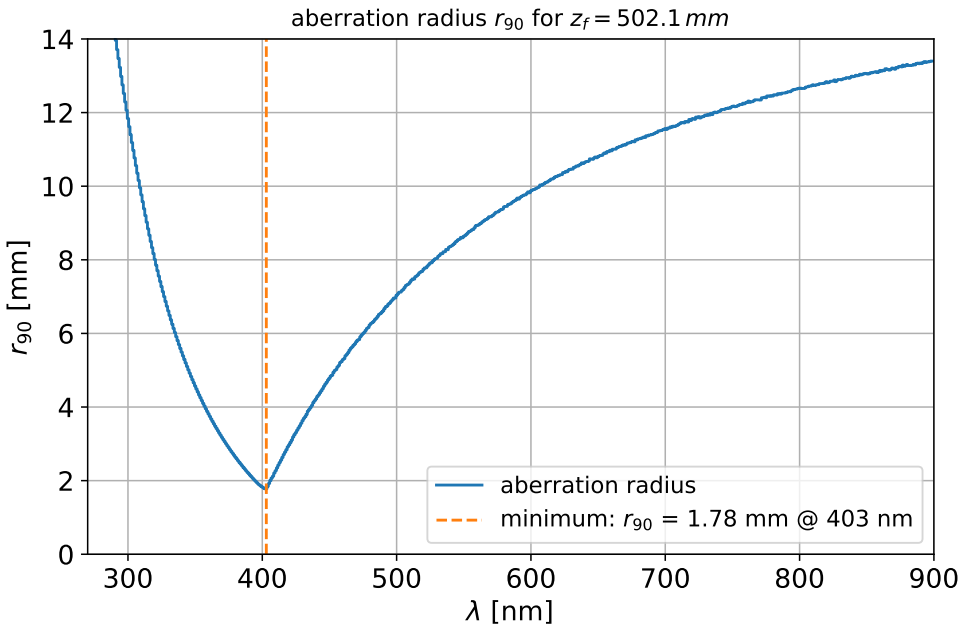


Figure 3.2.: Aberration radius on the focal plane. r_{90} is calculated for vertical light as a function of the wavelength. The focal distance is fixed to $z_f = 502.1$ mm. The minimal aberration radius of 1.78 mm is reached at a wavelength of 403 nm.

For the focal plane shift, one considers a small wavelength range and again calculates the aberration radius. Since the incidence angles on the focal plane are known, one can calculate the point of incidence for a hypothetical focal plane at a position of $z_f + \Delta z$, where Δz is the focal plane shift. A trigonometrical approach yields

$$r_{\text{hit}}(\Delta z) = \sqrt{(x_{\text{hit}} - \Delta z \tan \theta_{\text{hit}} \cos \phi_{\text{hit}})^2 + (y_{\text{hit}} - \Delta z \tan \theta_{\text{hit}} \sin \phi_{\text{hit}})^2}. \quad (3.2)$$

Thus, the aberration radius can be calculated for each focal plane shift Δz and wavelength λ . An optimal focal plane shift can then be found by minimizing the aberration radius. Figure 3.3 shows this calculation for different wavelengths by evaluating the beam *caustic*¹⁰ for different focal plane shifts. One can clearly see that the focal length increases with wavelength. Additionally, figure 3.4 shows a zoomed-out version of figure 3.3b. In particular for the most efficient wavelength $\lambda^* = 411$ nm, a resulting marginal focal plane shift of $\Delta z = 1.25$ mm shows that the standard focal distance is already quite good for the purposes of IceAct. Nevertheless, the small focal plane shift is considered in the final parameterization simulation.

¹⁰ In this context, caustic means the photon density distribution along the optical axis. Usually in beam optics, a caustic just describes the envelope of the beam.

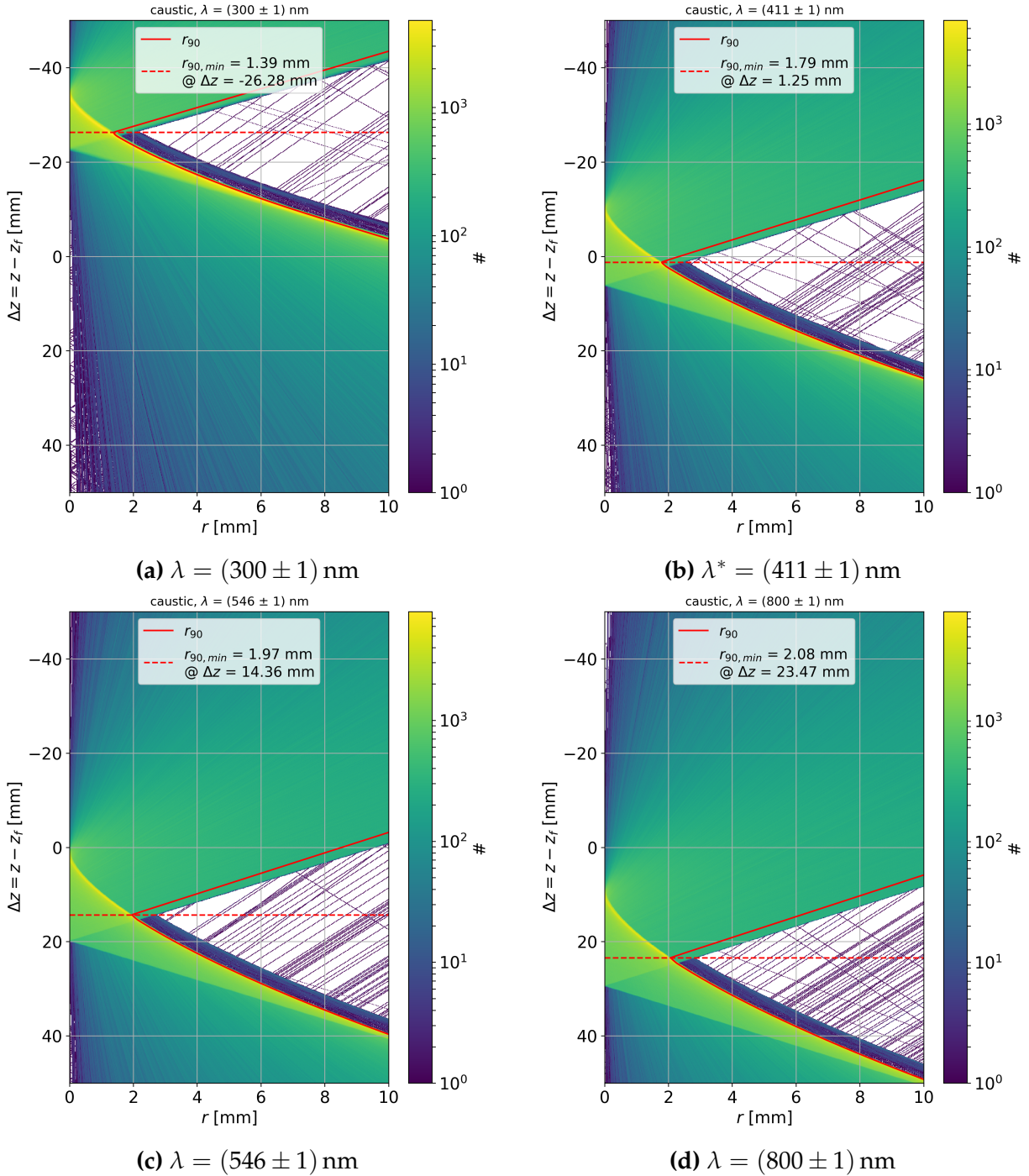


Figure 3.3.: Caustic histograms for the focal plane shift. For focal plane shifts Δz between -50 mm and 50 mm, the incident positions of simulated photons are histogramized by calculating their distance from the optical axis $r_{\text{hit}}(\Delta z)$. This results in a photon density plot called *caustic*. A focal plane shift of $\Delta z = 0$ is equivalent to the “standard” focal distance $z_f = 502.1$ mm. A positive Δz connotes a shift away from the lens. Thus, the lens is located on top of the shown plots. The calculation is done for different wavelengths, especially for the “best” wavelength in (b) and for the wavelength which the focal distance is set for in (c). The red line shows the aberration radius $r_{90}(\Delta z)$ and the focal plane shift where its minimum is reached marked by the red dashed line.

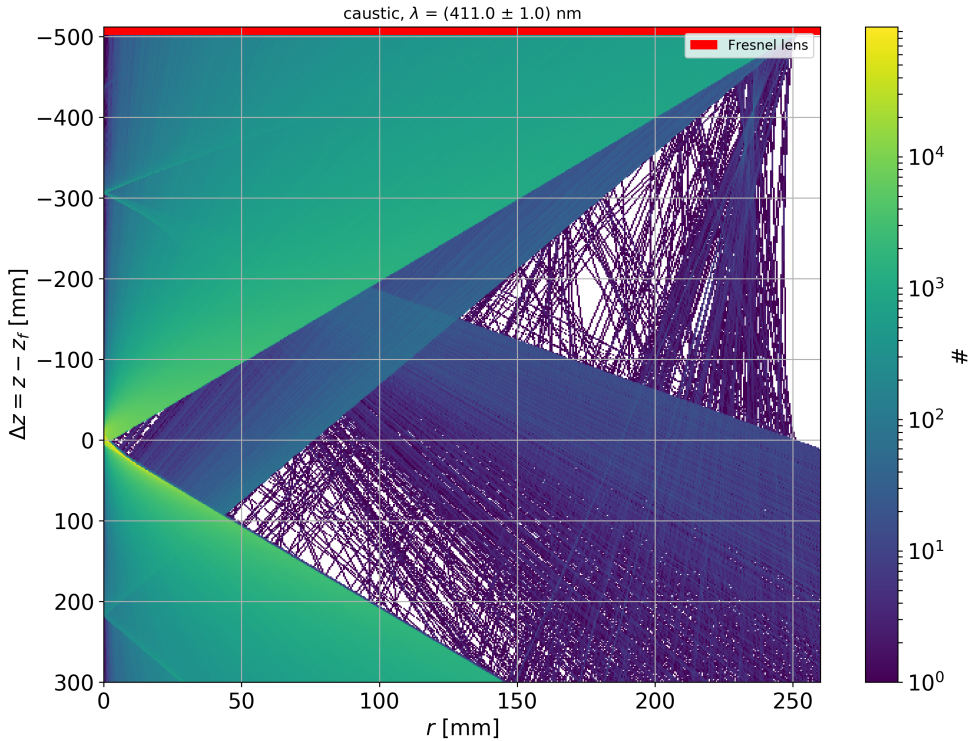


Figure 3.4.: Zoomed-out caustic histogram. The plot shows a zoomed-out version of figure 3.3b. The red band on the top denotes the location of the Fresnel lens. Besides a major focal spot at $\Delta z \approx 0$ mm, one can see two minor ones at $\Delta z \approx -300$ mm and $\Delta z \approx 220$ mm which come from the “false” refractions mentioned in section 2.3.2.

3.1.3. Winston Cone Meshing

As already brought up in section 2.3.3.2, the *mesh size* m – i.e. the maximum edge length of the meshed Winston cone model – has to be chosen as a compromise between imaging quality and computational effort. For the IceAct parameterization, especially the light collection capability of the Winston cone is necessary rather than its actual imaging quality. Nevertheless, the meshing is chosen to have a sufficiently high level of detail to avoid coarse imaging artifacts. Figure 3.5 shows very obviously that artifacts get coarser for higher mesh sizes.

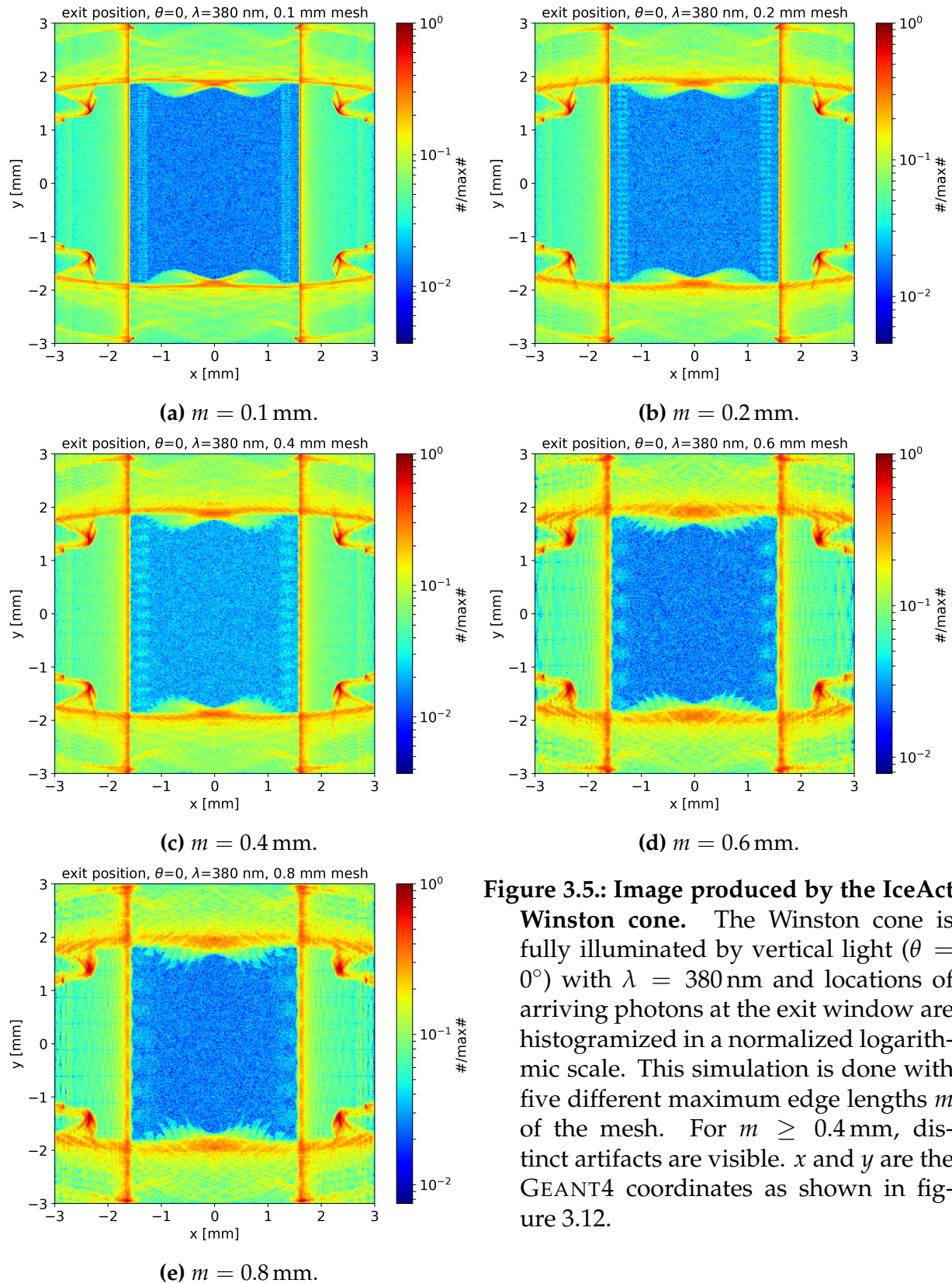


Figure 3.5.: Image produced by the IceAct Winston cone. The Winston cone is fully illuminated by vertical light ($\theta = 0^\circ$) with $\lambda = 380 \text{ nm}$ and locations of arriving photons at the exit window are histogramized in a normalized logarithmic scale. This simulation is done with five different maximum edge lengths m of the mesh. For $m \geq 0.4 \text{ mm}$, distinct artifacts are visible. x and y are the GEANT4 coordinates as shown in figure 3.12.

In order to compare the meshed Winston cone with the exact CAD model, the GEANT4 simulation is contrasted with the Zemax¹¹ simulation done in [40]. Figure 3.6 shows a quite high similarity.

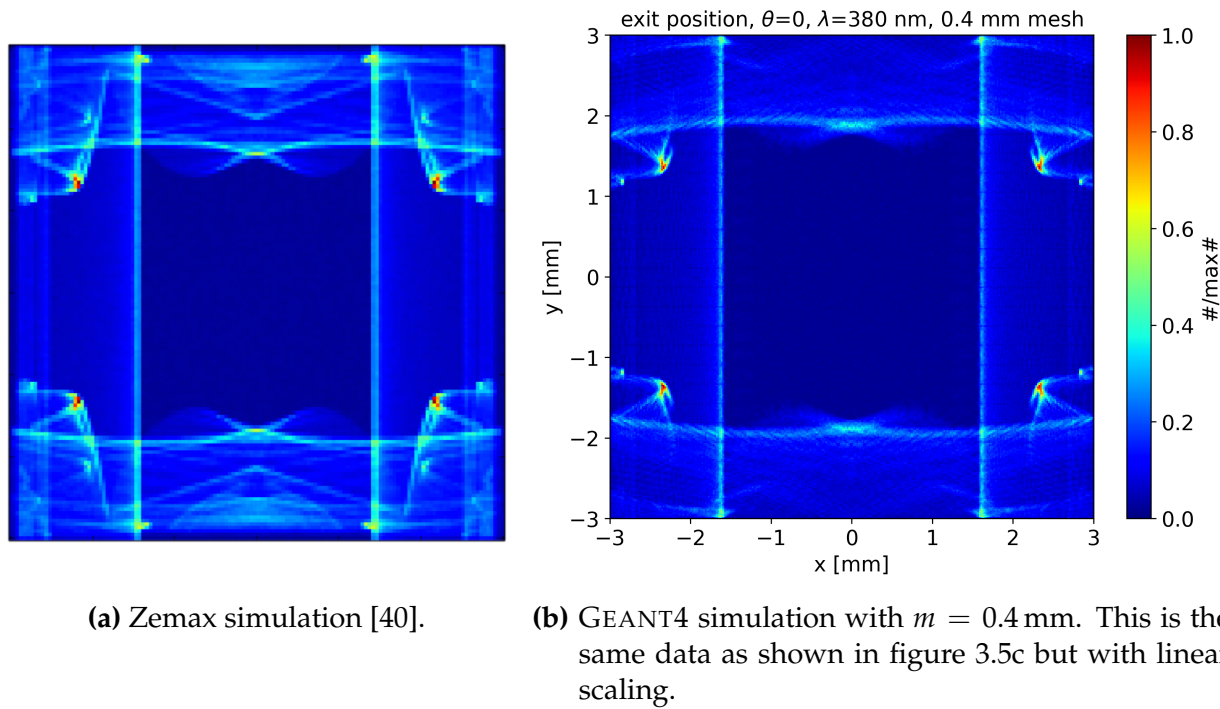


Figure 3.6.: Comparison between GEANT4 and Zemax simulation. For the main structure of the image by vertical illumination, GEANT4 produces a quite similar image to the Zemax simulation done in [40].

Additionally, one can quantify the complexity of the meshed model by looking at the file size for different mesh sizes. For the five investigated mesh sizes, this is done in table 3.1.

¹¹ Zemax is a commercial ray tracing tool for Microsoft Windows. It is commonly used for the analysis and optimization of optical systems.

mesh size m [mm]	size of meshed CAD file [KiB]	approx. loading time [s]
0.1	18 385	385
0.2	4581	23.8
0.4	2003	3.64
0.6	520	0.35
0.8	482	0.30

Table 3.1.: File size of Winston cone model for different mesh size. Additionally, the approximate loading time of one Winston cone is given (on a single CPU core at 1.4 GHz).

In summary, the mesh size $m = 0.4$ mm is chosen for the parameterization simulation since only slight artifacts are produced (cf. figure 3.5c). Additionally, it can reproduce the Zemax simulation quite well and with a file size of about 2 MiB, the loading time is at a just reasonable time scale of a few seconds.

3.1.4. The “Ghost Image” Effect

At all interfaces the photon has to pass, reflection and transmission occur. In the IceAct optics, mainly the transmission is desired. However, reflections occur as well. To get a rough estimate, one can assume perpendicular incidence and evaluate the transmission probability given in equation (2.2) with $n(\lambda) = 1.5$, $n_{\text{air}} = 1$. The result is that a photon is transmitted by $\approx 96\%$ and reflected by $\approx 4\%$. Usually, an incidental reflection results in diffuse scattering of the photons and reduces the imaging quality of the optical system. Besides this effect which results in a kind of “noisy” image, there is a very systematic beam path that ends up with an accumulation of scattered photons in a distinct direction – the *ghost image*. The reason for this effect is the glass plate in combination with the Fresnel lens. The imaging character of a lens translates an incident direction into a position on the focal plane. It is possible that a photon is reflected at the Winston cone entrance window and thus gets back to the Fresnel lens. The Fresnel lens can now refract the photon in such a way that it gets to the back of the glass plate – namely with the same inclination angle as in the initial state but now with the reversed traveling direction. A possible reflection on the glass plate results in a shift of the azimuth angle by 180° . By a transmission through the Fresnel lens once again, the photon is now refracted to the focal plane with an azimuth shift of 180° as well. If now this photon gets finally through the cone and is detected by the SiPM, it causes the ghost image. To visualize this, figure 3.7 shows the ghost image effect at “leading order” – i.e. the most probable beam path.

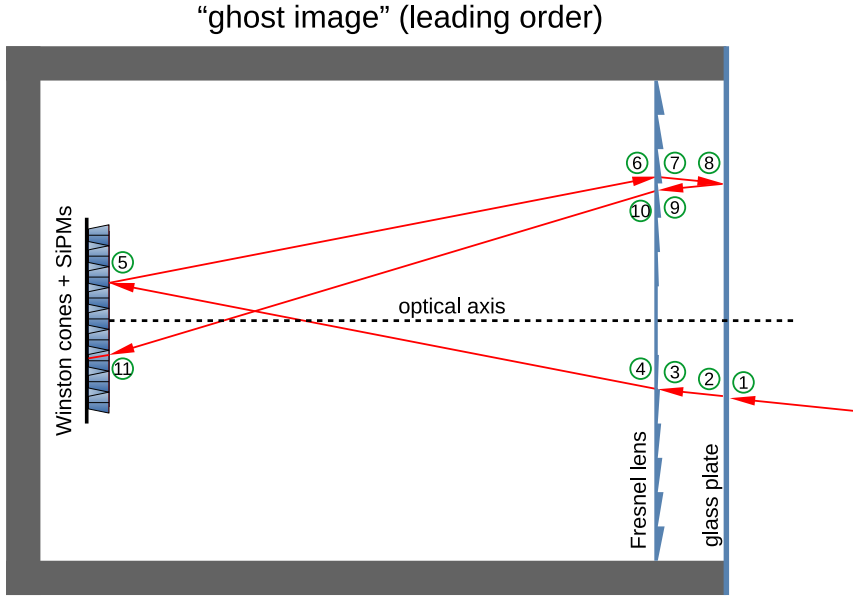


Figure 3.7.: Schematic sketch for the “ghost image” beam path. The encircled numbers mark the order of interface interactions. At 1, 2, 3, 4, 6, 7, 9, 10, and 11, transmission is required whereas at 5 and 8, the photon needs to be reflected in order to produce the ghost image. At 8, the azimuth shift of 180° takes place.

With the approximated transmission and reflection coefficient, one can estimate the suppression factor. The ghost image occurs if a photon undergoes two reflections and four transmissions more than a “normal” photon that is detected in the right SiPM. Thus, one gets a suppression factor of

$$(4\%)^2 \cdot (96\%)^4 \sim 0.1\%. \quad (3.3)$$

One obtains that the ghost image is a per-mill effect – i.e. for an image where 1000 photons are detected, one would expect one ghost image photon. The detection efficiency maps in figure 5.7 show some examples for the ghost image effect. It causes a suppressed mirror image of the core efficiency region. The ghost image is also visible in the camera top plane histograms of photons in figures 3.9, 3.10, and 3.11.

3.1.5. Impact-location-dependent Detection Efficiency

Due to their shape, the Winston cones have different maximum incident angles for their two symmetry axes (cf. figure 2.12). That implicates that there are trajectories with such angles that can not reach the exit window or the SiPM. For the optics, this leads to the fact that the detection efficiency may be dependent on the impact position on the lens or the glass plate, respectively. To investigate this, a ray tracing simulation is done where the lens is uniformly illuminated with photons of a single wavelength $\lambda = 420\text{ nm}$ and a single direction (θ, ϕ) . The resulting impact positions at the camera top plane and the camera pixel plane are histogramized. Additionally, all initial impact positions (x, y) at the glass plate are histogramized. By simulation, it is known which of the photons are detected. Therefore, one gets a impact-location-dependent detection efficiency profile – further abbreviated as *detection profile* – of the optics. The detection profiles have characteristic shapes for certain discrete photon directions. This is due to the symmetry properties of the IceAct camera. Basically, a hexagonal grid consisting of smaller hexagons has six symmetry axes but as the SiPMs are squared, these break down to only two remaining axes like it is sketched in figure 3.8.

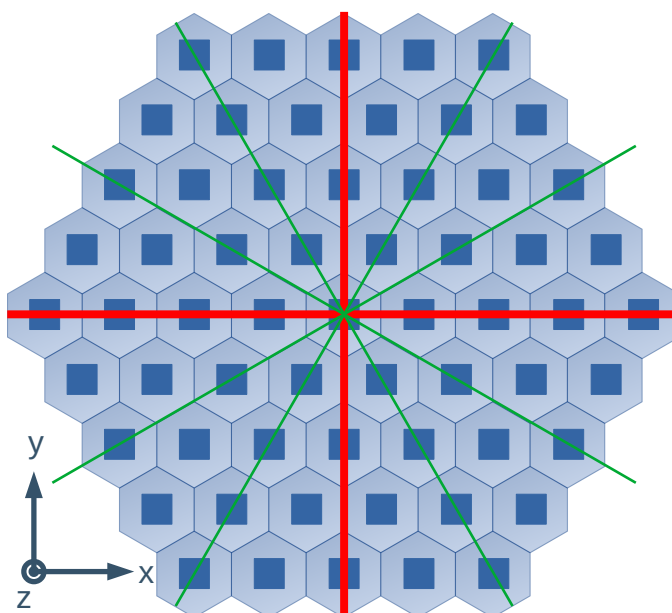
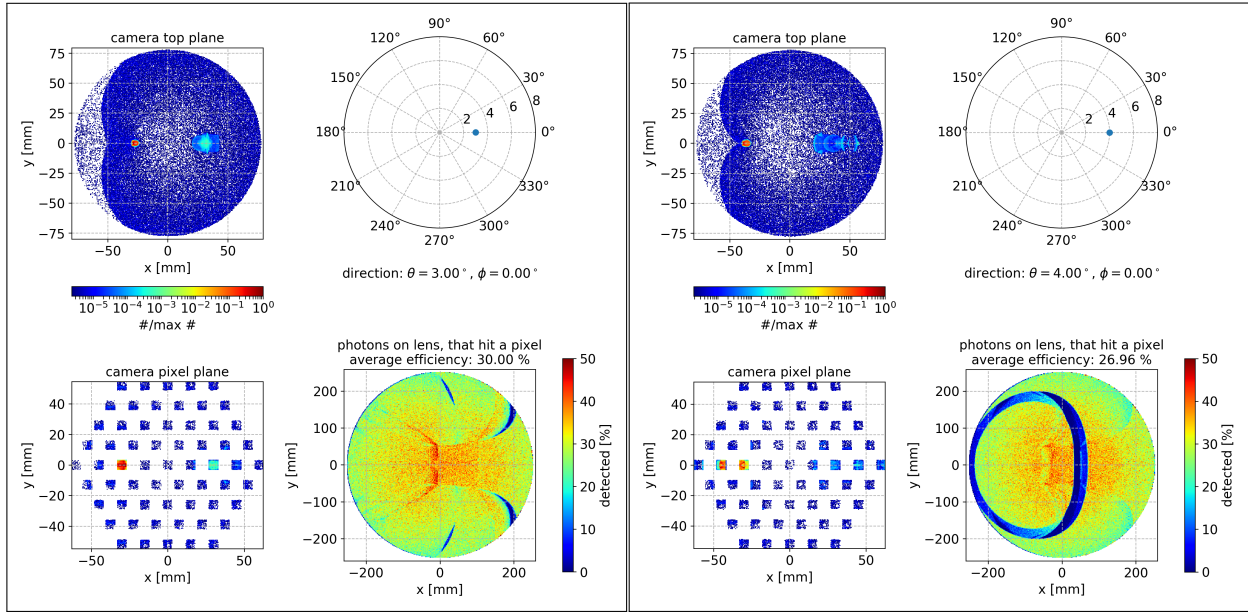


Figure 3.8.: Symmetry axes of the IceAct camera. The red lines show the two symmetry axes of the full camera. Additional symmetry axes of the hexagonal pattern are marked as green lines. The origin of the GEANT4 coordinate system sketched in the bottom left is the camera center on top of the Winston cones.

As a result, one expects the detection profiles for photon directions parallel to one of the

two symmetry axes to be symmetrical with respect to this axis as well. Figure 3.9 shows two examples.

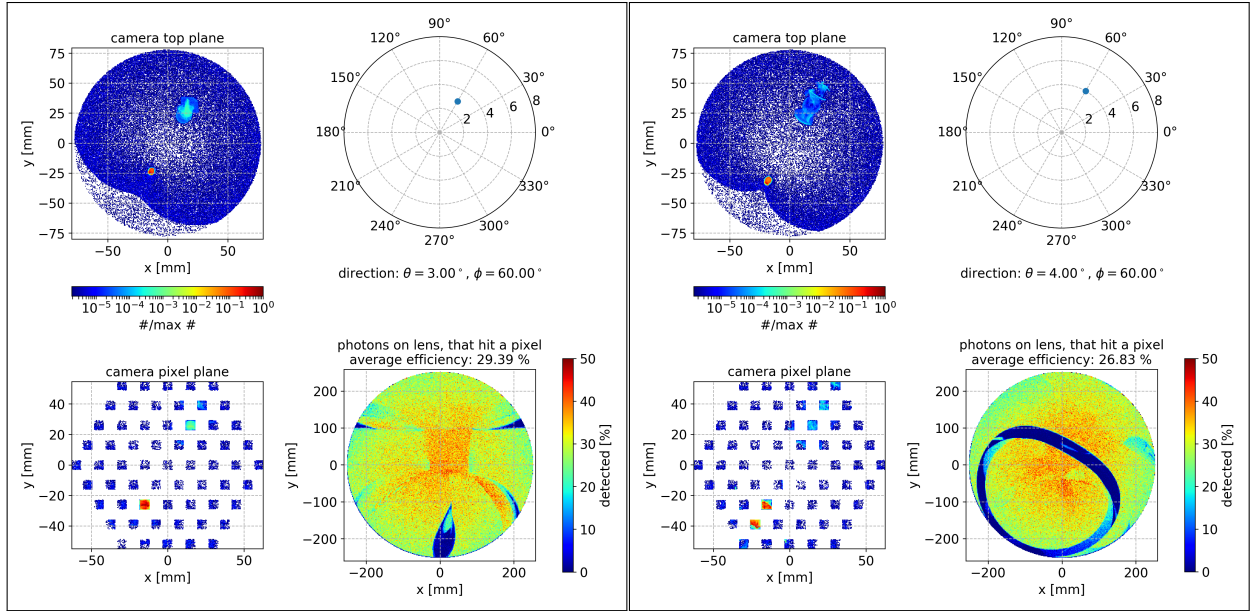


(a) Focal point on single Winston cone.

(b) Focal point on two Winston cones.

Figure 3.9.: Detection profiles in symmetry axis along x . The profile shown in the bottom right of each plot is distinct for both cases but since the photon direction is aligned to a symmetry axis of the whole camera, the detection profile is symmetrical w.r.t. this axis as well. Additional histograms of the photon distribution in the camera top plane (top left) and in the SiPM plane (bottom left) are shown. In the top right, the photon direction is plotted.

For the quasi-symmetrical axis – i.e. a symmetry axis of the hexagons but not of the SiPMs (green lines in figure 3.8) – one expects basically symmetrical detection profiles which are more or less distorted. Two examples are shown in figure 3.10.

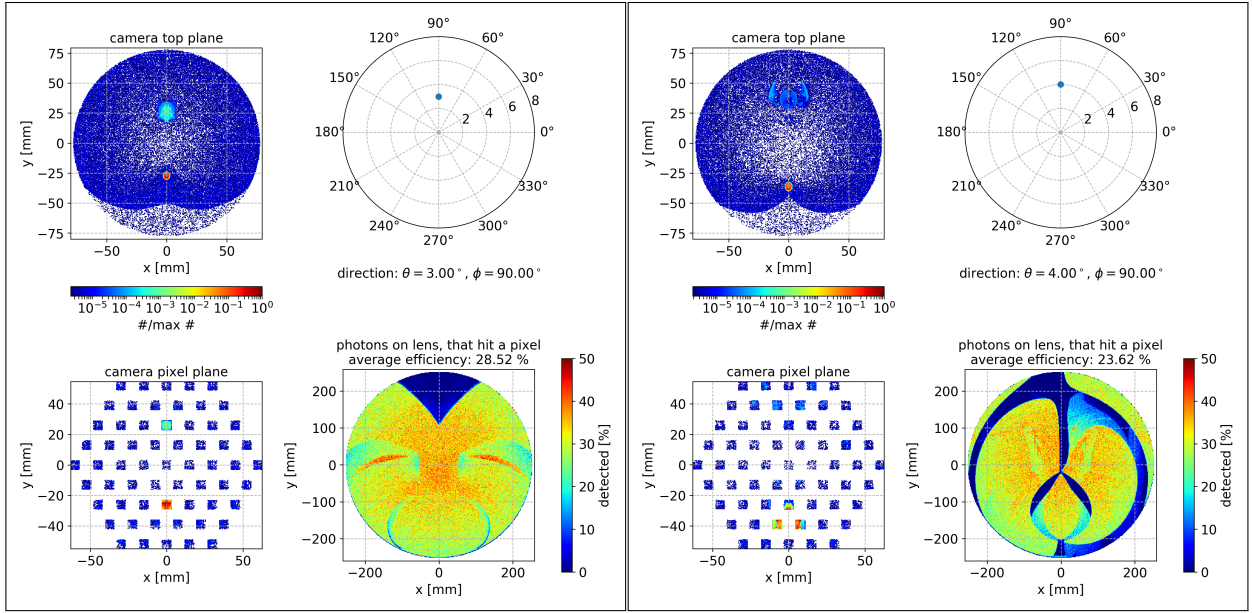


(a) Focal point on single Winston cone.

(b) Focal point on two Winston cones.

Figure 3.10.: Detection profiles in quasi-symmetry axis. Similar plots as in figure 3.9 but now for photon directions along a quasi-symmetrical axis. For the case of the focal spot being on a single Winston cone as in (a), the quasi-symmetrical detection profile is less obvious than for two Winston cones under the focal spot shown in (b).

Although the shape of detection profiles seems to be understood now, there is a peculiar behavior occurring if one simulated photon directions parallel to the other alleged main symmetry axis. If the focal spot is on top of just a single Winston cone, one obtains the expected symmetrical profile. However, if the focal spot covers multiple Winston cones – i.e. three along the y -axis – a significantly asymmetrical profile arises as shown in figure 3.11.



(a) Focal point on single Winston cone.

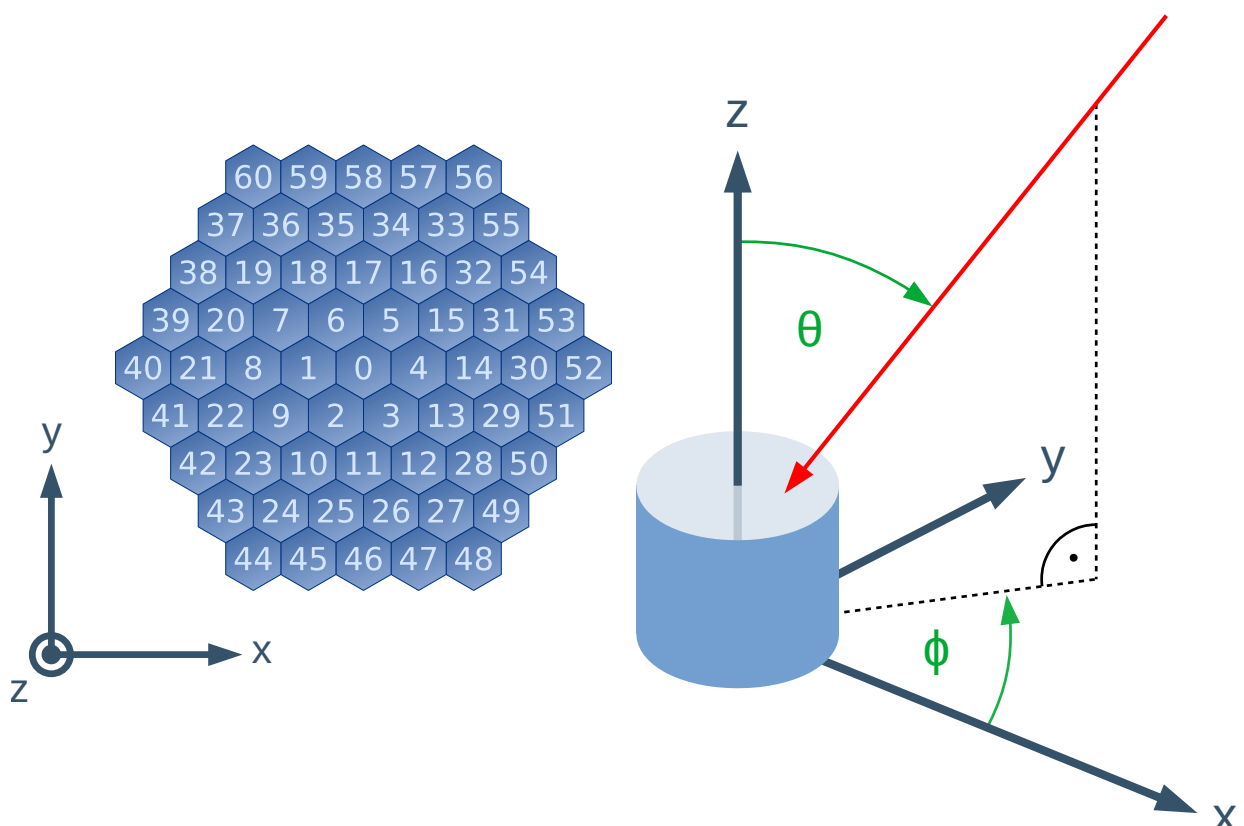
(b) Focal point on three Winston cones.

Figure 3.11.: Detection profiles in symmetry axis along y . Similar plots as in figure 3.9 but now for photon directions along the other symmetry axis of the whole camera. The symmetrical shape of the detection profile holds for the case of the focal spot under a single Winston cone shown in (a). However, the focal spot covering three Winston cones leads to considerable asymmetry of the profile.

Further investigation show that the strength of this feature is directly dependent on how strongly the focal spot covers multiple Winston cone entrance windows. More plots on this issue can be found in the appendix B.1. For the purpose of parameterizing the IceAct telescope, this feature is not that important since only the direction of the photons rather than their impact location on the telescope are considered. Therefore, it is sufficient for the parameterization to assume the detection profile to be constant and averaging their efficiency. Furthermore, the advantage is that the resulting parameterization is spatially independent. One only needs to know the orientation of the camera and a possible tilt angle of the optical axis.

3.2. Parameterization Simulation

The parameterization pursues the goal to yield the detection efficiency of each pixel for a photon with given wavelength λ and direction (θ, ϕ) . Therefore, a simulation has to be done for a wavelength range $[\lambda_{\min}, \lambda_{\max}]$ and a direction range – given by a maximum inclination angle θ_{\max} – in which IceAct is capable of detecting Cherenkov photons. Firstly, the GEANT4 coordinate system is introduced in figure 3.12.



(a) Top view of the IceAct camera with pixel numbering and coordinate system. The z -axis comes out of the drawing plane.

(b) Coordinate system for the IceAct telescope. The tube is sketched as a the blue cylinder. The coordinate origin is set as the center of the focal plane on the Winston cones' entrance windows. An exemplary incoming photon drawn as red line impinges on the glass plate under a zenith angle θ and an azimuth angle ϕ .

Figure 3.12.: Coordinate system used in GEANT4 and for the parameterization.

The wavelength range is mainly limited by the material properties and the photon detection efficiency of the SiPMs (cf. figures 2.4 and 2.19). The layout of the optical system determines the maximum inclination angle. In figure 2.5, a maximum inclination angle of $\approx 6.8^\circ$ is calculated. For this parameterization, a larger angle of $\theta_{\max} = 10^\circ$ is chosen in order to account for UV photons near λ_{\min} which are refracted more strongly and thus can be detected under higher zenith angles. Both – i.e. wavelengths and directions – are simulated uniformly distributed. For λ and ϕ this can be done without problems. For the zenith angle θ one has to consider the curvilinear character of the spherical coordinate system which causes a variable phase space depending on θ . By taking the cosine of the zenith angle, this effect is compensated. Thus, the simulation is done uniformly in $\cos \theta$. Additionally, the focal plane shift (cf. section 3.1.2) and the reasonable mesh size (cf. section 3.1.3) is applied. In total, $15 \cdot 10^9$ particles are simulated. As already stated in section 3.1.5, the detection efficiency should be determined independently of the impact position of a single Cherenkov photon on the telescope. This is ensured by seeding the simulated particles uniformly distributed directly above the glass plate and thus fully illuminate it. Although an additional calculation of the effective area can thus be dropped, one has to define to which aperture the detection probabilities should be normalized. Since the glass plate has a larger diameter than the lens as it covers the tube's coating, a normalization to an accidentally false aperture would result in different probabilities. In this simulation, the aperture of the telescope is assumed to be the area of the glass plate, thus $A_{\text{eff}} = \pi(650.3 \text{ mm})^2 \approx 1.33 \text{ m}^2$. Table 3.2 gives a summary of the simulation parameters.

description	symbol	value
minimum simulated wavelength	λ_{\min}	272 nm
maximum simulated wavelength	λ_{\max}	900 nm
maximum simulated zenith angle	θ_{\max}	10°
mesh size (maximum edge length)	m	0.4 mm
focal plan shift	Δz	1.25 mm
total simulated particles	N_{sim}	$15 \cdot 10^9$
effective area	A_{eff}	1.33 m^2

Table 3.2.: Parameters chosen for the parameterization simulation. Wavelengths are simulated uniformly in the interval $[\lambda_{\min}, \lambda_{\max}]$. The direction are simulated uniformly in azimuth ϕ and cosine of the zenith angle $\cos \theta$. The reasonable mesh size determined in section 3.1.3 and the focal plane shift discussed in section 3.1.2 are applied.

CHAPTER 4.

IceAct Parameterization Strategy

The simulation results discussed in chapter 3 can now be used to parameterize the telescope response of IceAct. The major goal of this is to provide a fast way to evaluate the detection probability of incident photons in each camera pixel which is done by elaboration of a lookup table (*LUT*). Afterwards, the high computational effort by propagating each Cherenkov photon through the whole GEANT4 model is not needed anymore. To achieve this, one needs a well-defined strategy to convert the simulated raw data into a meaningful parameterization.

The following chapter will discuss the step-by-step strategy to get *detection efficiency maps* out of the GEANT4 data. These maps will describe the direction-dependent detection probability for a certain wavelength range and a certain camera pixel.

As a first step, one needs to derive probability statements from raw data consisting of direction distributions of detected photons. Since there is no model or function as a template, an approach is needed in which a model is deduced directly from the data sample. This is known as a *non-parametric* probability density estimation method. Specifically, for the IceAct parameterization the approach of kernel density estimation is used.

4.1. Kernel Density Estimation (KDE)

Kernel density estimation (KDE) is a non-parametric method to estimate a *probability density function (PDF)* of a random variable by a given finite data sample. The standard *kernel density estimator*

$$\hat{f}(x) = \frac{1}{nh} \sum_{i=1}^n K\left(\frac{x - X_i}{h}\right) \quad (4.1)$$

is the sum of *kernel functions* $K(\dots)$ for each data point X_i . The non-negative parameter h is the *bandwidth* and is a measure for the smoothing of the resulting KDE: the KDE gets smoother with increasing h . Due to the normalization factor, $\hat{f}(x)$ is normed to

$$\int_{-\infty}^{+\infty} \hat{f}(x) dx \equiv 1. \quad (4.2)$$

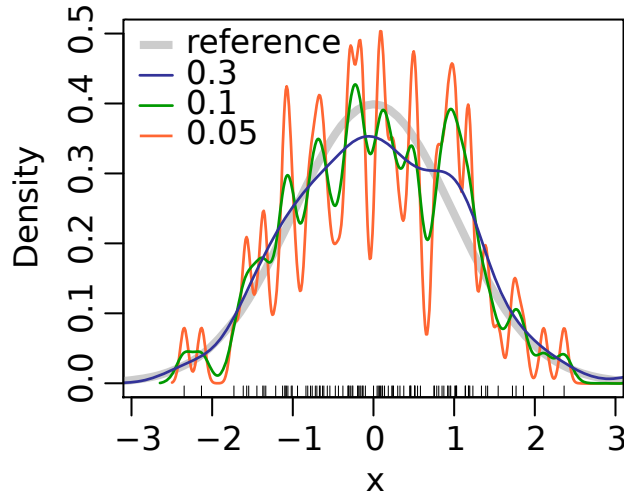


Figure 4.1.: Example KDE with different smoothing. [53] The kernel density estimation method is applied on a data sample with 100 random numbers drawn from a normal distribution (gray curve). The blue, green, and orange curves have different bandwidths.

The kernel function can be a very distinct function that can in principle describe any probability density. In this parameterization method, a Gaussian kernel

$$K(t) = \frac{1}{\sqrt{2\pi}} e^{-\frac{1}{2}t^2} \quad (4.3)$$

is used.

In order to make the KDE describing the probability density appropriately, one has to choose a reasonable bandwidth for the given data sample size. As shown in figure 4.1, too low bandwidth results in a spiky, fluctuating KDE. If the bandwidth is too high, one might get a rather inaccurate estimator. Therefore, it seems reasonable to choose different bandwidth in regions with different amount of statistics which then is called *adaptive* kernel density estimation. [54, 55]

4.1.1. Adaptive KDE with Gaussian Kernel

On the IceAct camera, each pixel has a certain region of photon directions where it is efficient. However, each pixel is almost “blind” for most other directions. This results in statistically stable – “dense” – regions but also “sparse” regions dominated by scattered photons that undergo large statistical fluctuations. Thus and based on the former conclusions, an approach to adapt the bandwidth to the local statistics should perform well. In this thesis, an algorithm presented by B. WANG and X. WANG in [55] which has been implemented within the scope of [54] is used. The adaptive (in principle weighted) kernel density estimator is calculated by [54, 55]

$$f(\vec{x}) = \sum_{i=1}^n \frac{w_i}{N_i} e^{-\frac{1}{2}(\vec{x}-\vec{X}_i)^T \frac{1}{h\lambda_i} \mathbf{C}^{-1}(\vec{x}-\vec{X}_i)}, \quad (4.4)$$

with

- n total number of data points,
- w_i weight of the i -th data point,
- N_i Gaussian normalization,
- \vec{X}_i coordinate vector of the i -th data point,
- h global bandwidth factor,
- λ_i local bandwidth factor,
- \mathbf{C} covariance matrix.

The global bandwidth factor h is calculated by the *Silverman rule* [54, 55]

$$h = \left(\frac{n(d+2)}{4} \right)^{-\frac{1}{d+4}}, \quad (4.5)$$

where d equals the number of dimensions of the data (here $d = 2$).

The local bandwidth λ_i is the factor where the local statistics of each data point is included. It is defined as [54, 55]

$$\lambda_i = \left(\frac{\hat{f}(\vec{X}_i)}{g} \right)^{-\alpha}, \quad (4.6)$$

with

$$\begin{aligned}\hat{f}(\vec{X}_i) &= f(\vec{X}_i)|_{w_i=\lambda_i=1}, \\ \ln g &= n^{-1} \sum_{i=1}^n \ln \hat{f}(\vec{X}_i), \\ \alpha &\in [0, 1].\end{aligned}$$

For the IceAct parameterization, the sensitivity parameter α is set to $\alpha = 0.3$ since this has been shown to be an appropriate value as well as in [54]. Additionally, all n photon hits have the same weight which results in [54, 55]

$$w_i = \frac{1}{n}. \quad (4.7)$$

4.1.2. Bootstrapping

One problem of kernel density estimation is that it does not provide any statistical information – i.e. “how precisely” the probability density is estimated. Since the data set used for the KDE is just a random sample of the underlying *probability density function (PDF)*, one needs a method to draw multiple sub-samples from the given data which is known as *resampling*. More specifically, the *bootstrapping* method is used. It is a type of resampling where n data points are drawn from n data points with replacement, so that one data point can possibly be chosen multiple times or not at all. The probability of drawing a point is equal for all points given by $\frac{1}{n}$. Hence, the probability of not drawing a single data point in a bootstrapped sample is

$$\left(1 - \frac{1}{n}\right)^n \xrightarrow{n \rightarrow \infty} \approx 37\%. \quad (4.8)$$

For a large sample size $n \rightarrow \infty$, this means that $1 - \left(1 - \frac{1}{n}\right)^n \approx 63\%$ of the data points in a bootstrapped data sample are statistically independent.

The bootstrapping can now be repeated k times and for each sub-sample $\{\vec{X}_i^*\}$, an adaptive KDE is done resulting in k KDE functions $f_{\{\vec{X}_i^*\}}(\vec{x})$. The final KDE function $f(\vec{x})$ and its statistical uncertainty is then given by the mean and the standard deviation, [54, 56]

$$f(\vec{x}) = \frac{1}{k} \sum_{i=1}^k f_{\{\vec{X}_i^*\}}(\vec{x}) \quad (4.9a)$$

$$\sigma_{f(\vec{x})} = \sqrt{\frac{1}{k} \sum_{i=1}^k \left(f_{\{\vec{X}_i^*\}}(\vec{x}) - f(\vec{x}) \right)^2} \quad (4.9b)$$

4.2. Coordinate Transformation for KDE

The kernel density estimation method needs a well-defined coordinate system on which the data is represented. The problem with a polar coordinate system (θ, ϕ) is the singularity at the zenith $\theta = 0^\circ$. At this point, there is no defined azimuth value ϕ . In order to get a “flat” and well-defined coordinate system, one introduces the coordinates

$$\begin{pmatrix} u \\ v \end{pmatrix} = \begin{pmatrix} \sin \theta \cos \phi \\ \sin \theta \sin \phi \end{pmatrix}. \quad (4.10)$$

This leads to a projection of a sphere onto a flat coordinate space with $u \in [-1, 1]$ and $v \in [-1, 1]$ without any singularities. The direction coordinates (θ, ϕ) of detected photons are transformed into uv space in which the KDE is calculated as well. Thus, the KDE has to be evaluated in uv space. Subsequently, the back transformation to spherical coordinates can be performed by

$$\begin{pmatrix} \theta \\ \phi \end{pmatrix} = \begin{pmatrix} \arcsin \sqrt{u^2 + v^2} \\ \pi + \text{arctan2}(v, u) \end{pmatrix}. \quad (4.11)$$

Here, $\text{arctan2}(v, u)$ is an extension of the arctangent function to be defined in all four quadrants of a two-dimensional Cartesian coordinate system. Descriptively, the result of $\text{arctan2}(v, u)$ is the angle between the positive x -axis and the position vector of the point $(u|v)$ yielding angles between 0 and 2π (0° and 360° , respectively). Therefore, it is convenient to be used in the transformation from Cartesian into polar coordinates.

Concretely, the arctan2 is defined by

$$\arctan2(v, u) = \begin{cases} \arctan \frac{v}{u} & u > 0 \\ \arctan \frac{v}{u} + \pi & u < 0, v \geq 0 \\ \arctan \frac{v}{z} - \pi & u < 0, v < 0 \\ +\frac{\pi}{2} & u = 0, v > 0 \\ -\frac{\pi}{2} & u = 0, v < 0 \\ \text{undefined} & u = 0, v = 0 \end{cases}. \quad (4.12)$$

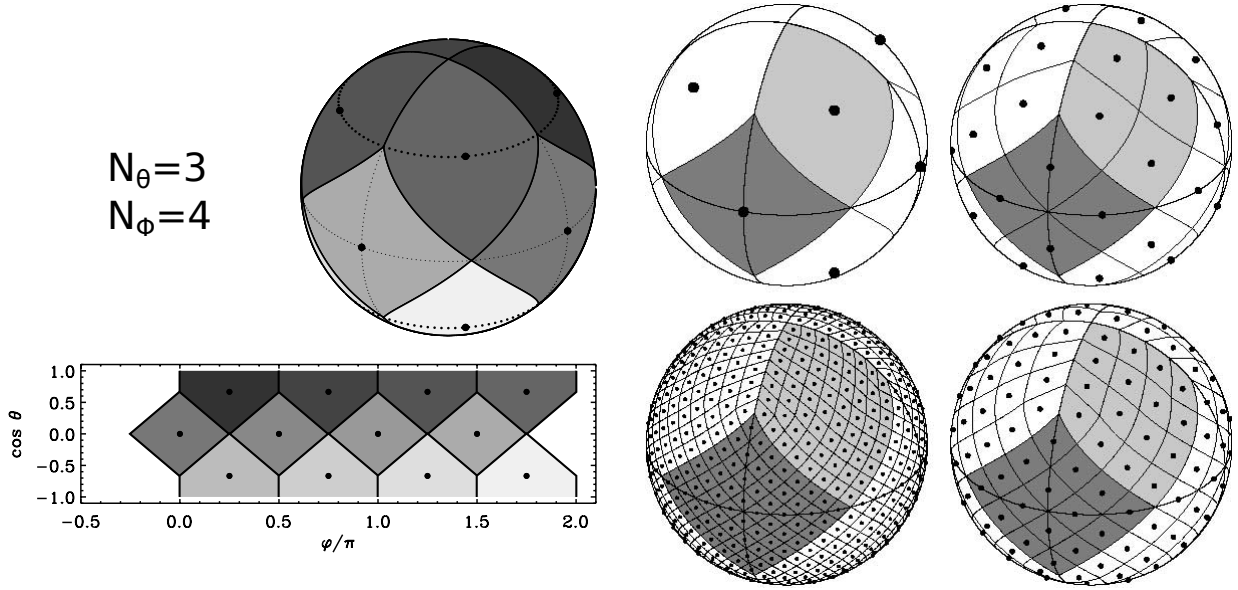
4.3. KDE Evaluation

Thanks to the former considerations, a proper evaluation of the estimated PDFs is now possible. Next, a reasonable method has to be found which means that one has to think about on which “grid” to evaluate the calculated probability densities and how to translate them into actual detection efficiency statements.

4.3.1. The HEALPix Algorithm

In order to account for the spherical shape of the angles of incidence, it is useful to have angular bins with equal areas. Therefore – in this parameterization method – the *HEALPix*¹² algorithm is used. It allows a uniform pixelization of incidence angles to the telescope.

¹² Hierarchical Equal Area isoLatitude Pixelization



(a) Orthographic (top) and cylindrical (bottom) view of the pixelization scheme at the initial step ($k = 0$). The sphere is tessellated into 12 quadrilateral equal-area panes with $N_\theta = 3$ divisions in zenith and $N_\phi = 4$ divisions in azimuth angle.

(b) Further subdivision steps starting with the initial base resolution $k = 0$ (top left) and $k = 1, 2, 3$ clockwise. The light gray shaded area marks one of the 8 identical polar base-resolution pixels while the dark light shaded area marks one of the 4 identical equatorial base-resolution pixels.

Figure 4.2.: Pixelization scheme of the HEALPix algorithm. [57, adapted]

The basic idea is to subdivide the sphere into 12 quadrilateral equal-area panes which can then further be divided uniformly into more sub panes as shown in figure 4.2. A parameter k numbers the subdivision step starting with the base resolution at $k = 0$ so that the number of sub panes per each of the 12 panes is $N_{\text{side}}^2 = (2^k)^2$. Hence, the total amount of pixels on the sphere is then [57]

$$N_{\text{pix}} = 12N_{\text{side}}^2. \quad (4.13)$$

The angular resolution θ_{pix} is defined to be the square root of the angular area Ω_{pix} , thus the angular length of a pixel edge. Ω_{pix} in turn can be calculated by dividing the total angular area of a sphere 4π by the total number of pixels N_{pix} which yields [57]

$$\theta_{\text{pix}} = \sqrt{\Omega_{\text{pix}}} = \sqrt{\frac{4\pi}{N_{\text{pix}}}} \stackrel{(4.13)}{=} \sqrt{\frac{4\pi}{12N_{\text{side}}^2}} = \sqrt{\frac{\pi}{3}} N_{\text{side}}^{-1} [\text{rad}]. \quad (4.14)$$

Table 4.1 gives an overview of pixel amounts and angular pixel area for the first subdivision steps.

k	$N_{\text{side}} = 2^k$	$N_{\text{pix}} = 12N_{\text{side}}^2$	$\theta_{\text{pix}} = \sqrt{\Omega_{\text{pix}}}$
0	1	12	58.6°
1	2	48	29.3°
2	4	192	14.7°
3	8	768	7.33°
4	16	3072	3.66°
5	32	12 288	1.83°
6	64	49 152	55.0'
7	128	196 608	27.5'
8	256	786 432	13.7'
9	512	3 145 728	6.87'
10	1024	12 582 912	3.44'
11	2048	50 331 648	1.72'
12	4096	201 326 592	51.5''
13	8192	805 306 368	25.8''
:	:	:	:

Table 4.1.: HEALPix parameters and resulting angular resolutions. [57] k represents the number of dividing iterations on the 12 panes, N_{side} the number of tiles per pane edge, N_{pix} the total number of pixels, and θ_{pix} the angular resolution defined by the angular length of a pixel edge.

For the application in this simulation, the pixelization of a whole sphere is not needed since the telescope only has a field of view of about 12° (i.e. $\theta \leq 6^\circ$). Considering that, one only needs a smaller sector of pixels around the zenith at $\theta = 0^\circ$ which reduces the number of needed HEALPix to a factor of

$$\Gamma = \frac{1}{4\pi} \int_0^{2\pi} \int_0^{\theta_{\text{max}}} \sin \theta d\theta d\phi = \frac{1 - \cos \theta_{\text{max}}}{2}. \quad (4.15)$$

For the IceAct simulation with $\theta_{\text{max}} = 10^\circ$, this leads to the fact that only about 0.76 % of the sphere is needed to be pixelized¹³.

An additional important supplement is that the HEALPix numbering scheme is hierarchical. The standard numbering scheme – called *ring scheme* – starts at the zenith $\theta = 0^\circ$ and follows a spiral for increasing zenith angles. There are two advantages of this numbering scheme for the use case of IceAct simulation. On the one hand, the unambiguous

¹³ In the IceAct parameterization, a few more HEALPix are actually needed. The reason is that all HEALPixels that at least overlap partly with the region $\theta \leq \theta_{\text{max}}$ are included.

numbering makes it unnecessary for the directional coordinates (θ, ϕ) to be saved but only the ordinal number HP . In order to reconstruct the direction in polar coordinates, one only has to know the pixelization parameter N_{side} . On the other hand, the ring scheme and the fact that the simulated directions are limited by θ_{\max} result in a distinct maximum ordinal number HP^{\max} and one can just ignore all pixels beyond this number. This allows saving information very efficiently by using HEALPixes.

4.3.2. KDE Renormalization: Detection Efficiency

By using the adaptive KDE method, one gets a probability density function which implies normalization (cf. equation (4.2)). In order to get to an actual efficiency, one has to do a renormalization.

The ansatz is made by describing the differential detection efficiency of the i -th SiPM in the angular area $d\Omega$ as a ratio of *detection density* in the i -th SiPM $\rho_{\text{det},i,\Delta\lambda}(\theta, \phi)$ and *simulation density* $\rho_{\text{sim},\Delta\lambda}(\theta, \phi)$ for each wavelength range $\Delta\lambda$ by

$$\frac{d\epsilon_{i,\Delta\lambda}}{d\Omega}(\theta, \phi) = \frac{1}{d\Omega} \frac{\rho_{\text{det},i,\Delta\lambda}(\theta, \phi)}{\rho_{\text{sim},\Delta\lambda}(\theta, \phi)}, \quad (4.16)$$

Hereafter, the densities are derived by asking following questions.

How many photons are detected in SiPM i and wavelength range $\Delta\lambda$?

Follows directly from the amount of data points used for KDE. $\rightarrow N_{\text{det},i,\Delta\lambda}$

How many photons are simulated in the wavelength range $\Delta\lambda$?

Obviously needed to make a statement on the ratio of detected photons. $\rightarrow N_{\text{sim},\Delta\lambda}$

The ratio of detected and simulated photons in the i -th SiPM and the wavelength range $\Delta\lambda$ can then be defined as the average detection efficiency

$$\bar{\epsilon}_{i,\Delta\lambda} = \frac{N_{\text{det},i,\Delta\lambda}}{N_{\text{sim},\Delta\lambda}}. \quad (4.17)$$

What is the maximum simulated zenith angle?

Needed to calculate the ratio Γ of the total spherical area that is evaluated (cf. equation (4.15)). For the IceAct simulation, this is $\theta_{\max} = 10^\circ$. $\rightarrow \theta_{\max}$

What size does the angular area have which the KDE is evaluated for?

This is caused by the evaluation of a continuous PDF at discrete points. To do so, one has to consider the angular area Ω_{HP} for which a discrete value is set to be constant.

Thanks to the use of HEALPixes, the angular area of all pixels is constant and follows from the resolution parameter N_{side} by

$$\Omega_{\text{HP}} = \frac{4\pi}{N_{\text{pix}}} \stackrel{(4.13)}{=} \frac{\pi}{3N_{\text{side}}^2}. \quad (4.18)$$

From the former considerations, one can conclude the densities given by

$$\rho_{\text{det},i,\Delta\lambda}(\theta, \phi) = \begin{cases} N_{\text{det},i,\Delta\lambda} \cdot \text{KDE}_{i,\Delta\lambda}(\theta, \phi) & \theta \leq \theta_{\max} \\ 0 & \theta > \theta_{\max} \end{cases}, \quad (4.19a)$$

$$\rho_{\text{sim},\Delta\lambda}(\theta, \phi) = \begin{cases} \frac{N_{\text{sim},\Delta\lambda}}{4\pi\Gamma} & \theta \leq \theta_{\max} \\ 0 & \theta > \theta_{\max} \end{cases}. \quad (4.19b)$$

In equation (4.19a), $N_{\text{det},i,\Delta\lambda}$ rescales the KDE to be normed to the total amount of detected photons. The factor $(4\pi\Gamma)^{-1}$ in equation (4.19b) takes account of the zenith angle limit in the simulation so that the densities have the unit

$$[\rho] = \frac{\text{particles}}{\text{angular area}}. \quad (4.20)$$

Additionally, one can exploit the equal area properties of the HEALPixes by evaluating the detection efficiency at the central points of each HEALPix $(\theta_{\text{HP}}^*, \phi_{\text{HP}}^*)$ and setting this value to be a constant in each HEALPix area. Hence, we can calculate the detection efficiency by

$$\begin{aligned} \epsilon_{i,\Delta\lambda,\text{HP}}(\theta \leq \theta_{\max}) &= \iint_{\Omega_{\text{HP}}} \frac{d\epsilon_{i,\Delta\lambda}}{d\Omega}(\theta_{\text{HP}}^*, \phi_{\text{HP}}^*) d\Omega \\ &= \iint_{\Omega_{\text{HP}}} \frac{1}{d\Omega} \frac{N_{\text{det},i,\Delta\lambda}(\theta_{\text{HP}}^*, \phi_{\text{HP}}^*)}{N_{\text{sim},\Delta\lambda}} \cdot 4\pi\Gamma \cdot \text{KDE}_{i,\Delta\lambda}(\theta_{\text{HP}}^*, \phi_{\text{HP}}^*) d\Omega \\ &= \frac{N_{\text{det},i,\Delta\lambda,\text{HP}}}{N_{\text{sim},\Delta\lambda}} \cdot 4\pi\Gamma \cdot \text{KDE}_{i,\Delta\lambda,\text{HP}} \\ &\stackrel{(4.15)}{=} \frac{N_{\text{det},i,\Delta\lambda,\text{HP}}}{N_{\text{sim},\Delta\lambda}} \cdot 2\pi(1 - \cos \theta_{\max}) \cdot \text{KDE}_{i,\Delta\lambda,\text{HP}}, \end{aligned} \quad (4.21)$$

with $N_{\text{det},i,\Delta\lambda,\text{HP}} := N_{\text{det},i,\Delta\lambda}(\theta_{\text{HP}}^*, \phi_{\text{HP}}^*)$ and $\text{KDE}_{i,\Delta\lambda,\text{HP}} := \text{KDE}_{i,\Delta\lambda}(\theta_{\text{HP}}^*, \phi_{\text{HP}}^*)$. This yields a detection efficiency value for each SiPM i , wavelength range $\Delta\lambda$, and HEALPix HP .

To visualize the renormalization process, figure 4.3 shows a 1D example.

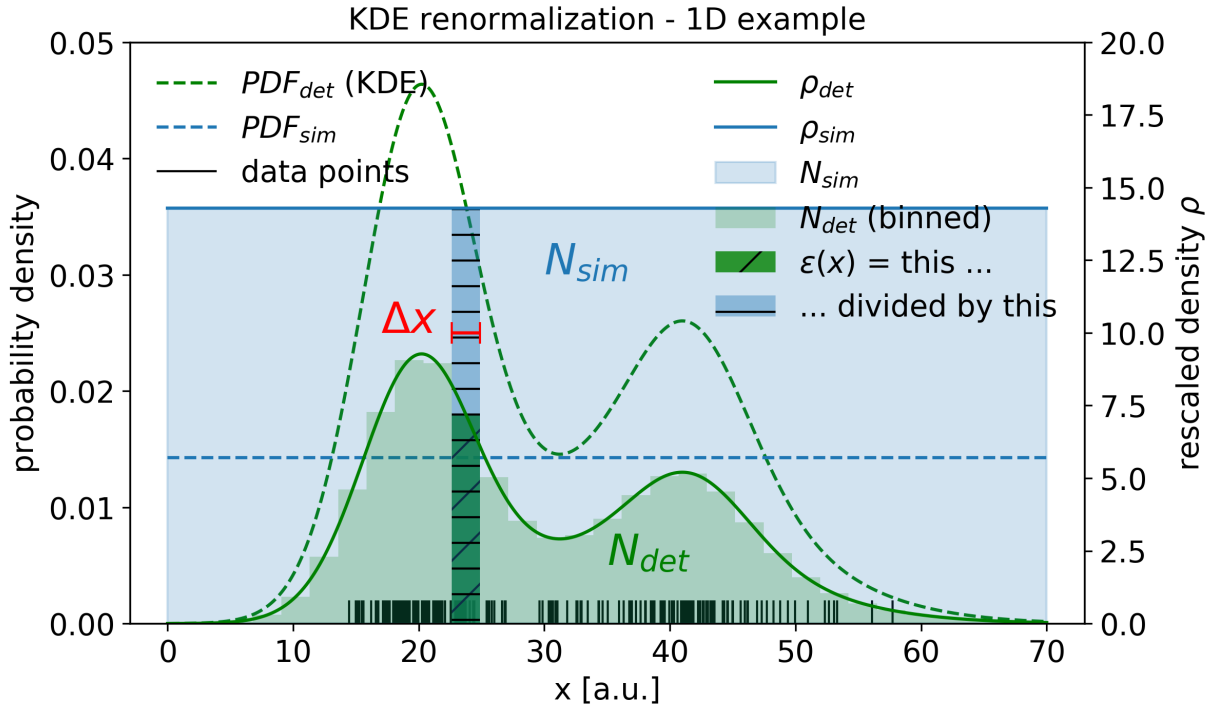


Figure 4.3.: Example: KDE renormalization. 1D example to visualize the renormalization process. In this “toy simulation”, 1000 “photons” are simulated uniformly in the interval [0 a.u., 70 a.u.] for which the blue dashed line is the corresponding PDF. 200 “photons” are detected (black dashes on the x -axis) and the PDF is calculated by adaptive kernel density estimation (green dashed line). Since the PDFs are both normalized to 1 (w.r.t. left y -axis), a rescaling is now done (cf. right y -axis). The KDE for detected “photons” is scaled (green solid line) so that the enclosed area is $N_{\text{det}} = 200$. This is also done with the PDF of simulated data (blue solid line) in order to correspond to an enclosed area $N_{\text{sim}} = 1000$. The scaled detection and simulation densities ρ_{det} and ρ_{sim} are evaluated in bins with size Δx which is analogous to the HEALPix area Ω_{HP} (cf. equation (4.18)). One gets the detection efficiency $\epsilon(x)$ for each bin by dividing the emphasized hatched areas by each other. The division of areas incorporates the integration over the HEALPix area done in the “real” evaluation (cf. equation (4.21)).

CHAPTER 5.

Application on Simulated Data

The parameterization strategy introduced in chapter 4 can now be applied to the simulation results from GEANT4. In the following sections, some comparisons and results are shown and discussed.

5.1. Wavelength Binning

Since the photon detection efficiency of the SiPMs is a non-constant function of the wavelength (cf. figure 2.19), one can optimize the different wavelength ranges or *bin sizes* $\Delta\lambda$ by equalizing not the bin sizes themselves (*constant binning*) but the detected photons per bin which is further referred to as *adaptive binning*. Figure 5.1 shows a comparison between constant and adaptive wavelength binning.

The adaptive bin edges are calculated by sorting the wavelengths of all simulated particles that are detected by any of the 61 SiPMs – i.e. all photons on which the KDE will be applied afterwards (cf. section 5.2). Next, this sequence is divided into 50 parts of equal length. Thus, the wavelengths are divided into consecutive 2 %-quantiles. In order to get more convenient bin sizes, the quantile limits (or bin edges) are rounded to integer values which obviously result in some fluctuations (cf. figure 5.1b).

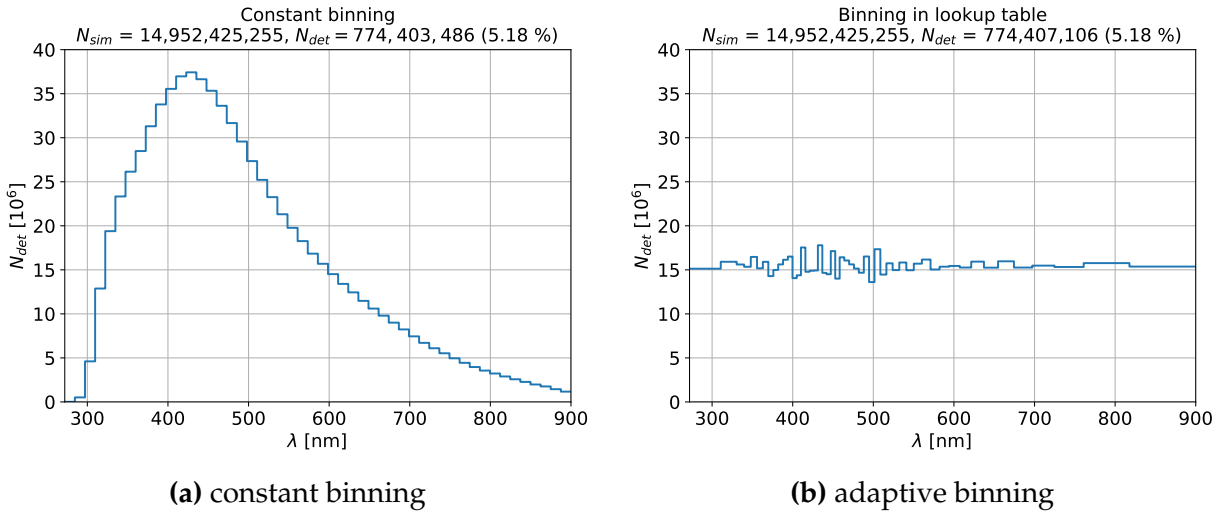


Figure 5.1.: Constant vs. adaptive wavelength binning. All wavelengths of photons that are detected by any camera SiPM are histogrammed in 50 bins between 272 nm and 900 nm. In (a), the 50 bins are distributed uniformly in wavelength so that one can see a shape that is quite similar to the PDE of the SiPMs. Figure (b) shows the same data with adaptive bin sizes to equalize the counts per bin. The resulting bin edges are rounded to integer numbers which causes the visible fluctuations. Since the adaptive bin limits are always included by closed intervals, there are slightly more detected photons in (b) than in (a) due to numerical issues. This is not a problem since also the simulated photons are binned in the same closed intervals which result in correct detection efficiency calculations.

With the adaptive wavelength binning, it is ensured that in each range $\Delta\lambda$ almost the same number of photons is detected which enables a statistically more stable probability density estimation. The simulated wavelength range starts at $\lambda_{\min} = 272$ nm since there is no photon detected with a wavelength below 272 nm due to the absorption properties of the glass plate (cf. 2.2).

5.2. Adaptive vs. Non-adaptive KDE

Now that the wavelength binning is defined, the next step is to take a look on the camera pixels individually. Due to the distinct field of view of each pixel, the direction distribution of each pixel is characteristic and has regions with very different statistical densities as already stated in section 4.1.1. In order to get an idea of the given direction distributions for which the KDE should be calculated, figure 5.2 shows some exemplary scatter plots of detected photons by an arbitrary camera pixel i in a wavelength range $\Delta\lambda$.

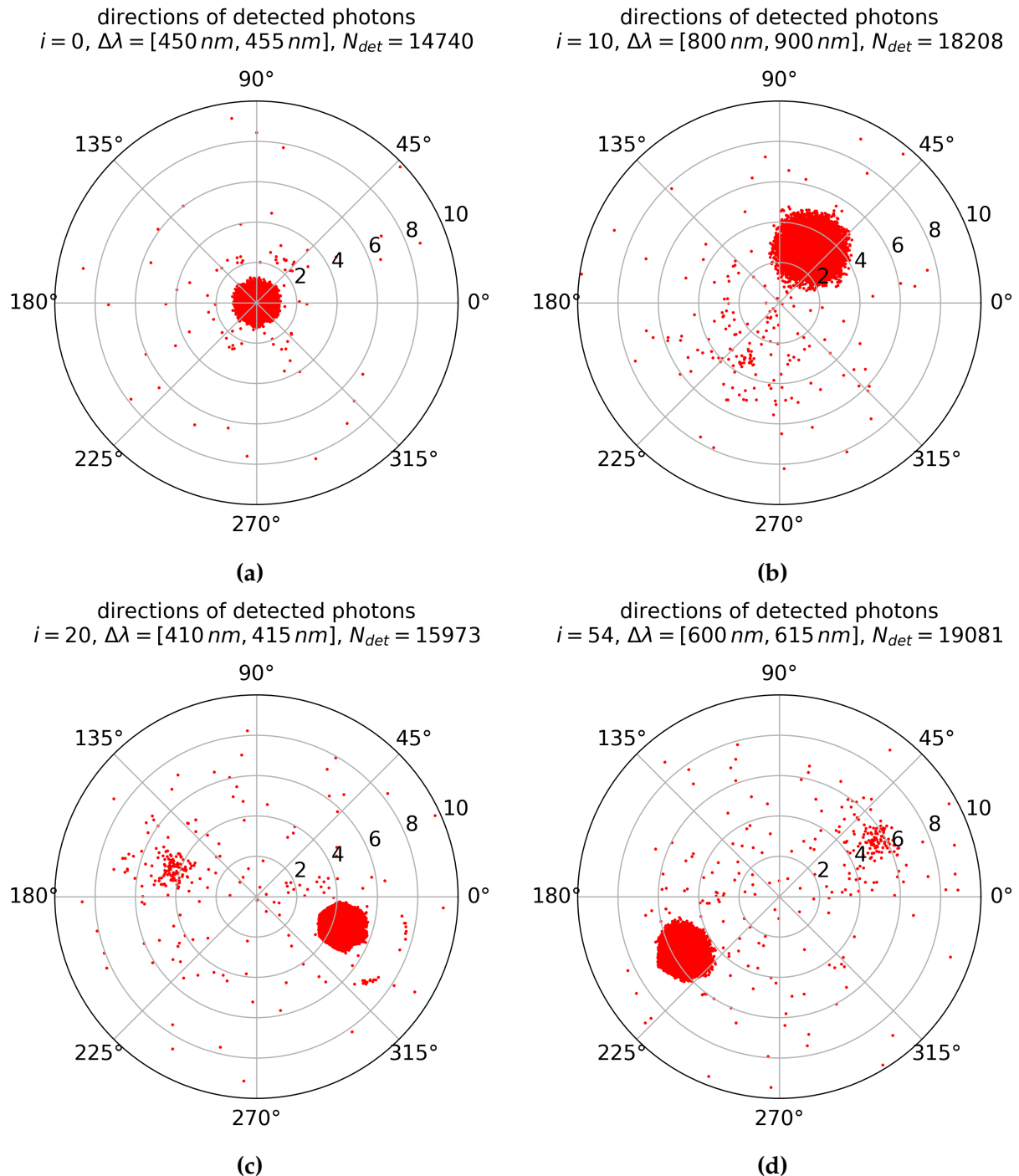
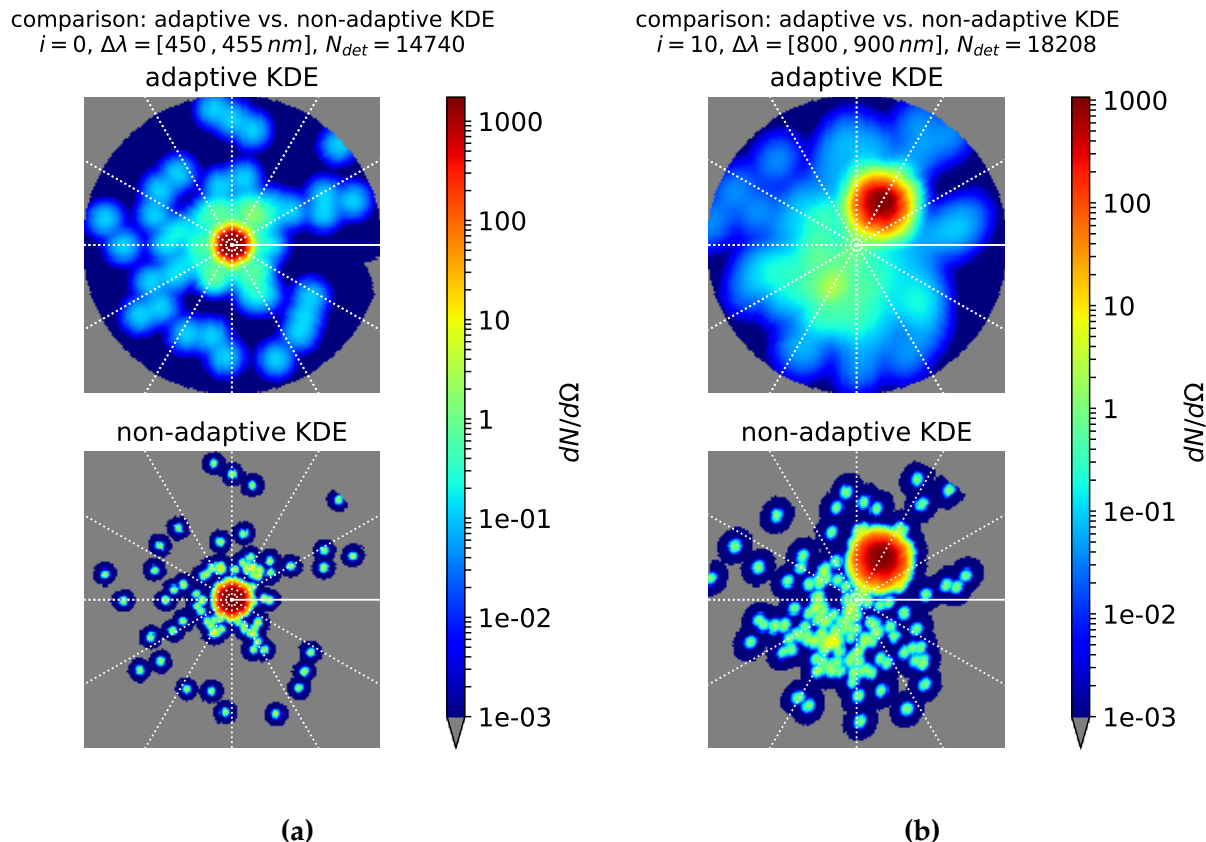


Figure 5.2.: Example: directions of detected photons as a scatter plot. A subset of simulated photon directions that are detected in a given camera pixel i and the wavelength range $\Delta\lambda$ are shown in a polar plot. One can clearly see that there are regions with high and low statistical significance. Additionally, the *ghost image* effect (cf. section 3.1.4) is visible in the non-central pixels ((b), (c), (d)).

The regions with very sparse “dots” can only arise from random scattering processes inside the optical system since they are outside the main field of view and the *ghost image* region (cf. section 3.1.4). Thus, the probability density should be rather constant in these scattering regions. For the KDE, one achieves this by increasing the kernel bandwidth. Simultaneously, the “real” detection regions should be described precisely which is done by reducing the bandwidth. The need of an adaptive kernel density approach is given. Figure 5.3 strikingly shows the difference between an adaptive and a non-adaptive KDE.



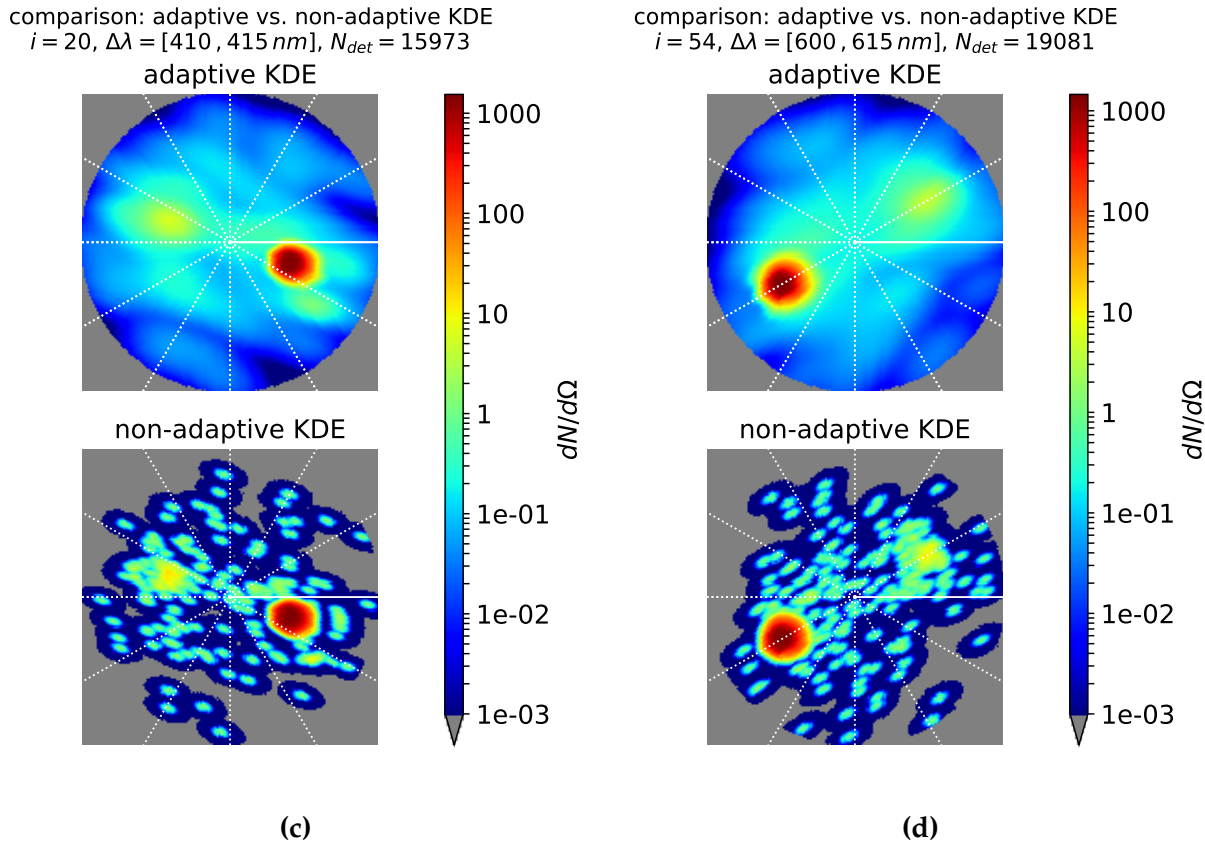


Figure 5.3.: Comparison: adaptive vs. non-adaptive KDE. Evaluation of the direction distributions shown in figure 5.2 on a HEALPix grid with $N_{\text{side}} = 512$. The plot shows a disc up to $\theta = 10^\circ$ and the white dotted meridians have an azimuth distance of 30° . The azimuth ϕ starts at the solid white line and goes around counter-clockwise. Differences between an adaptive (top) and non-adaptive (bottom) KDE approach are visible. Especially in the region with low statistics (scattering region), the non-adaptive KDE is dominated by the fluctuations while adaptive KDE blurs the probability density more strongly.

Anyway, the detection distributions can now be calculated and renormalized for each of the 61 camera pixels and 50 wavelength bins which result in 3050 so called *detection efficiency maps* shown in the next section 5.3.

5.3. Detection Efficiency Maps

By following the strategy described in chapter 4 and considering the findings from sections 5.1 and 5.2, one can now finally calculate *detection efficiency maps*. For each camera pixel i and wavelength bin $\Delta\lambda$, these maps show the probability $\epsilon_{i,\Delta\lambda,HP}$ to detect a photon with wavelength $\lambda \in \Delta\lambda$ in camera pixel i as a function of its origin direction (θ, ϕ) which is coded in the ordinal number HP of the corresponding HEALPix. For the error estimation, the bootstrapping method presented in section 4.1.2 is used. To get a confident estimation with reasonable computational effort, $N_{\text{bootstrap}} = 10$ bootstrapping iterations are performed.

5.3.1. Choice of HEALPix Pixelization Parameter N_{side}

For the pixelization parameter of the HEALPix model N_{side} (cf. section 4.3.1), one has to choose a reasonable value as well (cf. table 4.1): too fine pixelization would obviously result in a very detailed parameterization. Due to KDE, an “unbinned” detection efficiency is available – at least in origin directions – so that it is technically possible to choose a very fine binning. The problem is that the main goal of the IceAct parameterization is to produce a lookup table that is efficient and capable of evaluating large amounts of Cherenkov photons. An unnecessarily fine HEALPix binning would just blow up the lookup table and quick evaluation is not feasible anymore. To determine the optimal N_{side} of the HEALPix model, the detection efficiency of the central pixel $i = 0$ is considered. As one can see in figure 5.4, the most efficient angular area is below a zenith angle of $\theta = 0.7^\circ$. Usually, this regions are called *field of view* (FOV) which equals the doubled zenith angle 2θ if the FOV is symmetrical around the zenith. Thus, the core field of view of the central pixel is 1.4° . In the transition region $1.4^\circ < 2\theta \leq 2.5^\circ$, the detection efficiency decreases rapidly. Therefore, it is crucial to pixelize this region such that the hexagonal shape of the pixel’s field of view – which is caused by the Winston cones – is described in a sufficient degree of detail in order to have a fairly precise approximation.

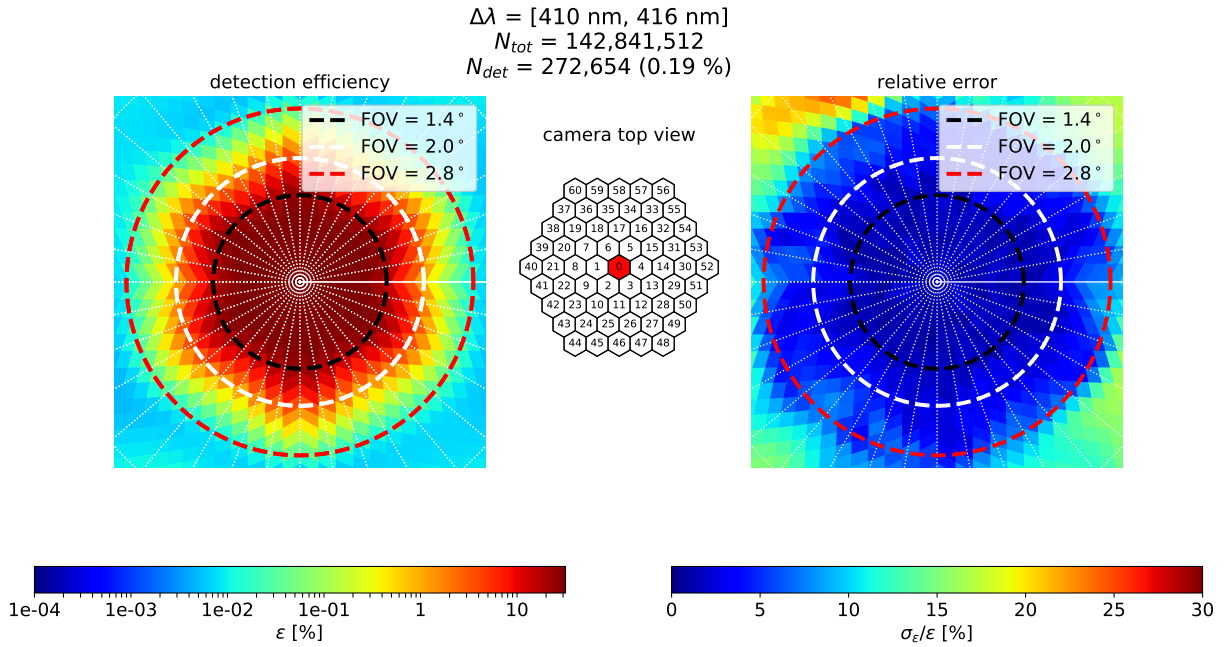


Figure 5.4.: Detection efficiency of central camera pixel. The plot is zoomed into the main detection region up to a zenith angle $\theta = 1.5^\circ$. As a wavelength, the bin around the most efficient wavelength λ^* (cf. section 3.1.1) is chosen. In a field of view below 1.4° , the central pixel has its maximal detection efficiency. The HEALPix parameter in this map is $N_{\text{side}} = 512$. Bootstrapping leads to the relative error shown in the right plot. The interval between the white dashed meridians is $\Delta\phi = 10^\circ$.

As figure 5.4 shows, a HEALPix parameter of $N_{\text{side}} = 512$ is sufficient to describe the hexagonal shape. By applying $N_{\text{side}} = 256$, four HEALPixels would reduce to just one HEALPix, which could hardly describe the edges. On the other side, one gets to $N_{\text{side}} = 1024$ by dividing a HEALPix into four. This results in an unnecessarily high amount of HEALPixels to describe the given shape. Table 5.1 shows the number of enclosed HEALPix(-centers) in the core region ($2\theta \leq 1.4^\circ$) and the transition region ($1.4^\circ < 2\theta \leq 2.5^\circ$) depending on the used HEALPix parameter.

N_{side}	HEALPixels in region	
	$2\theta \leq 1.4^\circ$	$1.4^\circ < 2\theta \leq 2.5^\circ$
256	24	88
512	112	368
1024	480	1380

Table 5.1.: Number of HEALPix centers in regions around the zenith. The numbers for three possible HEALPix models are shown. As characteristic areas, the efficiency core region ($2\theta \leq 1.4^\circ$) and transition region ($1.4^\circ < 2\theta \leq 2.5^\circ$) of the central pixel around the most efficient wavelength λ^* (cf. section 3.1.1) are chosen.

5.3.2. Overview of Results

In this section, some results are presented. At first, the focus is on the maximum detection efficiency. Just because the optics has been optimized to the “best” wavelength $\lambda^* = 411\text{ nm}$ by minimizing the focal spot for this wavelength (cf. section 3.1.2), this does not necessarily imply that the detection efficiency is maximal at λ^* . Indeed, the maximal efficiency is reached between 426 nm and 431 nm for the central camera pixel with $\epsilon_{\max} \approx 33.35\%$ as figure 5.5 shows. One also observes that for the off-axis pixels – i.e. all but the central one – the centroid of the efficiency distributions slightly shifts towards higher wavelengths. The reason is that the focal plane shifts “behind” the camera plane with increasing wavelengths (cf. figure 3.3). The higher the wavelength, the more blurred the image gets and these wavelengths are tendentially seen by more pixels. As a result, more inner pixels are more sensitive to lower and more outer pixels are more sensitive to higher wavelengths.

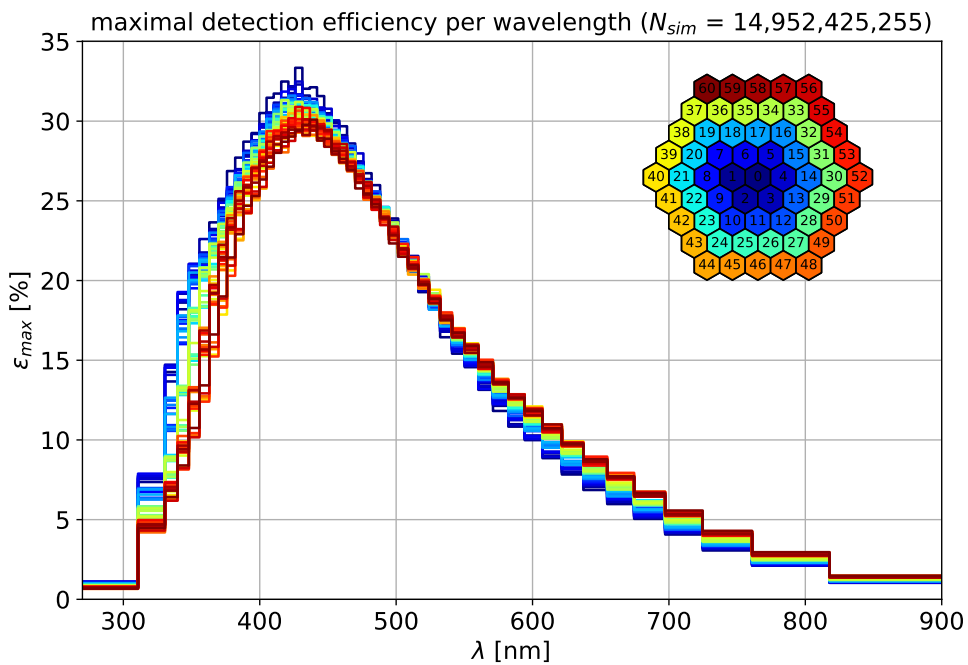
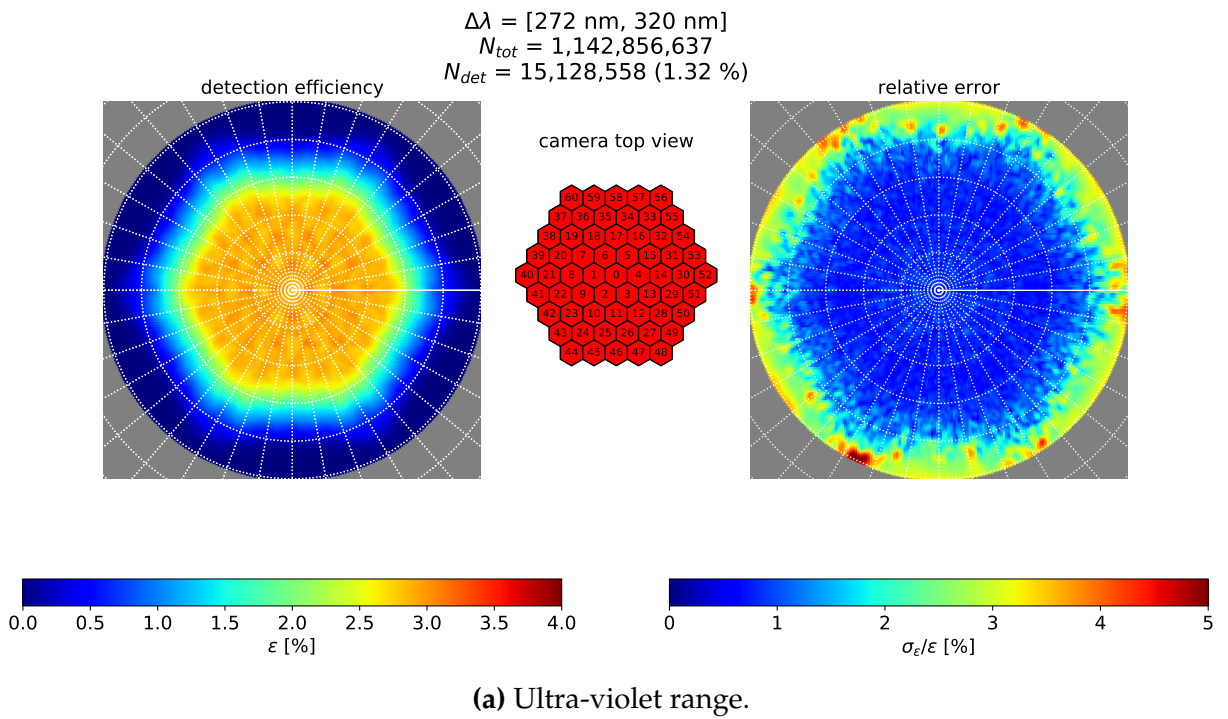


Figure 5.5.: Maximum detection efficiency for each pixel and wavelength. The 61 camera pixels are color-coded via their ordinal number from blue to red. The overall maximum detection efficiency is reached by the central pixel at $\Delta\lambda = [426\text{ nm}, 431\text{ nm}]$ with $\epsilon_{\max} \approx 33.35\%$.

By summing up the individual detection efficiency maps of each pixel, the response of the whole camera to a certain wavelength is given. Figure 5.6 shows these maps for

three characteristic wavelength ranges. What is remarkable is that in the region of focus – i.e. wavelengths for which the focal spot on the camera plane is relatively small – the geometry of the camera is important. One can see very sharp differences between the main field of view of each pixel which corresponds to the Winston cone centers and the Winston cone edges resulting in an approximately 10% lower efficiency (cf. figure 5.6b). For smaller wavelengths where the focus is above the camera plane, a distinct geometry-dependent pattern is not visible except – of course – the overall hexagonal shape. For higher wavelengths, a pattern occurs again, but a barrel-shaped distortion is visible. This is a known optical aberration effect where the magnification decreases with distance from the optical axis like for an image of a fisheye lens.



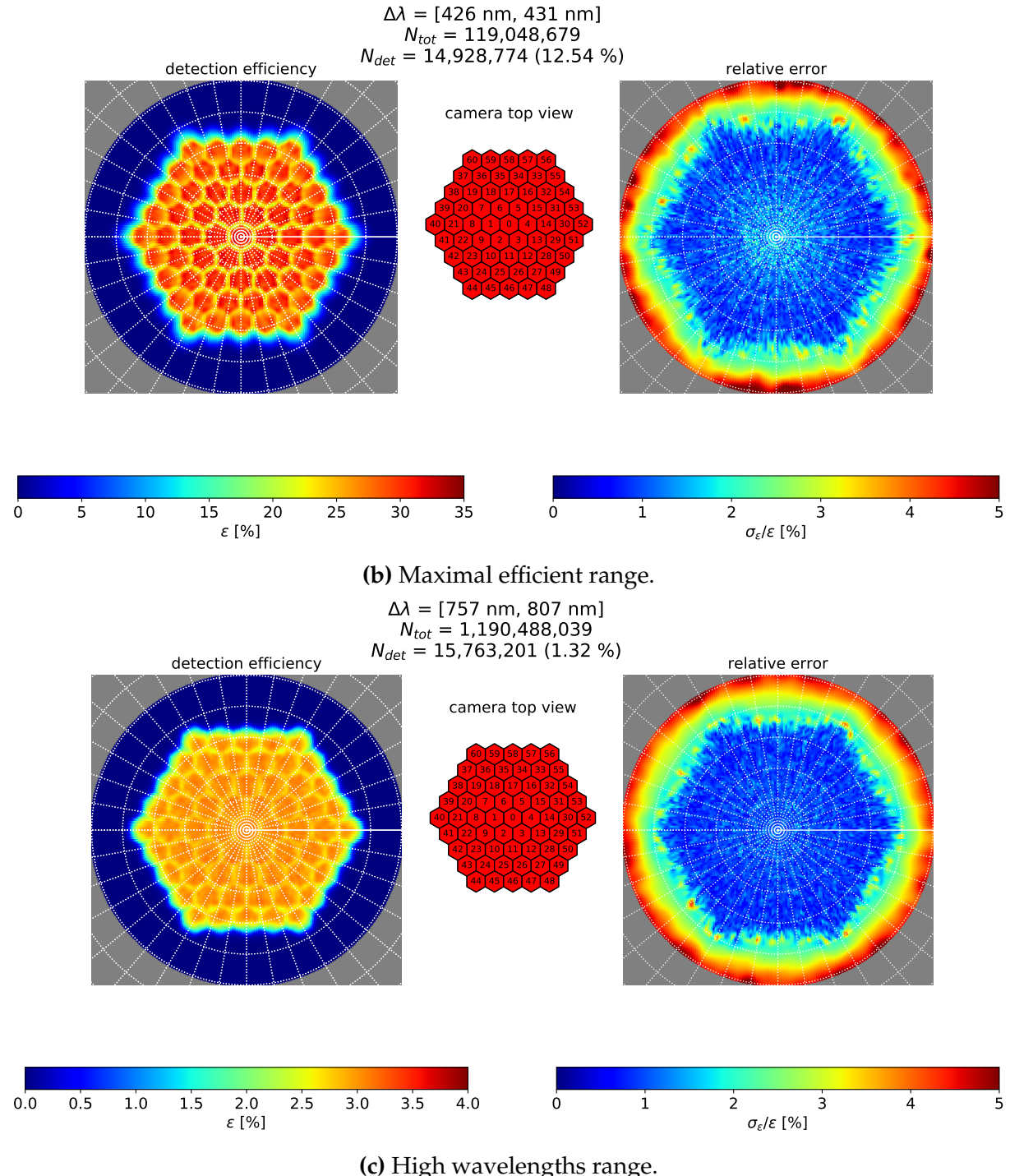
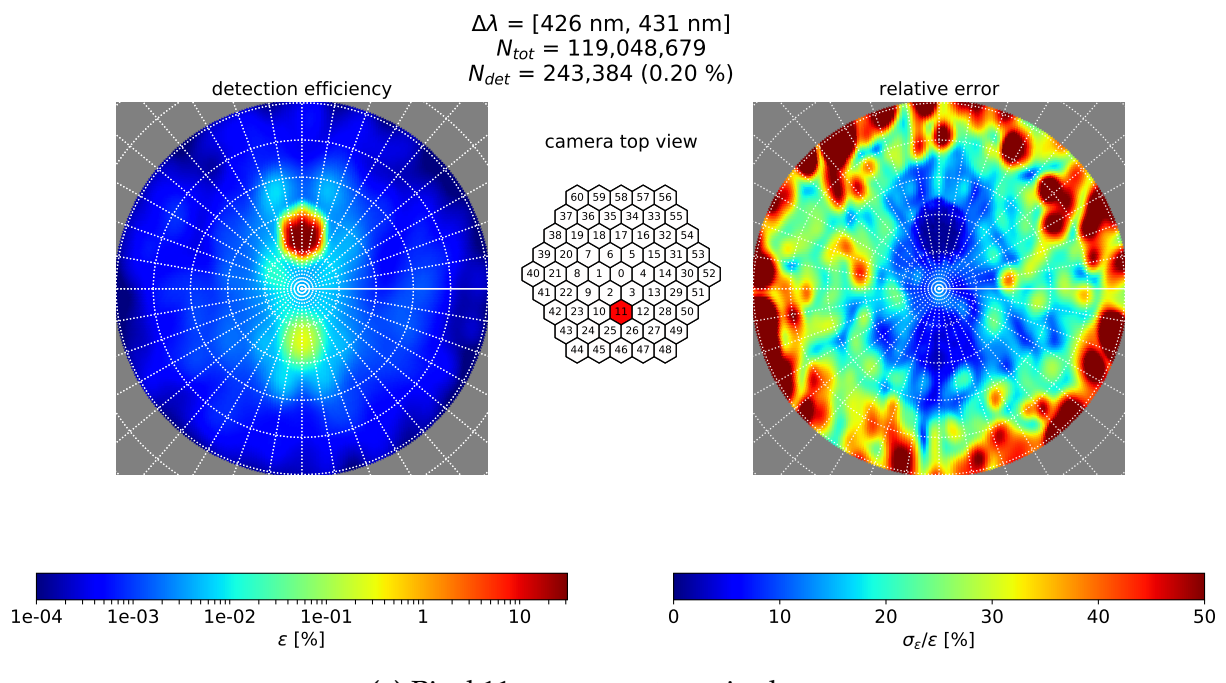


Figure 5.6.: Detection efficiency maps of the full camera. The left plots show the detection efficiency while the right plots show the relative error. Three wavelength regions are chosen: a UV range in (a), the maximum efficiency in (b) and high wavelengths in (c). The white dashed parallels and meridians have the distances $\Delta\theta = 2^\circ$ and $\Delta\phi = 10^\circ$. The azimuth revolves counter-clockwisely starting at the white solid line. Please note the different color mapping for the detection efficiencies.

Interesting optical effects are visible if one plots some off-axis pixels individually. Figure 5.7 shows three of these. Besides the core region, one can also see the ghost image explained in section 3.1.4 on the opposite side in terms of the azimuth. Additionally, there are some spots next to the core and the ghost image region which originate from reflections between the Winston cones' top and Fresnel lens' back side. In blind regions where the detection probability does not exceed $10^{-3}\%$, the estimated efficiency is highly dominated by statistical fluctuations as the plots for relative statistical errors show as well.



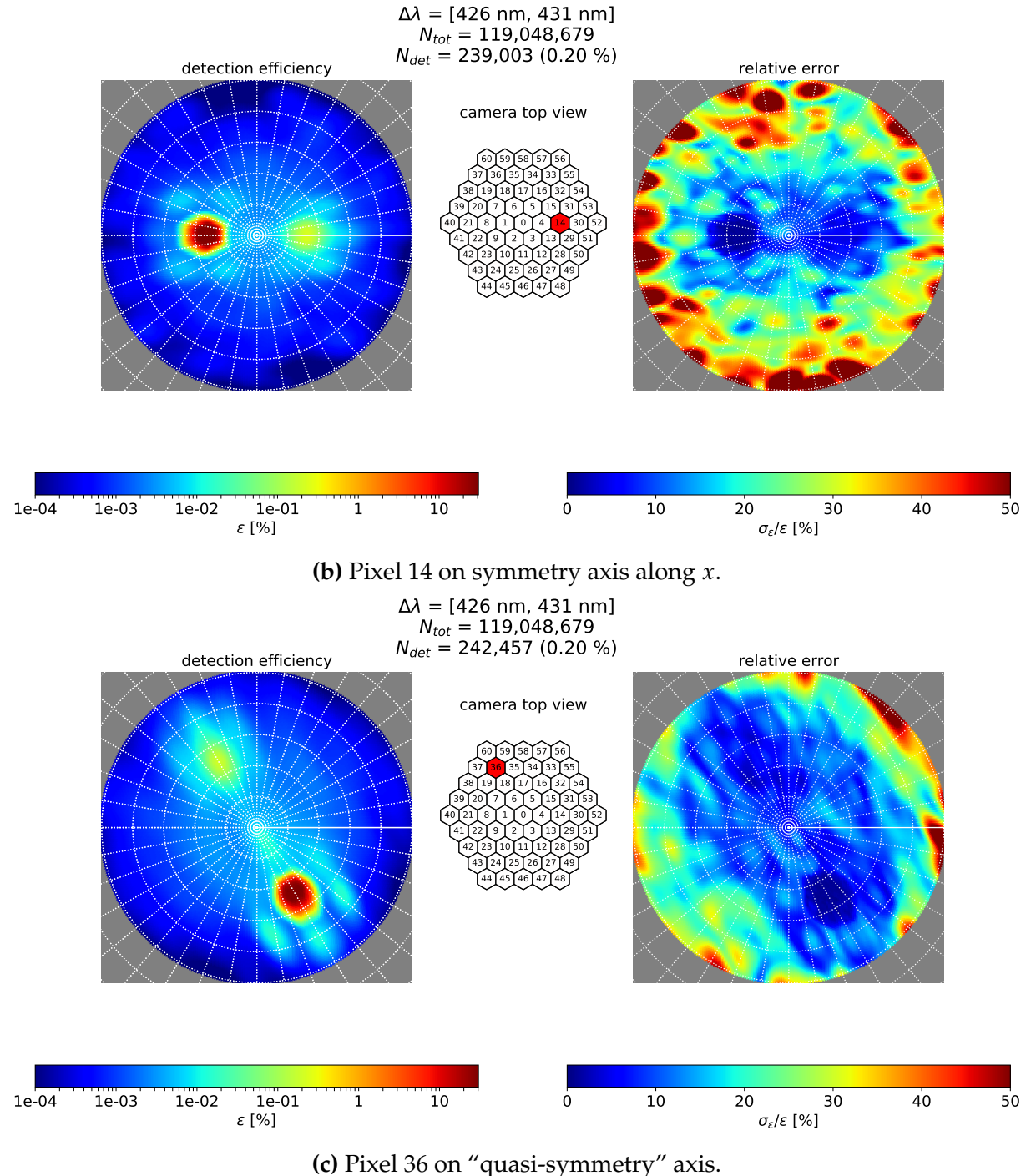


Figure 5.7.: Detection efficiency maps for some off-axis pixels. Similar plots as in figure 5.6 but now for individual camera pixels at the wavelength range with maximum efficiency. Three pixels on symmetry axes are chosen. The two pixels shown in (a) and (b) are on real symmetry axes while the third pixel in (c) is on a symmetry axis of the camera plane but not with respect to the squared SiPMs.

Additional detection efficiency maps can be found in the appendix B.2.

5.4. Lookup Table (LUT)

As the detection efficiency maps are ready now, one has to think about a way to access the information as fast as possible. Usually, this is done by storing the parameterization function evaluated at certain points in a multidimensional array structure known as *lookup table*. Afterwards, events can be “diced” with the given information yielding count histograms for the camera – named *images*.

5.4.1. LUT Production

First of all, one has to define how to iterate over the given information. In this case, one starts with a photon direction (θ, ϕ) translated into the corresponding HEALPix number HP and the wavelength λ of this photon which is assigned to the proper wavelength bin $\Delta\lambda$. The result then should be the response of each pixel to the very same photon, i.e. how probable is it for the photon to be detected in camera pixel i . In order to achieve this, one can evaluate the detection efficiency maps by firstly considering just one HEALPix. For this HEALPix, the detection efficiency for all wavelength bins and all camera pixels is read out which is exemplarily shown in figure 5.8.

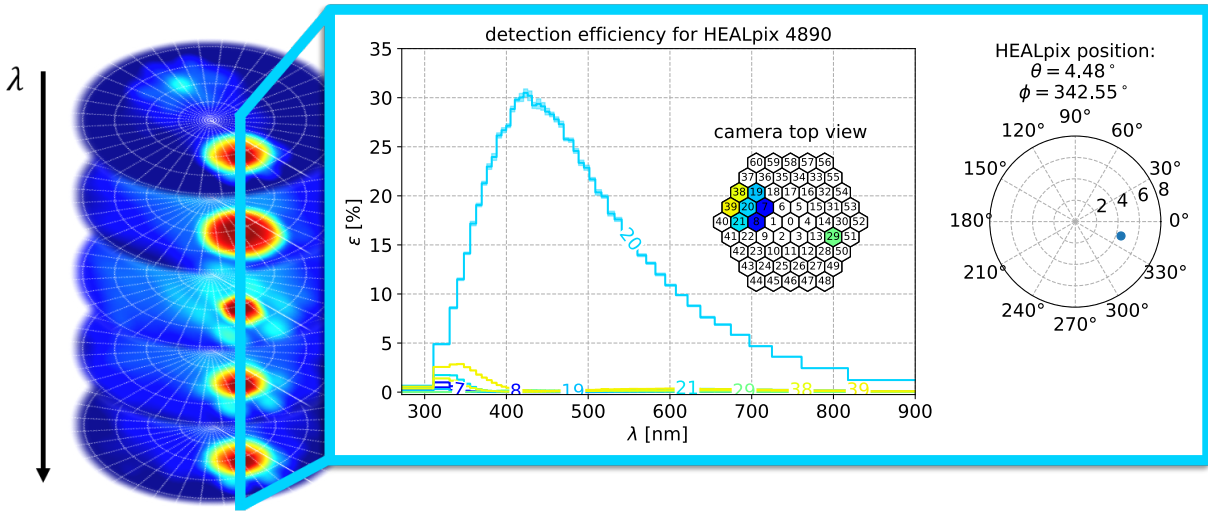


Figure 5.8.: Visualization for the lookup table transposition. A certain HEALPix (here: $HP = 4890$) is considered. For one camera pixel, the detection efficiency is read from the maps throughout all wavelength bins. In this example, some maps for pixel 20 are chosen. Doing this for all camera pixels yields to the blue-framed plot. For the considered HEALPix one gets the wavelength-dependent detection efficiency for each camera pixel. The “camera top view” plot shows the camera as seen from the lens. Pixels that have a maximum detection efficiency greater than 0.1 % are emphasized with colors. The detection efficiency functions of all other pixels are not plotted. Besides, the HEALPix center coordinates are given with a polar plot. More of these plots are shown for certain HEALPixels in the appendix B.3.

By iterating over each HEALPix, one gets $N_{HP} \times N_{\Delta\lambda}$ pixel-by-pixel detection efficiency arrays where N_{HP} is the total number of HEALPix covered by simulation and $N_{\Delta\lambda}$ the number of wavelength bins. These sub-arrays are further named as $\epsilon_{HP,\Delta\lambda}$ and contain the detection efficiency ϵ_i for each camera pixel i (also called *pixel response*).

Additionally, one can even improve the structure of these sub-arrays by not just saving the single responses ϵ_i ordered by pixel number, but saving the cumulative responses. Then, the k -th of totally 60 elements in the sub-array is defined as

$$\epsilon_k^{\text{abs}} = \sum_{i=0}^k \epsilon_i, \quad (5.1)$$

i.e. ϵ_k^{abs} is the probability to detect the photon in any pixel with number $i \in [0, k]$. Additionally, it is

$$\epsilon_k^{\text{abs}} < 1, \quad (5.2)$$

where the last element $\epsilon_{60}^{\text{abs}}$ is the total detection probability of the camera. Distances between the elements represent the responses of the individual camera pixels. The advantage of saving the cumulative sum rather than actual responses gets clear in the next section 5.4.2. Schematically, the lookup process can be described by

$$\gamma \rightarrow \begin{cases} (\theta, \phi) & \rightarrow HP \\ \lambda & \rightarrow \Delta\lambda \end{cases} \Rightarrow \epsilon_{HP, \Delta\lambda}^{\text{abs}} = \{\epsilon_k^{\text{abs}}\}_{k=0}^{60}. \quad (5.3)$$

The HEALPix resolution used for parameterization of IceAct is $N_{\text{side}} = 512$. With $\theta_{\max} = 10^\circ$, this results in a total “active” HEALPix number of $N_{HP} = 24\,420$. Additionally, the wavelengths are divided into $N_{\Delta\lambda} = 50$ bins in the interval [272 nm, 900 nm] (cf. section 5.1). For the 61-pixel camera, this results in $N_{HP} \cdot N_{\Delta\lambda} \cdot 61 = 74\,481\,000$ numbers to be saved. The needed disk space for this lookup table is 284 MiB by using 32 bit float as data type¹⁴.

5.4.2. LUT Readout – “Event Dicing”

Now that the data is properly stored in the LUT, an evaluation algorithm has to be elaborated. In the following, the principle to evaluate N photons is described step by step.

1. For each direction the corresponding HEALPix number is calculated.¹⁵

$$\{(\theta_i, \phi_i)\}_{i=1}^N \rightarrow \{HP_i\}_{i=1}^N \quad (5.4)$$

2. Only valid photons are evaluated. A photon is valid if its HEALPix number HP_i is in the lookup table – i.e. below the cut-off – and if its wavelength λ_i is in the wavelength range covered by the lookup table $[\lambda_{\min}, \lambda_{\max}]$. $N^* \leq N$ photons are valid. Invalid photons are counted.

$$\text{valid} := HP_i < N_{HP} \wedge \lambda_i \in [\lambda_{\min}, \lambda_{\max}] \quad (5.5)$$

¹⁴ Since also the information about wavelength binning, HEALPix model, and maximum simulated zenith angle has to be included, the lookup table file might need slightly more space.

¹⁵ In this thesis, the evaluation algorithm is implemented with Python. For HEALPix calculations, the package *healpy* is used.

3. For all N^* photons, the corresponding wavelength bin is determined.

$$\{\lambda_{i^*}\}_{i^*=1}^{N^*} \rightarrow \{\Delta\lambda_{i^*}\}_{i^*=1}^{N^*} \quad (5.6)$$

Here, the index of the assigned wavelength bin rather than the actual range is important for the lookup table query.

4. The actual lookup table query is performed. Thus, every valid photon gets its proper pixel response array.

$$\{HP_{i^*}, \Delta\lambda_{i^*}\}_{i^*=1}^{N^*} \rightarrow \{\epsilon_{HP_{i^*}, \Delta\lambda_{i^*}}^{\text{abs}}\}_{i^*=1}^{N^*} \quad (5.7)$$

5. For each valid photon i^* , a random number $r_{i^*} \in [0, 1]$ is diced and sorted into the corresponding response array. Now, the advantage of saving the cumulative rather than the absolute responses (cf. section 5.4.1) becomes clear. By definition, the cumulative responses are sorted in ascending order¹⁶. As a result, the position k where the random number is sorted in equals the ordinal number of the camera pixel where the photon is detected. If the random number is sorted in at the 61-th position – i.e. at the end – this means that the photon is not detected. The cumulative saving enables a lookup process that is only based on comparative operations which are very fast.
6. The resulting sorting positions k_{i^*} can now be histogramized which gives the final image seen by the camera.

¹⁶ This is the case if all numbers are non-negative like it is the case for the camera pixel responses. Otherwise, the cumulative sequence may not be sorted.

5.5. Application on CORSIKA Air Shower Events

With the lookup table, one can finally produce event displays – or images – of simulated air showers. A commonly used toolkit for detailed Monte-Carlo simulation of cosmic-ray air showers is *CORSIKA*¹⁷ [58]. It is capable of simulating the direction and energy of Cherenkov photons which emerge from air showers.

The plots in figure 5.9 show some images of air showers simulated with CORSIKA. Three different primaries are induced: proton, iron, and photon (gamma). The wavelength or respectively the energy of Cherenkov photons could possibly be simulated directly within CORSIKA as stated before but this results in a large amount of data and a longer simulation time. Therefore, just the direction of some Cherenkov photons that hit the detector surface in a certain region is stored. For the lookup process, the wavelength of each photon is drawn from the Cherenkov spectrum shown in figure 1.5 by extrapolating wavelengths above 700 nm with a linear function. More details about possible options with CORSIKA and the simulation process can be found in the CORSIKA manual [59].

In order to take into account the effective area of the telescope, only Cherenkov photons that hit a circular area within a diameter of the glass plate $d = 650.3$ mm are evaluated. This holds for the case of an upright telescope. For a telescope tilted by a zenith angle θ^* , the projected effective area is

$$A_{\text{eff}}^* = A_{\text{eff}} \cos \theta^*. \quad (5.8)$$

However, the events shown in figure 5.9 are evaluated for the simple case of a single, upright telescope.

¹⁷ COsmic Ray Simulations for KAscade

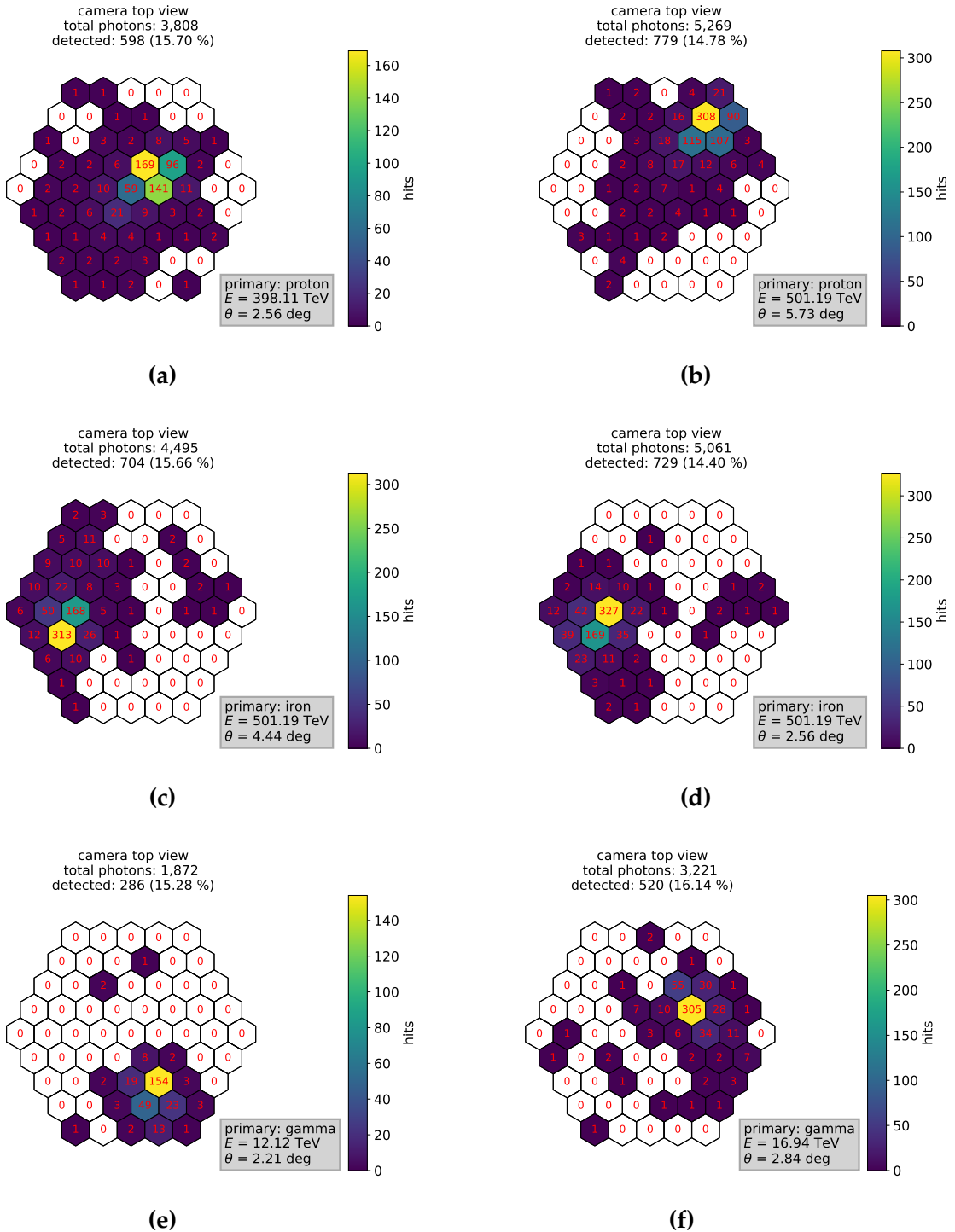


Figure 5.9.: Camera images diced with the lookup table. The red numbers in the hexagonal pixels count the number of detected photons in the respective pixel. In these events, only the direction of Cherenkov photons is simulated by CORSIKA. The wavelengths of the photons are drawn from the Cherenkov spectrum given in figure 1.5.

CHAPTER 6.

Summary and Outlook

The successful parameterization of the full IceAct optics makes it now possible to evaluate Monte-Carlo data from cosmic-ray air showers with low time and computational effort. A detailed knowledge on how IceAct images the Cherenkov light can now be applied to estimate the veto and cosmic ray composition measurement capabilities for a single telescope but also for an array of many IceAct telescopes. A proposed design consists of deploying multiple IceAct *stations* with 7 telescopes each – 1 central upright and 6 tilted, surrounding ones. Since the parameterization can easily be adapted for tilted telescopes by coordinate transformation and considering the different effective area, this layout can also be tested for its imaging capabilities.

The IceAct demonstrator telescope was equipped with different SiPMs and round, hollow aluminum Winston cones. Previous simulation studies showed a maximum detection efficiency of about 19 % at $\lambda = 454\text{ nm}$ [15]. With the solid PMMA Winston cones and the MicroFJ SiPM, IceAct reaches a maximum detection efficiency of about 33 % between 426 nm and 431 nm.

IceAct embodies one of multiple applications of compact imaging air-Cherenkov telescopes. Therefore, the simulation can be used or easily adapted for similar experiments like HAWC’s Eye, FAMOUS, or other future projects having the goal of a complementary detection technique for larger-scale surface detector experiments.

Finally, the potential of the GEANT4 simulation is still not fully exploited. For instance, the SiPM simulation toolkit G4SiPM offers much more possibilities. Once a detailed

knowledge of features and properties of the IceAct SiPM is available, G4SiPM is capable to simulate voltage traces for each SiPM. This makes it possible to simulate the response of IceAct not just in an optical but also in an electronic point of view.

APPENDIX A.

Access to the IceAct GEANT4 Simulation

The IceAct GEANT4 simulation is available as a git repository in the RWTH Aachen GitLab:

<https://git.rwth-aachen.de/iceact/simulation>.

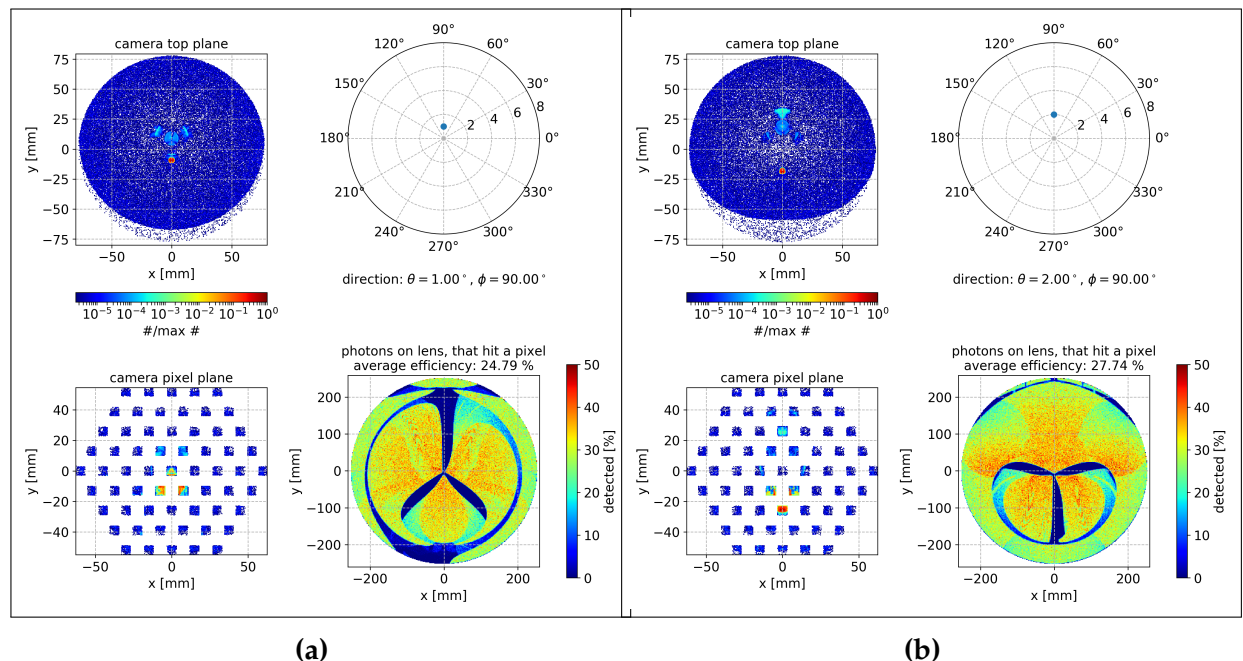
To get access, please contact maurice.guender@rwth-aachen.de

Besides the GEANT4 simulation, the repository contains Python scripts for evaluation of the simulation as well as for production and readout of the lookup table.

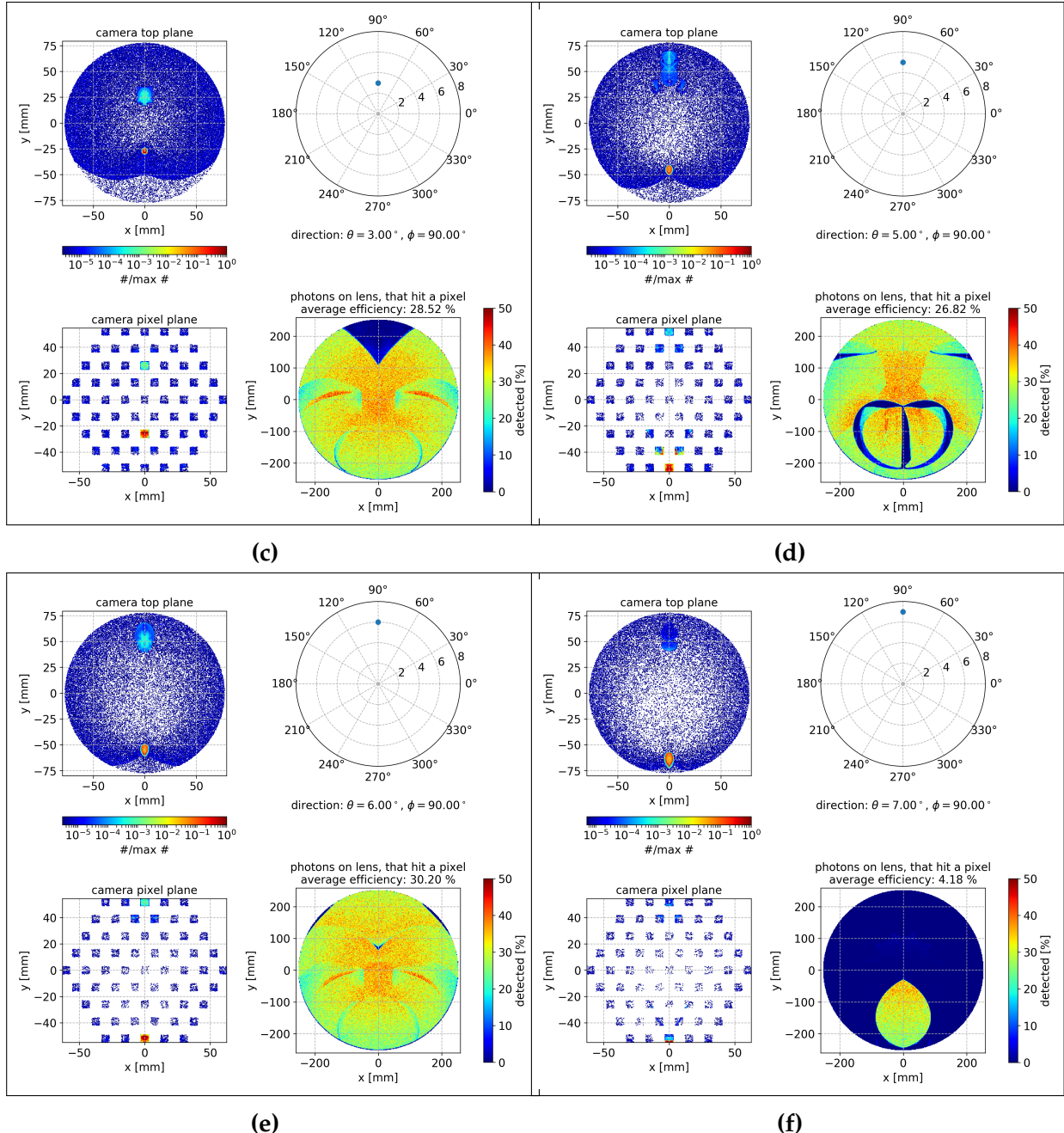
APPENDIX B.

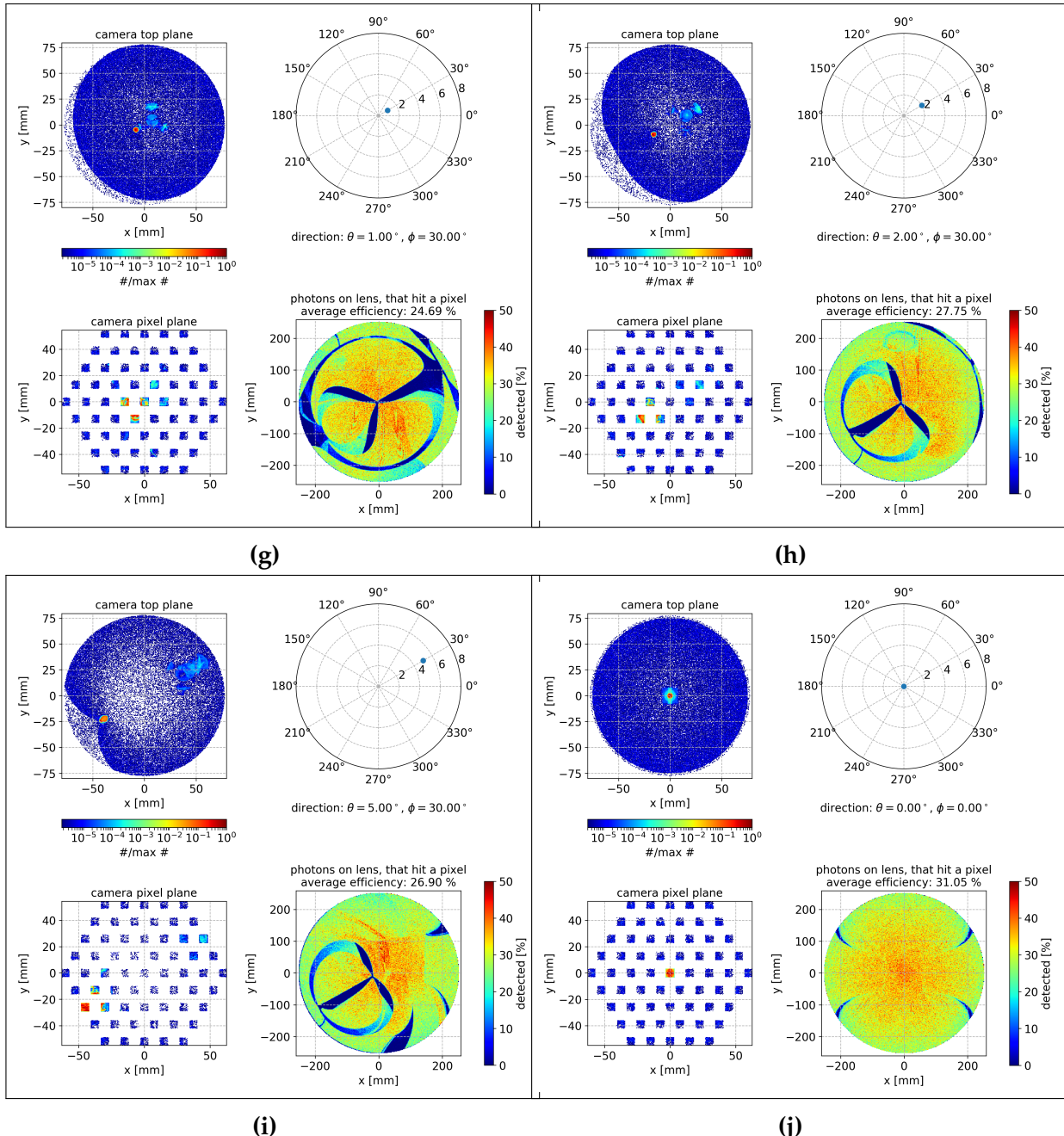
Additional Plots

B.1. Impact-location-dependent Detection Efficiency

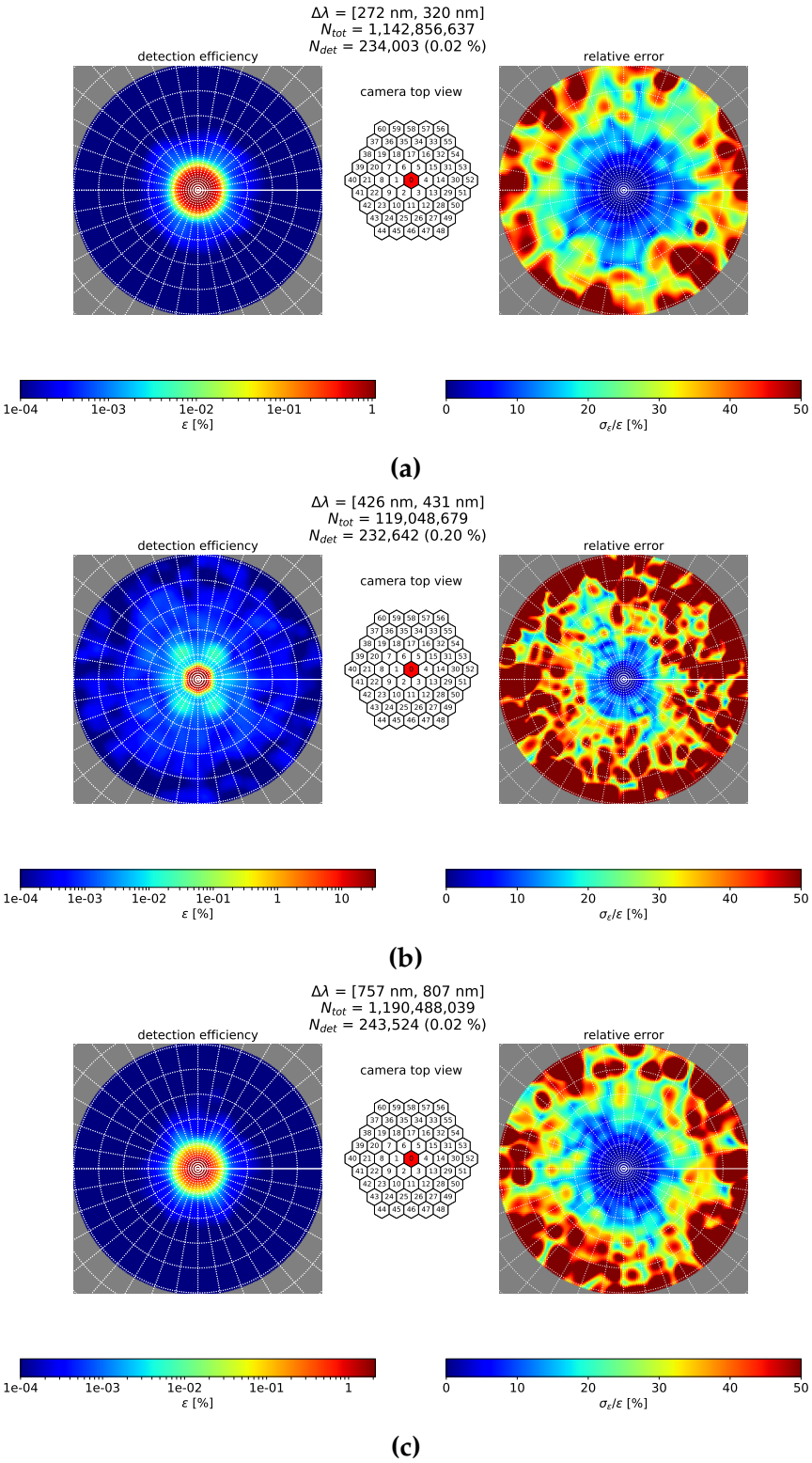


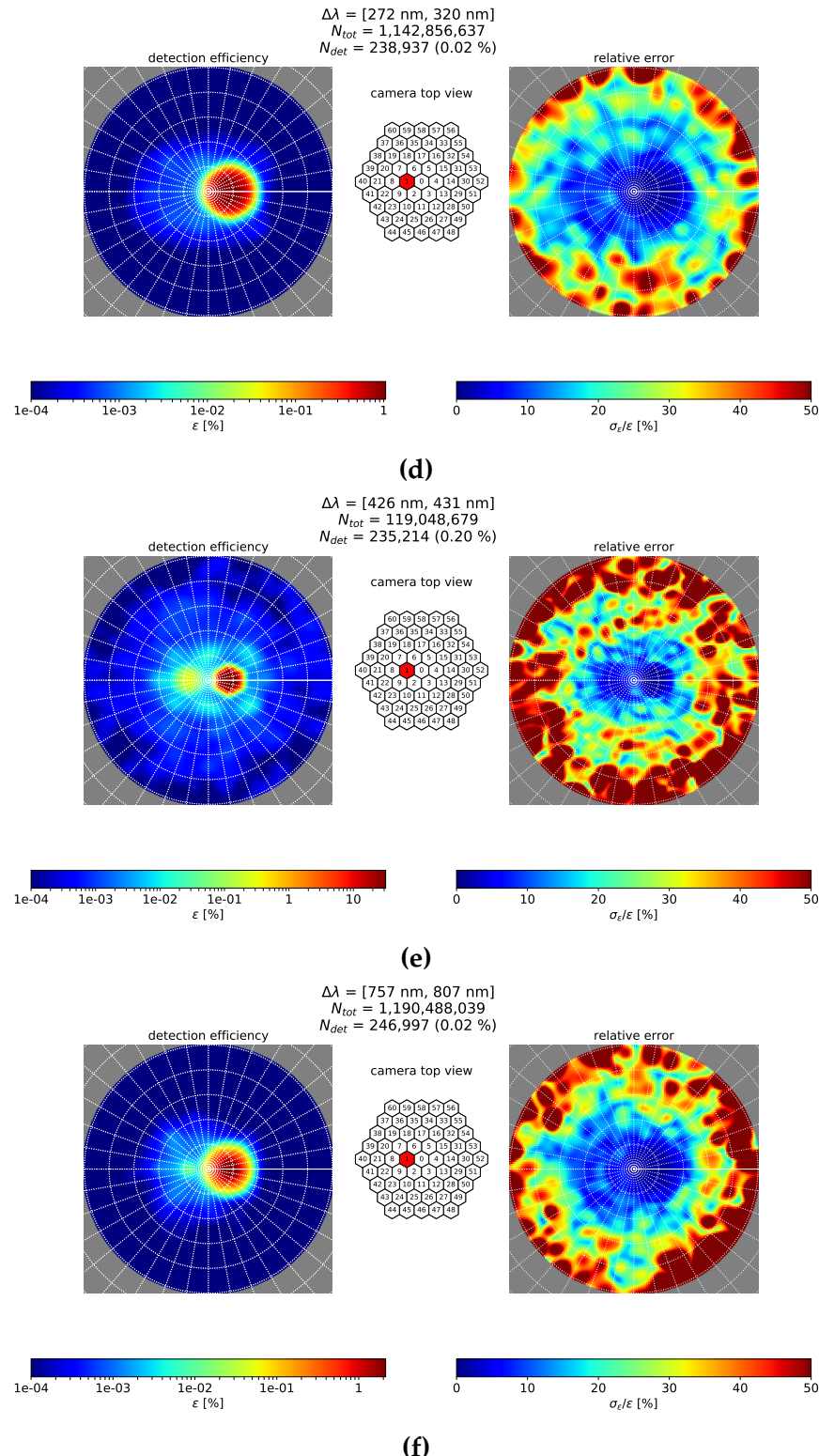
Appendix B. Additional Plots



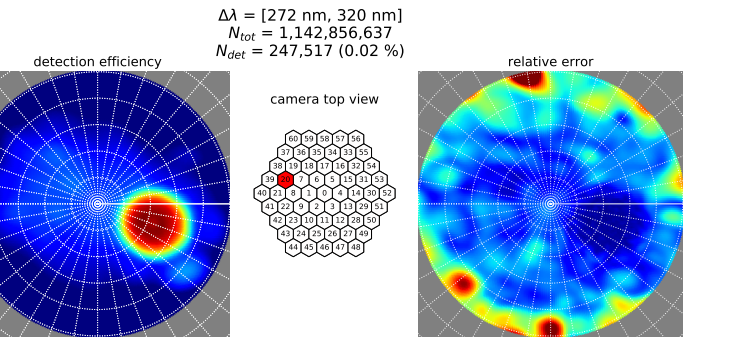


B.2. Detection Efficiency Maps

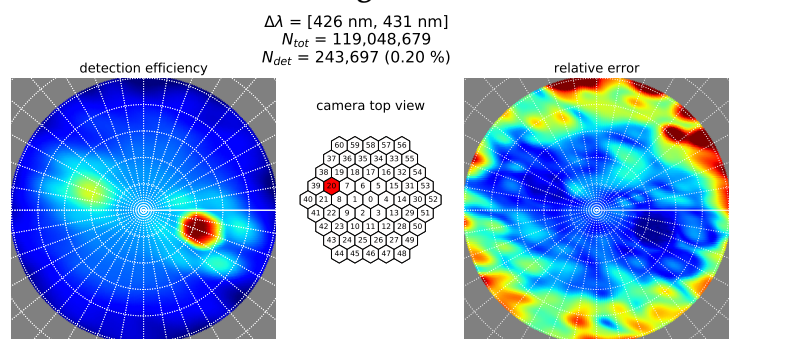




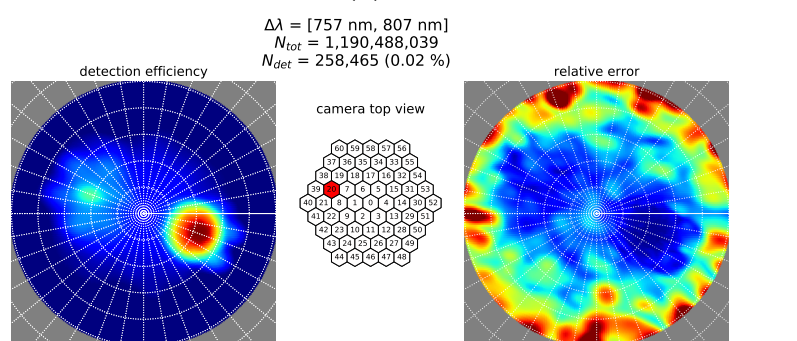
Appendix B. Additional Plots



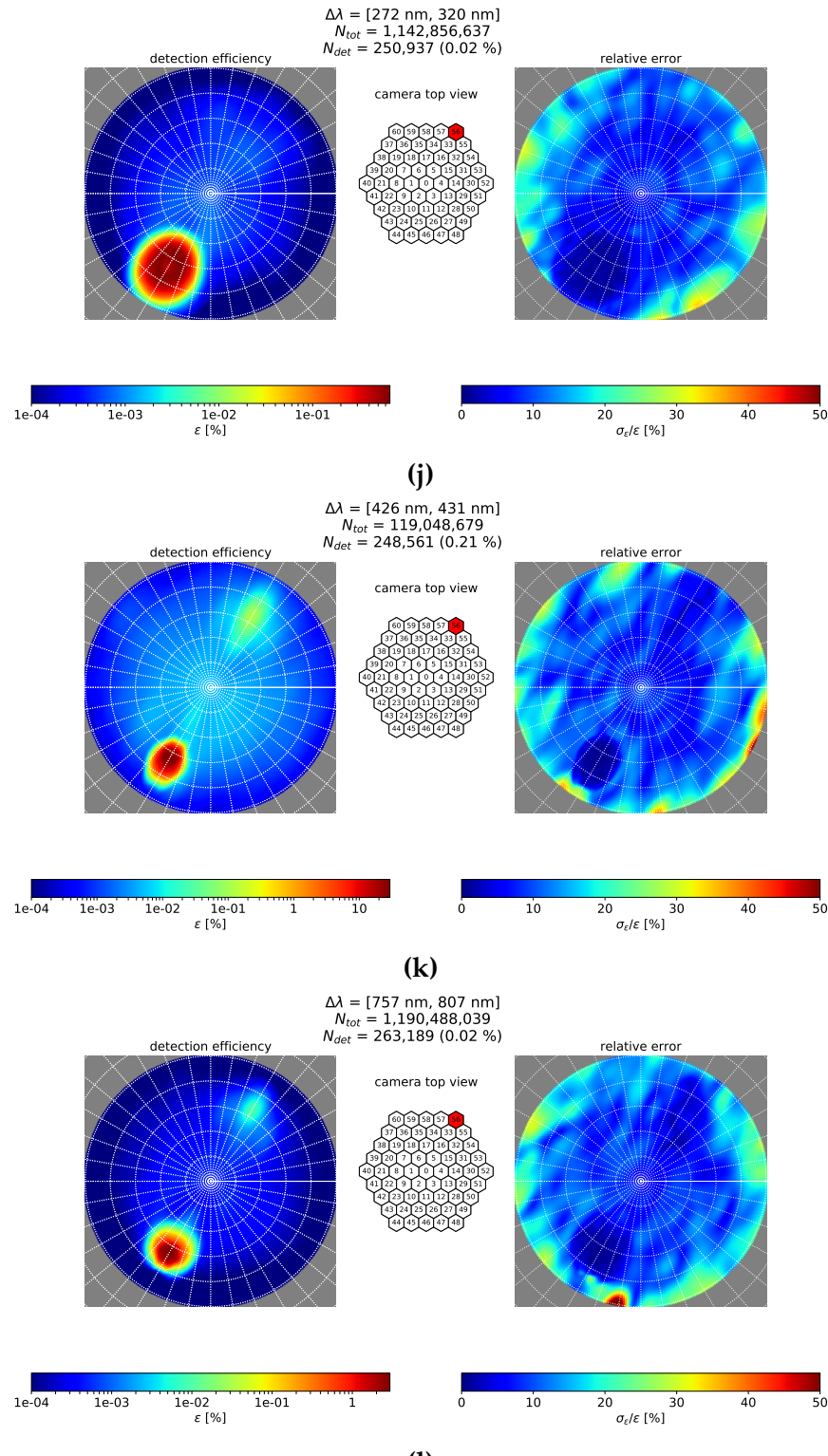
(g)



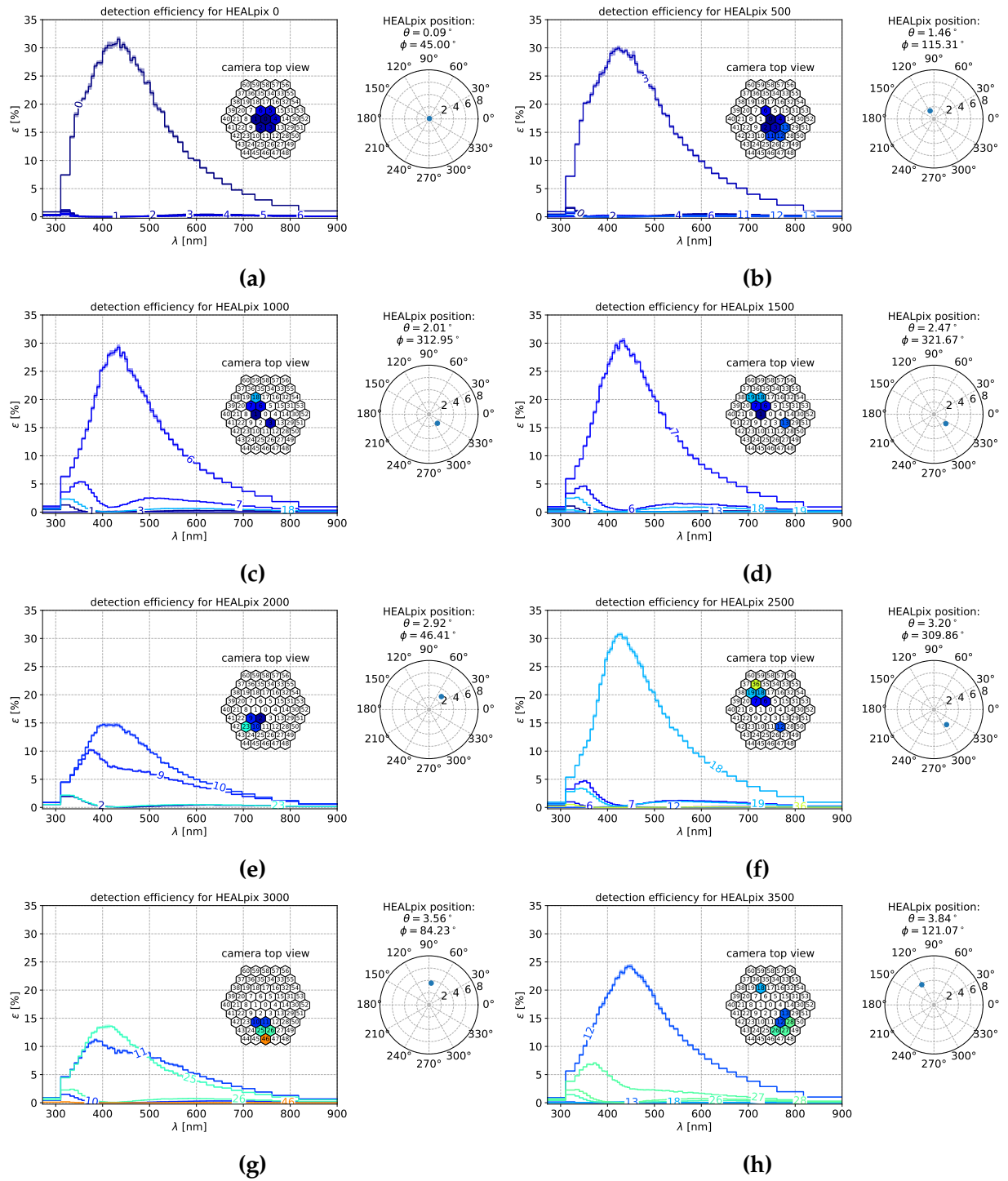
(h)



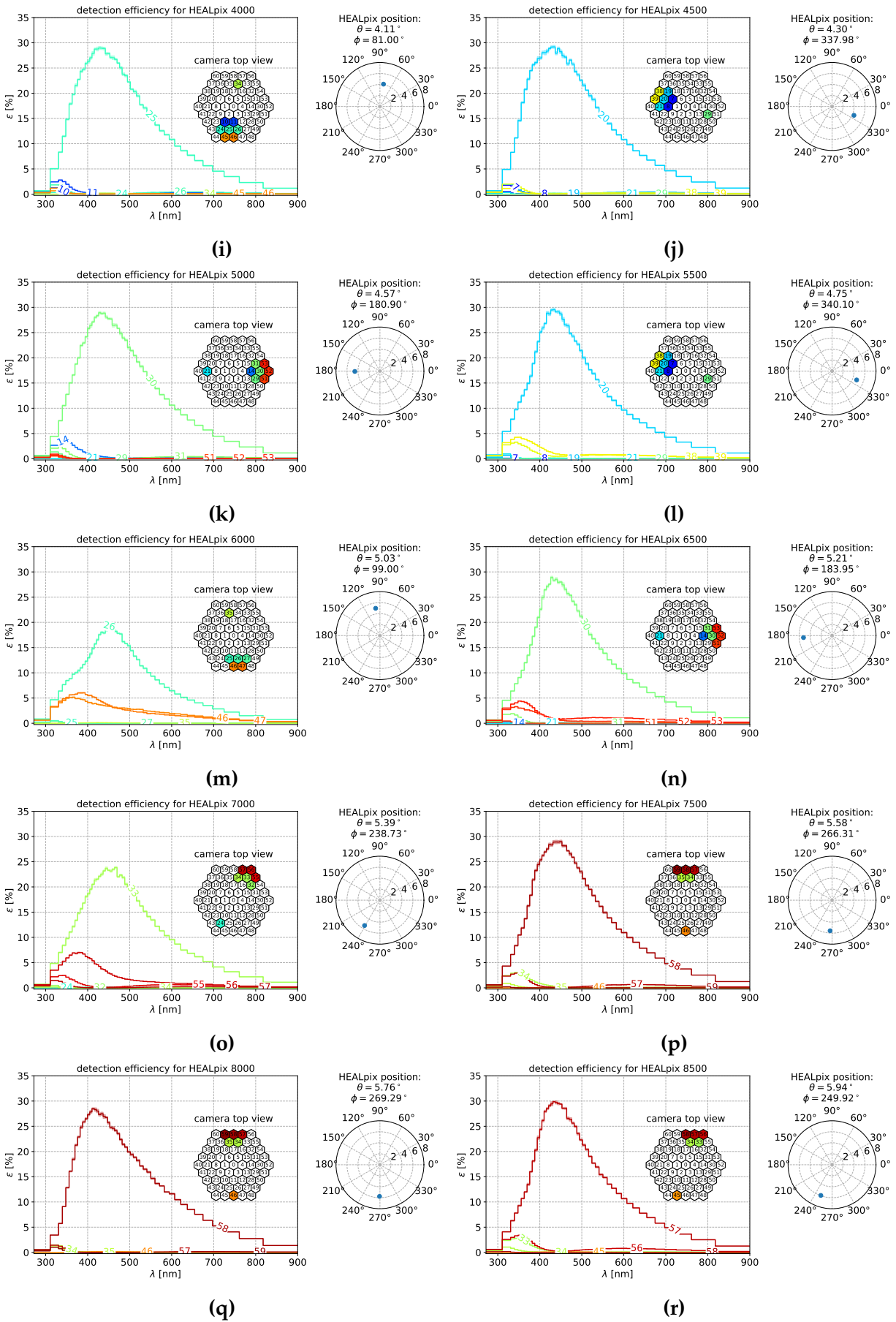
(i)



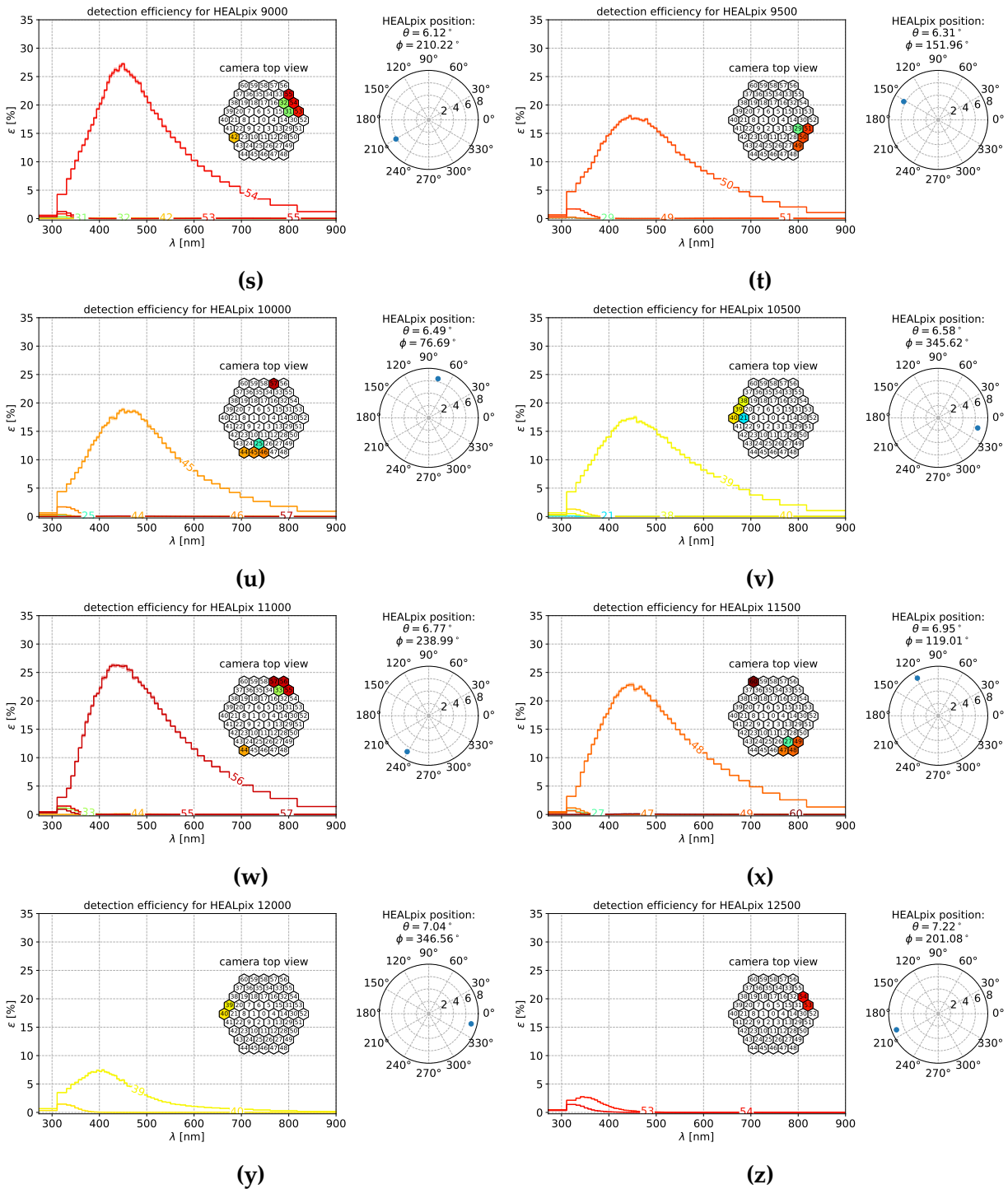
B.3. Camera Pixel Response For Single HEALPixels



B.3. Camera Pixel Response For Single HEALPixels



Appendix B. Additional Plots



Figures

1.1.	Schematic view of IceCube	3
1.2.	Cosmic ray energy spectrum	5
1.3.	Schematic view of extensive air showers	7
1.4.	Illustration for the Cherenkov effect	9
1.5.	Cherenkov spectrum	10
1.6.	Different techniques for air shower detection	11
1.7.	Artwork of the proposed CTA site at ESO’s Paranal Observatory	13
1.8.	Sketch of the IceAct telescope	15
1.9.	The IceAct telescope on top of the IceCube Laboratory (ICL)	16
2.1.	GEANT4 logo	17
2.2.	GEANT4 category diagram	18
2.3.	Refractive index of used materials	19
2.4.	Transmission of used materials	20
2.5.	Basic IceAct camera layout	22
2.6.	IceAct GEANT4 model	23
2.7.	Comparison conventional vs. Fresnel lens	24
2.8.	Fresnel groove	25
2.9.	Fresnel side-profile	26
2.10.	IceAct camera	27
2.11.	Sketch of a Winston cone	28
2.12.	Sketches of the IceAct “hex-to-square” Winston cone	30
2.13.	IceAct Winston cone meshing with different maximum edge lengths . . .	31
2.14.	Sketch of a <i>p-n</i> -junction	32
2.15.	Sketch of a “ <i>p-on-n</i> ” G-APD cell	33
2.16.	Structure of an SiPM	34
2.17.	Pulse waveforms of an SiPM	34
2.18.	Technical sketch of the IceAct SiPM	36

2.19. Photon detection efficiency of the IceAct SiPM	37
3.1. “Best” wavelength	40
3.2. Aberration radius on the focal plane	42
3.3. Caustic histograms for the focal plane shift	43
3.4. Zoomed-out caustic histogram	44
3.5. Image produced by the IceAct Winston cone for vertical light	45
3.6. Comparison between GEANT4 and Zemax simulation	46
3.7. Schematic sketch for the “ghost image” beam path	48
3.8. Symmetry axes of the IceAct camera	49
3.9. Detection profiles in symmetry axis along x	50
3.10. Detection profiles in quasi-symmetry axis	51
3.11. Detection profiles in symmetry axis along x	52
3.12. Coordinate system used in GEANT4 and for the parameterization	53
4.1. Example KDE with different smoothing	56
4.2. Pixelization scheme of the HEALPix algorithm	61
4.3. Example: KDE renormalization	65
5.1. Constant vs. adaptive wavelength binning	68
5.2. Example: directions of detected photons as a scatter plot	69
5.3. Comparison: adaptive vs. non-adaptive KDE	71
5.4. Detection efficiency of central camera pixel	73
5.5. Maximum detection efficiency for each pixel and wavelength	74
5.6. Detection efficiency maps of the full camera	76
5.7. Detection efficiency maps for some off-axis pixels	78
5.8. Visualization for the lookup table transposition	80
5.9. Camera images diced with the lookup table	84

Tables

2.1. Sellmeier coefficients for PMMA	21
3.1. File size of Winston cone model for different mesh size	47
3.2. Parameterization simulation parameters	54
4.1. HEALPix parameters and resulting angular resolutions	62
5.1. Number of HEALPix centers in regions around the zenith	73

Literature

- [1] M. G. AARTSEN et al. "The IceCube Neutrino Observatory: Instrumentation and Online Systems". In: *JINST* 12.03 (2017), P03012. DOI: 10.1088/1748-0221/12/03/P03012. arXiv: 1612.05093 [astro-ph.IM] (cit. on p. 3).
- [2] M. G. AARTSEN et al. "Evidence for High-Energy Extraterrestrial Neutrinos at the IceCube Detector". In: *Science* 342 (2013), p. 1242856. DOI: 10.1126/science.1242856. arXiv: 1311.5238 [astro-ph.HE] (cit. on p. 4).
- [3] M. G. AARTSEN et al. "Neutrino emission from the direction of the blazar TXS 0506+056 prior to the IceCube-170922A alert". In: *Science* 361.6398 (2018), pp. 147–151. DOI: 10.1126/science.aat2890. arXiv: 1807.08794 [astro-ph.HE] (cit. on p. 4).
- [4] J. AUFFENBERG. "IceAct: Imaging Air Cherenkov Telescopes with SiPMs at the South Pole for IceCube-Gen2". In: *PoS ICRC2017* (2018), p. 1055. DOI: 10.22323/1.301.1055 (cit. on pp. 4, 14).
- [5] J. VAN SANTEN. "IceCube-Gen2: the next-generation neutrino observatory for the South Pole". In: *PoS ICRC2017* (2018), p. 991. DOI: 10.22323/1.301.0991 (cit. on p. 4).
- [6] S. KUNWAR et al. "The IceTop Scintillator Upgrade". In: *PoS ICRC2017* (2018), p. 401. DOI: 10.22323/1.301.0401 (cit. on p. 4).
- [7] A. BALAGOPAL V. et al. "Search for PeVatrons at the Galactic Center using a radio air-shower array at the South Pole". In: *The European Physical Journal C* 78.2 (Feb. 2018), p. 111. ISSN: 1434-6052. DOI: 10.1140/epjc/s10052-018-5537-2. URL: <https://doi.org/10.1140/epjc/s10052-018-5537-2> (cit. on p. 4).
- [8] M. SCHAFEL et al. "Small size air-Cherenkov telescopes for ground detection arrays - a possible future extension?" In: *Proceedings of 35th International Cosmic Ray Conference — PoS(ICRC2017)*. Aug. 2017, p. 786. DOI: 10.22323/1.301.0786 (cit. on pp. 4, 13).
- [9] V. F. HESS. "Über Beobachtungen der durchdringenden Strahlung bei sieben Freiballondfahrten". In: *Z. Phys.* 13 (1912), p. 1084. URL: <https://www.mpi-hd.mpg.de/hfm/HESS/public/HessArticle.pdf> (cit. on p. 4).

- [10] T. K. GAISSER, T. STANEV, and S. TILAV. "Cosmic ray energy spectrum from measurements of air showers". In: *Frontiers of Physics* 8.6 (Dec. 2013), pp. 748–758. ISSN: 2095-0470. DOI: 10.1007/s11467-013-0319-7. URL: <https://doi.org/10.1007/s11467-013-0319-7> (cit. on p. 5).
- [11] J. R. HÖRANDEL. "On the knee in the energy spectrum of cosmic rays". In: *Astroparticle Physics* 19.2 (2003), pp. 193–220. ISSN: 0927-6505. DOI: [https://doi.org/10.1016/S0927-6505\(02\)00198-6](https://doi.org/10.1016/S0927-6505(02)00198-6). URL: <http://www.sciencedirect.com/science/article/pii/S0927650502001986> (cit. on pp. 5, 6).
- [12] J. W. FOWLER et al. "A measurement of the cosmic ray spectrum and composition at the knee". In: *Astroparticle Physics* 15 (Apr. 2000), pp. 49–64. DOI: 10.1016/S0927-6505(00)00139-0 (cit. on p. 5).
- [13] M. M. SHAPIRO, ed. *Composition and Origin of Cosmic Rays*. Springer Netherlands, 1983. DOI: 10.1007/978-94-009-7166-0. URL: <https://doi.org/10.1007/978-94-009-7166-0> (cit. on p. 6).
- [14] G. T. ZATSEPIN and V. A. KUZMIN. "Upper limit of the spectrum of cosmic rays". In: *JETP Lett.* 4 (1966). [Pisma Zh. Eksp. Teor. Fiz. 4, 114(1966)], pp. 78–80 (cit. on p. 6).
- [15] T. NIGGEMANN. "The silicon photomultiplier telescope FAMOUS for the detection of fluorescence light". Veröffentlicht auf dem Publikationsserver der RWTH Aachen University. Dissertation. Aachen: RWTH Aachen University, 2016, 1 Online-Ressource (viii, 215 Seiten) : Illustrationen, Diagramme. URL: <http://publications.rwth-aachen.de/record/673852> (cit. on pp. 7, 18, 21, 25, 26, 37, 41, 85).
- [16] J. MATTHEWS. "A Heitler model of extensive air showers". In: *Astroparticle Physics* 22.5 (2005), pp. 387–397. ISSN: 0927-6505. DOI: <https://doi.org/10.1016/j.astropartphys.2004.09.003>. URL: <http://www.sciencedirect.com/science/article/pii/S0927650504001598> (cit. on p. 7).
- [17] P. A. ČERENKOV. "Visible Radiation Produced by Electrons Moving in a Medium with Velocities Exceeding that of Light". In: *Phys. Rev.* 52 (4 Aug. 1937), pp. 378–379. DOI: 10.1103/PhysRev.52.378. URL: <https://link.aps.org/doi/10.1103/PhysRev.52.378> (cit. on p. 8).
- [18] I. M. FRANK and I. E. TAMM. "Coherent visible radiation of fast electrons passing through matter". In: *Compt. Rend. Acad. Sci. URSS* 14.3 (1937). [Usp. Fiz. Nauk 93, no. 2, 388 (1967)], pp. 109–114. DOI: 10.1007/978-3-642-74626-0_2, 10.3367/UFNr.0093.196710o.0388 (cit. on p. 9).
- [19] M. DÖRING et al. "Measurement of the Cherenkov light spectrum and of the polarization with the HEGRA IACT system". In: (2001). arXiv: astro-ph/0107149 [astro-ph] (cit. on p. 10).

- [20] F. G. SCHRÖDER. "Radio detection of cosmic-ray air showers and high-energy neutrinos". In: *Progress in Particle and Nuclear Physics* 93 (2017), pp. 1–68. ISSN: 0146-6410. DOI: <https://doi.org/10.1016/j.ppnp.2016.12.002>. URL: <http://www.sciencedirect.com/science/article/pii/S0146641016300758> (cit. on pp. 11, 12).
- [21] J. RICO. "Overview of MAGIC results". In: *Nuclear and Particle Physics Proceedings* 273–275 (2016). 37th International Conference on High Energy Physics (ICHEP), pp. 328–333. ISSN: 2405-6014. DOI: <https://doi.org/10.1016/j.nuclphysbps.2015.09.046>. URL: <http://www.sciencedirect.com/science/article/pii/S2405601415005350> (cit. on p. 12).
- [22] R. C. G. CHAVES. "Highlights from H.E.S.S." In: *AIP Conference Proceedings* 1792.1 (2017), p. 020012. DOI: 10.1063/1.4968897. eprint: <https://aip.scitation.org/doi/pdf/10.1063/1.4968897>. URL: <https://aip.scitation.org/doi/abs/10.1063/1.4968897> (cit. on p. 12).
- [23] J. HOLDER. "Latest Results from VERITAS: Gamma 2016". In: *AIP Conf. Proc.* 1792.1 (2017), p. 020013. DOI: 10.1063/1.4968898. arXiv: 1609.02881 [astro-ph.HE] (cit. on p. 12).
- [24] *Cherenkov Telescope Array. CTA — the World's Largest Ground-Based Gamma-Ray Observatory*. European Southern Observatory ESO. 2019. URL: <https://www.eso.org/public/teles-instr/paranal-observatory/cta/> (visited on 04/15/2019) (cit. on pp. 12, 13).
- [25] *CTA Telescopes in Southern Hemisphere*. European Southern Observatory ESO. 2019. URL: <https://www.eso.org/public/images/eso1841a/> (visited on 04/14/2019) (cit. on p. 13).
- [26] H. ANDERHUB et al. "Design and operation of FACT – the first G-APD Cherenkov telescope". In: *Journal of Instrumentation* 8.06 (June 2013), P06008–P06008. DOI: 10.1088/1748-0221/8/06/p06008. URL: <https://doi.org/10.1088%2F1748-0221%2F8%2F06%2Fp06008> (cit. on p. 13).
- [27] J. AUFFENBERG et al. "On improving composition measurements by combining compact Cherenkov telescopes with ground based detectors". In: *PoS ICRC2017* (2018), p. 404. DOI: 10.22323/1.301.0404 (cit. on p. 14).
- [28] T. BRETZ et al. "FAMOUS - A fluorescence telescope using SiPMs". In: Aug. 2016, p. 649. DOI: 10.22323/1.236.0649 (cit. on p. 14).
- [29] M. SCHAFEL. "HAWC's Eye. Implementing Hybrid Detection by combining a compact Air-Cherenkov Telescope with the HAWC Gamma-Ray Observatory". Master Thesis. RWTH Aachen University, 2017 (cit. on p. 14).
- [30] E. GANSTER. "Observation of air showers with the IceAct 7 pixel demonstrator in coincidence with IceCube and IceTop". Master Thesis. RWTH Aachen University, Sept. 2018 (cit. on p. 15).

- [31] J. AUFFENBERG. *private communication*. Mar. 20, 2019 (cit. on p. 16).
- [32] THE GEANT4 COLLABORATION. *GEANT4 Logo*. 2019. URL: <https://geant4.web.cern.ch/logo> (visited on 02/22/2019) (cit. on p. 17).
- [33] S. AGOSTINELLI et al. “GEANT4: A Simulation toolkit”. In: *Nucl. Instrum. Meth.* A506 (2003), pp. 250–303. DOI: 10.1016/S0168-9002(03)01368-8 (cit. on pp. 17, 18).
- [34] T. BRETZ et al. “A compact and light-weight refractive telescope for the observation of extensive air showers”. In: *JINST* 13.07 (2018), P07024. DOI: 10.1088/1748-0221/13/07/P07024. arXiv: 1804.01781 [astro-ph.IM] (cit. on p. 18).
- [35] T. NIGGEMANN. *Geant4 detector simulation of the SiPM fluorescence telescope FAMOUS*. <https://github.com/ntim/famous/>. 2016 (cit. on p. 18).
- [36] SCHOTT BOROFLOAT® 33. *The versatile floated borosilicate glass - with an infinite number of applications*. SCHOTT Technical Glass Solutions GmbH. URL: https://psec.uchicago.edu/glass/borofloat_33_e.pdf (visited on 02/27/2019) (cit. on pp. 19, 20).
- [37] R. HUI and M. O’SULLIVAN. “Chapter 1 - Fundamentals of Optical Devices”. In: *Fiber Optic Measurement Techniques*. Ed. by RONGQING HUI and MAURICE O’SULLIVAN. Boston: Academic Press, 2009, pp. 1–128. ISBN: 978-0-12-373865-3. DOI: <https://doi.org/10.1016/B978-0-12-373865-3.00001-X>. URL: <http://www.sciencedirect.com/science/article/pii/B978012373865300001X> (cit. on p. 20).
- [38] W. SELLMEIER. “Zur Erklärung der abnormen Farbenfolge im Spectrum einiger Substanzen”. In: *Annalen der Physik* 219.6 (1871), pp. 272–282. DOI: 10.1002/andp.18712190612. eprint: <https://onlinelibrary.wiley.com/doi/pdf/10.1002/andp.18712190612>. URL: <https://onlinelibrary.wiley.com/doi/abs/10.1002/andp.18712190612> (cit. on p. 21).
- [39] M. N. POLYANSKIY. *Refractive index database*. URL: <https://refractiveindex.info> (visited on 03/10/2019) (cit. on p. 21).
- [40] J. P. KOSCHINSKY. “Development of a 61-Pixel Camera for the IceAct Imaging Air Cherenkov Telescope”. Master thesis. RWTH Aachen University, Sept. 2017 (cit. on pp. 22, 28–30, 32, 46).
- [41] *Positive Fresnel Lenses*. ORAFOL Fresnel Optics GmbH. URL: <https://www.orafol.com/12643> (visited on 02/27/2019) (cit. on pp. 24, 41).
- [42] H. M. EICHLER. “Characterisation studies on the optics of the prototype fluorescence telescope FAMOUS”. Master Thesis. RWTH Aachen University, Mar. 2014 (cit. on pp. 24–26).
- [43] A. DAVIS and F. KÜHNLENZ. “Optical Design using Fresnel Lenses. Basic principles and some practical examples”. In: *Optik & Photonik* 4 (Dec. 2007), pp. 52–55. URL: https://application.wiley-vch.de/berlin/journals/op/07-04/0P0704_S52_S55.pdf (visited on 03/13/2019) (cit. on pp. 25, 26).

- [44] B. BURGMANN. "Klebetests von PMMA basierten Winston-Cones mit Silizium-Photomultipliern für das IceAct Luft-Tscherenkov-Teleskop am Südpol". Bachelor thesis. RWTH Aachen University, Jan. 2019 (cit. on p. 27).
- [45] ROLAND WINSTON, JUAN C. MIÑANO, and PABLO BENÍTEZ, eds. Burlington: Academic Press, 2005. ISBN: 978-0-12-759751-5. DOI: <https://doi.org/10.1016/B978-012759751-5/50017-8>. URL: <http://www.sciencedirect.com/science/article/pii/B9780127597515500178> (cit. on pp. 28, 29).
- [46] C. M. POOLE et al. "A CAD Interface for GEANT4". In: *Australasian Physical & Engineering Science in Medicine* (2012). DOI: 10.1007/s13246-012-0159-8. URL: <http://www.springerlink.com/content/u563877422284578> (cit. on p. 31).
- [47] S. H. SIMON. *The Oxford Solid State Basics*. Oxford University Press, UK, 2013. ISBN: 0199680779 (cit. on p. 32).
- [48] D. RENKER and E. LORENZ. "Advances in solid state photon detectors". In: *Journal of Instrumentation* 4.04 (Apr. 2009), P04004–P04004. DOI: 10.1088/1748-0221/4/04/p04004. URL: <https://doi.org/10.1088/2F1748-0221%2F4%2F04%2Fp04004> (cit. on p. 33).
- [49] *J-Series SiPM. Silicon Photomultipliers (SiPM), High PDE and Timing Resolution Sensors in a TSV Package*. Rev. 6. ON Semiconductor. Dec. 2018. URL: <https://www.onsemi.com/PowerSolutions/product.do?id=J-SERIES%20SiPM> (visited on 03/31/2019) (cit. on pp. 34–37).
- [50] *Opto-semiconductor Handbook*. Hamamatsu Photonics K.K. 2014. URL: https://www.hamamatsu-news.de/hamamatsu_optosemiconductor_handbook/files/assets/basic-html/index.html (visited on 04/02/2019) (cit. on p. 34).
- [51] A. BILAND et al. "Calibration and performance of the photon sensor response of FACT — the first G-APD Cherenkov telescope". In: *Journal of Instrumentation* 9.10 (Oct. 2014), P10012–P10012. DOI: 10.1088/1748-0221/9/10/p10012. URL: <https://doi.org/10.1088/2F1748-0221%2F9%2F10%2Fp10012> (cit. on p. 35).
- [52] T. NIGGEMANN et al. "G4SiPM: A novel silicon photomultiplier simulation package for Geant4". In: *Nuclear Instruments and Methods in Physics Research Section A: Accelerators, Spectrometers, Detectors and Associated Equipment* 787 (2015). New Developments in Photodetection NDIP14, pp. 344–347. ISSN: 0168-9002. DOI: <https://doi.org/10.1016/j.nima.2015.01.067>. URL: <http://www.sciencedirect.com/science/article/pii/S0168900215000996> (cit. on pp. 36, 37).
- [53] *File:Kernel density.svg*. Wikimedia Commons. 2018. URL: https://commons.wikimedia.org/w/index.php?title=File:Kernel_density.svg&oldid=287783112 (visited on 03/31/2019) (cit. on p. 56).

- [54] S. SCHOENEN. "Discovery and characterization of a diffuse astrophysical muon neutrino flux with the iceCube neutrino observatory". Veröffentlicht auf dem Publikationsserver der RWTH Aachen University. Dissertation. Aachen: RWTH Aachen University, 2017, 1 Online–Ressource (xix, 234 Seiten) : Illustrationen, Diagramme. DOI: 10 . 18154 / RWTH - 2017 - 06715. URL: <https://publications.rwth-aachen.de/record/696221> (cit. on pp. 57–59).
- [55] B. WANG and X. WANG. "Bandwidth Selection for Weighted Kernel Density Estimation". In: *arXiv e-prints*, arXiv:0709.1616 (Sept. 2007), arXiv:0709.1616. arXiv: 0709 . 1616 [stat.ME] (cit. on pp. 57, 58).
- [56] B. EFRON. "Bootstrap Methods: Another Look at the Jackknife". In: *Ann. Statist.* 7.1 (Jan. 1979), pp. 1–26. DOI: 10 . 1214 / aos / 1176344552. URL: <https://doi.org/10.1214/aos/1176344552> (cit. on p. 59).
- [57] K. M. GÓRSKI et al. "HEALPix: A Framework for High-Resolution Discretization and Fast Analysis of Data Distributed on the Sphere". In: *The Astrophysical Journal* 622 (Apr. 2005), pp. 759–771. DOI: 10 . 1086 / 427976. eprint: astro-ph/0409513 (cit. on pp. 61, 62).
- [58] CORSIKA – *an Air Shower Simulation Program*. Karlsruhe Institute of Technology (KIT). Dec. 2018. URL: <https://www.ikp.kit.edu/corsika/> (visited on 04/19/2019) (cit. on p. 83).
- [59] D. HECK and T. PIEROG. *Extensive Air Shower Simulation with CORSIKA: A User's Guide. Version 7.6900 from January 16, 2019*. Karlsruhe Institute of Technology (KIT). 2019. (Visited on 04/20/2019) (cit. on p. 83).

Acknowledgements

Danksagungen

Nach nunmehr einem Jahr gilt es, einigen Personen zu danken.

2016 habe ich meine Bachelorarbeit ebenfalls am III. Physikalischen Institut B bei Prof. Wiebusch angefertigt, weshalb mir viele Gesichter der Aachener IceCube Arbeitsgruppe schon bekannt waren. Die Atmosphäre innerhalb der Gruppe ist sehr harmonisch und der rege Austausch in Meetings und Telefonkonferenzen sowie häufiges Feedback haben maßgeblich zu einem Gelingen dieser Ausarbeitung beigetragen.

Insbesondere möchte ich mich bei Prof. Wiebusch bedanken, der mir die Gelegenheit gegeben hat, meine Masterarbeit in seiner Gruppe anzufertigen und Teil einer internationalen Kollaboration zu sein.

Besonderer Dank gilt auch meinem Betreuer Jan Auffenberg und meinen Bürokollegen Merlin Schaufel und Erik Ganster, die mir durch häufige und inspirierende Gespräche jederzeit mit Rat und Tat zur Seite standen.

Abschließend bedanke ich mich bei meiner Familie und meinen Freunden, die mich während meines gesamten Studiums unterstützt und mir Rückhalt gegeben haben.

Eidesstattliche Versicherung

Statutory Declaration in Lieu of an Oath

Günder, Maurice

332308

Name, Vorname/Last Name, First Name

Matrikelnummer (freiwillige Angabe)

Matriculation No. (optional)

Ich versichere hiermit an Eides Statt, dass ich die vorliegende Arbeit/Bachelorarbeit/
Masterarbeit* mit dem Titel

I hereby declare in lieu of an oath that I have completed the present paper/Bachelor thesis/Master thesis* entitled

Simulation of the Optics of the Imaging Air-Cherenkov Telescopes IceAct with Geant4

selbstständig und ohne unzulässige fremde Hilfe (insbes. akademisches Ghostwriting) erbracht habe. Ich habe keine anderen als die angegebenen Quellen und Hilfsmittel benutzt. Für den Fall, dass die Arbeit zusätzlich auf einem Datenträger eingereicht wird, erkläre ich, dass die schriftliche und die elektronische Form vollständig übereinstimmen. Die Arbeit hat in gleicher oder ähnlicher Form noch keiner Prüfungsbehörde vorgelegen.

independently and without illegitimate assistance from third parties (such as academic ghostwriters). I have used no other than the specified sources and aids. In case that the thesis is additionally submitted in an electronic format, I declare that the written and electronic versions are fully identical. The thesis has not been submitted to any examination body in this, or similar, form.

Aachen, 23. April 2019

Ort, Datum/City, Date

Unterschrift/Signature

*Nichtzutreffendes bitte streichen

*Please delete as appropriate

Belehrung:

Official Notification:

§ 156 StGB: Falsche Versicherung an Eides Statt

Wer vor einer zur Abnahme einer Versicherung an Eides Statt zuständigen Behörde eine solche Versicherung falsch abgibt oder unter Berufung auf eine solche Versicherung falsch aussagt, wird mit Freiheitsstrafe bis zu drei Jahren oder mit Geldstrafe bestraft.

Para. 156 StGB (German Criminal Code): False Statutory Declarations

Whoever before a public authority competent to administer statutory declarations falsely makes such a declaration or falsely testifies while referring to such a declaration shall be liable to imprisonment not exceeding three years or a fine.

§ 161 StGB: Fahrlässiger Falscheid; fahrlässige falsche Versicherung an Eides Statt

(1) Wenn eine der in den §§ 154 bis 156 bezeichneten Handlungen aus Fahrlässigkeit begangen worden ist, so tritt Freiheitsstrafe bis zu einem Jahr oder Geldstrafe ein.

(2) Straflosigkeit tritt ein, wenn der Täter die falsche Angabe rechtzeitig berichtigt. Die Vorschriften des § 158 Abs. 2 und 3 gelten entsprechend.

Para. 161 StGB (German Criminal Code): False Statutory Declarations Due to Negligence

(1) If a person commits one of the offences listed in sections 154 through 156 negligently the penalty shall be imprisonment not exceeding one year or a fine.

(2) The offender shall be exempt from liability if he or she corrects their false testimony in time. The provisions of section 158 (2) and (3) shall apply accordingly.

Die vorstehende Belehrung habe ich zur Kenntnis genommen:

I have read and understood the above official notification:

Aachen, 23. April 2019

Ort, Datum/City, Date

Unterschrift/Signature